

A Unified Framework Connecting Chemical Enrichment with Resolved Star Formation Histories

CHRISTOPHER T. GARLING,¹ ALEX M. GARCIA,¹ NIUSHA AHVAZI,^{1,*} NITYA KALLIVAYALIL,¹ KRISTEN B. W. MCQUINN,^{2,3}
ROBERT FELDMANN,⁴ AND ROGER E. COHEN³

¹*Department of Astronomy, University of Virginia, 530 McCormick Road, Charlottesville, VA 22904, USA*

²*Space Telescope Science Institute, 3700 San Martin Drive, Baltimore, MD 21218, USA*

³*Department of Physics and Astronomy, Rutgers, the State University of New Jersey, 136 Frelinghuysen Road, Piscataway, NJ 08854, USA*

⁴*Department of Astrophysics, Universität Zürich, Zurich, CH-8057, Switzerland*

ABSTRACT

We present a new framework for modeling the chemical enrichment histories of galaxies by integrating the chemical evolution with resolved star formation histories (SFHs) derived from color-magnitude diagrams. This novel approach links the time evolution of the metallicity of the star-forming ISM to the cumulative stellar mass formed in the galaxy, enabling a physically motivated, self-consistent description of chemical evolution. We apply this methodology to four isolated, gas-rich Local Group dwarf galaxies—WLM, Aquarius, Leo A, and Leo P—using deep HST and JWST imaging. For WLM, Aquarius, and Leo A, we independently validate our metallicity evolution results using ages and metallicities of individual red giant stars with spectroscopic measurements, finding good agreement. We quantify systematic uncertainties by repeating our analysis with multiple stellar evolution and bolometric correction libraries. We then compare the observed chemical enrichment histories to predictions from the TNG50 and FIREbox cosmological hydrodynamic simulations and the Galacticus semi-analytic model. We find that the enrichment history of WLM is best reproduced by the FIREbox simulation, while TNG50 and Galacticus predict higher metallicities at early times. Our results suggest that differences in stellar feedback and metal recycling prescriptions drive significant variation in the predicted chemical enrichment of dwarf galaxies, particularly at early times. This work demonstrates the power of combining resolved SFHs with physically motivated chemical evolution models to constrain galaxy formation physics and highlights the need for further observational and theoretical studies of metal retention and recycling in low-mass dwarf galaxies.

Keywords: Galaxy chemical evolution (580); Hertzsprung Russell diagram (725); Hubble Space Telescope (761); James Webb Space Telescope (2291); Stellar photometry (1620); Stellar populations (1622)

1. INTRODUCTION

Resolved star formation histories (SFHs) derived from deep color-magnitude diagrams (CMDs) provide the most precise measurements of the star formation rates (SFRs) for galaxies as a function of time. This precision comes from the ability to distinguish stars in different evolutionary phases, allowing for detailed reconstructions of the SFHs of galaxies. Other methods for measuring the SFHs of galaxies, like full spectrum fitting and spectral energy distribution modeling (e.g., J. Walcher et al. 2011; C. Conroy 2013; B. D. Johnson et al. 2021; M. Cappellari 2023), rely on integrated light

from the entire stellar population of the galaxy. Such integrated light measurements suffer from the “outshining” effect, where young stars contribute much of the luminosity of the galaxy, masking the contribution from older stars and limiting the ability of these methods to accurately recover the early-time star formation rates of galaxies (D. Narayanan et al. 2024; T. Harvey et al. 2025; B. Wang et al. 2025).

To accurately model a galaxy’s CMD and disentangle age and metallicity degeneracies, resolved SFH analyses must assume or fit a model for the metallicity evolution of the galaxy as the metallicity at each epoch influences the luminosities and colors of stars (e.g., A. Aparicio & C. Gallart 2004). In this way, the inferred SFRs are inherently coupled to the chemical enrichment history. Most previous approaches to modeling metallicity evo-

Corresponding author: Christopher T. Garling

* Galaxy Evolution and Cosmology (GECO) Fellow

lution in resolved SFHs treat the age-metallicity relation (AMR) as an independent function of time, often taking simple forms with parameters fit simultaneously with the SFH (non-parametric methods have also been used; see, e.g., [A. E. Dolphin 2016](#)). However, there is no physical coupling between the metallicity evolution and the actual star formation activity in these models. This means that changes to the SFH (i.e., the amount or timing of star formation) do not affect the metallicity evolution, and vice versa. The metallicity at a given time is determined solely by the chosen AMR parameterization, not by the integrated effects of past star formation or the enrichment expected from stellar feedback.

As a result, these simple AMR models do not self-consistently evolve the metallicity in response to star formation. This can lead to non-physical solutions, such as metallicity increasing independently of the galaxy’s actual star formation activity (see, e.g., appendix B of [A. Savino et al. 2023](#)). It also makes it difficult to compare observational results to theoretical models in which the metallicity evolves self-consistently as galaxies form stars. In summary, traditional AMR-based approaches lack a physical link between the SFH and chemical enrichment, and therefore do not capture the feedback-driven, self-consistent evolution of metallicity that is expected in real galaxies.

We introduce a novel framework in which the metallicity evolution is directly coupled to the SFH. In this model, the mean metallicity of stars forming at a particular epoch is a function of the cumulative stellar mass formed prior to that epoch. As such, changes to the SFH directly propagate into changes in the metallicity evolution as is expected from galaxy evolution theory. In §2, we describe how we integrate the chemical evolution with the resolved SFH and implement a minimal two parameter model relating them. The primary systematic in resolved SFH measurements based on well-populated CMDs are the stellar models that are assumed when making the measurement. In §3 we describe our method for quantifying these systematics by repeating our measurements with isochrones interpolated from three different libraries of stellar tracks and two different libraries of bolometric corrections. In order to validate our metallicity evolution results, we derive ages and metallicities for single red giant stars in WLM, Aquarius, and Leo A using the method presented in §4. In §5 we present applications of this new method to deep HST/ACS and JWST/NIRCam photometry of four isolated, gas-rich Local Group galaxies – WLM, Aquarius, Leo A, and Leo P. These galaxies range in stellar mass from $5.7 \times 10^5 M_{\odot}$ (Leo P; [K. B. W. McQuinn et al.](#)

[2024a](#)) to $4.3 \times 10^7 M_{\odot}$ (WLM; [A. W. McConnachie 2012](#)), allowing us to probe the chemical evolution of dwarf galaxies over a wide range in stellar mass. To interpret these results, we calculate chemical enrichment histories from the TNG50 and FIREbox cosmological hydrodynamic simulations and the GALACTICUS semi-analytic model in §6. We conclude in §7 with discussion of, and comparison between, the theoretical predictions and observational measurements.

2. CHEMICAL ENRICHMENT MODEL

Here we describe our novel method for simultaneously modeling the SFH and chemical evolution of galaxies. We make use of the framework for hierarchical SFH modeling developed in [C. T. Garling et al. \(2025\)](#), hereafter [Paper I](#), which applied this framework to AMRs – here we extend it to include mass-metallicity histories (MZHs) as well. We begin by outlining the basis of this framework as developed in [Paper I](#) in §2.1 before introducing our new MZH model in §2.2.

2.1. Hierarchical Star Formation History Modeling

We start from the fact that the CMD of a complex stellar population, consisting of stars belonging to multiple populations with different ages and/or metallicities, can be modeled as the superposition of the CMDs of the constituent populations ([A. Dolphin 1997](#)). This remains true for the Hess diagrams of stellar populations, as the Hess diagram is simply a 2-D discretization of the CMD. [Paper I](#) developed methods for generating Hess diagram models for simple stellar populations (SSPs) from stellar models that can be superposed with each other to model observations of complex stellar populations. The SSP Hess diagram models (which we will refer to as *templates* for brevity) are typically constructed for a regular grid of SSP ages and metallicities to cover the range of relevant stellar populations that may coexist in the observed stellar population. A weighted sum of these templates then gives the composite model Hess diagram that will be compared to the observed Hess diagram. Mathematically, the composite model Hess diagram is constructed as

$$m_i = \sum_{j,k} r_{j,k} c_{i,j,k} \quad (1)$$

where m_i is bin i of the complex model Hess diagram, $c_{i,j,k}$ is bin i of the template with age index j (and corresponding age t_j) and metallicity index k (with corresponding metallicity $[M/H]_k$), and $r_{j,k}$ is the multiplicative coefficient that determines how significantly the template contributes to the complex model. Put another way, the complex Hess diagram model m is a linear

combination of the templates $c_{j,k}$ with amplitudes $r_{j,k}$. For the purpose of this work, we will assume the templates are normalized to uniform birth stellar mass, such that $c_{i,j,k}$ are the expected number of stars predicted to be observed in bin i per unit solar mass of stars formed in the SSP and the weight $r_{j,k}$ gives the total stellar mass attributed to the SSP with age t_j and metallicity $[M/H]_k$.

The simplest way to model the observed Hess diagram is to simultaneously fit the $r_{j,k}$ under the sole constraint that all $r_{j,k} \geq 0$ to avoid attributing negative stellar mass to any population. However, as discussed in section 2.7 of Paper I and references therein, this approach tends to overfit the data as the grids of templates used can contain thousands of SSP models, resulting in an equal – and very large – number of free parameters. Additionally, such unconstrained fits can produce non-physical AMRs that undermine the interpretation of the resulting SFH. For this reason, it is common to fit a set of coefficients R_j that are a function of only the age index j and not the metallicity index k . If the templates are normalized to uniform birth stellar mass, then R_j is the sum of the stellar mass formed in all SSPs with age t_j . In this case, a hierarchical model is used that defines how to convert the R_j into the per-template coefficients $r_{j,k}$ that are needed to compute Equation 1. Paper I developed a model that used parametric AMRs to determine the mean metallicity at time t_j , which we define as $\mu_j \equiv \langle [M/H] \rangle(t_j)$. Given this mean value, the R_j are distributed to templates with SSP ages t_j and different metallicities $[M/H]_k$ by assuming a Gaussian metallicity distribution function (MDF) at fixed time with standard deviation σ , given by Equation 8 in Paper I,

$$\begin{aligned} \mu_j &= \langle [M/H] \rangle(t_j) \\ a_{j,k} &= \exp\left(-\left(\frac{[M/H]_k - \mu_j}{\sigma}\right)^2\right) \\ r_{j,k} &= R_j \frac{a_{j,k}}{\sum_k a_{j,k}}. \end{aligned} \quad (2)$$

This class of hierarchical model is highly flexible in that $\mu_j = \langle [M/H] \rangle(t_j)$ can be any time-dependent function. Paper I used simple parametric AMRs to model the time evolution of the mean metallicity, for example $\langle [M/H] \rangle(t) = \alpha(T_{\max} - t) + \beta$ where T_{\max} is the maximum lookback time for which the AMR is valid. In this model, α and β are free parameters and are optimized at the same time as R_j , allowing the covariance between R_j and the AMR parameters to be fully captured. Such parametric AMR models are attractive as they have few free parameters, mitigating concerns about overfitting

the observed data, while providing sufficient freedom to enable good fits to observed Hess diagrams. Additionally, the simple forms of these AMR models allow the gradient of the likelihood function used to optimize the fitting parameters to be derived analytically with little difficulty. With an analytic gradient, finding the best-fit coefficients R_j and AMR parameters (e.g., α and β above) can be done efficiently and robustly.

However, these kinds of AMR models also have several undesirable characteristics. First, these AMR models are not directly linked to the SFH parameters (i.e., the R_j discussed above) – with an AMR model like $\langle [M/H] \rangle(t) = \alpha(T_{\max} - t) + \beta$, changing the SFH parameters R_j does not change $\langle [M/H] \rangle(t)$. Physically, we expect the metallicity of a galaxy to rise due to stellar feedback (e.g., supernovae and AGB winds) over time – therefore, it would be more physical for $\langle [M/H] \rangle(t_j)$ to have some link to the SFH parameters R_j for times earlier than t_j . Additionally, these AMR models are difficult to compare between galaxies – even if observations of two galaxies imply that they have consistent AMRs, they will have different population-averaged metallicities ($\langle [M/H] \rangle$) if their SFHs ($M_*(t)$) are different, as the average age (and, therefore, metallicity) of the two galaxies will be different.

Below we develop a class of MZH models as an alternative to the AMR models used to calculate the μ_j in Equation 2 to address these issues.

2.2. The Mass-Metallicity History Model

As outlined above, the goal of our new MZH model is to connect the chemical evolution of the galaxy $\mu_j = \langle [M/H] \rangle(t_j)$ to the SFH parameters R_j directly, so that the μ_j change in response to changes in the R_j , as is physically expected since the galactic ISM is enriched primarily due to stellar feedback. Our basic approach is to convert the time dependence of $\mu_j = \langle [M/H] \rangle(t_j)$ into a dependence on the total stellar mass formed up to time t_j , which we write as $M_*(t_j)$, such that $\mu_j = \langle [M/H] \rangle(M_*(t_j))$ in the MZH model. This connection between the stellar mass and the metallicity of galaxies has some similarities to the mass-metallicity relation (MZR; e.g., B. H. Andrews & P. Martini 2013; M. Curti et al. 2020), but is fundamentally different. MZR describes the relation between stellar mass and gas-phase metallicity for a population of galaxies with different stellar masses at *one particular epoch*. In contrast, our method describes how the *historical* accumulation of stellar mass relates to an individual galaxy’s chemical enrichment over time; for this reason we discuss our model as a mass-metallicity *history* to differentiate it from the well-known MZR.

Given a set of proposed SFH parameters R_j , it is straightforward to derive the cumulative stellar mass formed in the galaxy as a function of time. Let the R_j be sorted in order from earliest time t_j to most recent time. The cumulative stellar mass $M_*(t_j)$ can therefore be expressed as the sum over the $R_{j'}$ for which $j' \leq j$, such that

$$M_*(t_j) = \sum_{j'=0}^{j'=j} R_{j'} \quad (3)$$

assuming that we have normalized the templates to a uniform birth stellar mass of $1 M_\odot$ as discussed in §2.1 so that the SFH parameters R_j give the total stellar mass formed at each unique epoch t_j . With the ability to calculate $M_*(t_j)$, we can now convert the time dependence of $\mu_j = \langle [M/H] \rangle(t_j)$ into a dependence on the total stellar mass, $\mu_j = \langle [M/H] \rangle(M_*(t_j))$. This alternative form for the μ_j that enter into Equation 2 is the basis for our new class of MZH chemical evolution models.

Given this form, there are many approaches one could take to modeling $\langle [M/H] \rangle(M_*)$. We consider a simple power-law MZH,

$$\begin{aligned} \langle [M/H] \rangle(M_*) &= [M/H]_0 + \log \left(\left(\frac{M_*}{M_{*,0}} \right)^\alpha \right) \\ &= [M/H]_0 + \alpha (\log(M_*) - \log(M_{*,0})) \end{aligned} \quad (4)$$

as is typically used to model the low-redshift MZR in the dwarf regime ($M_* \leq 10^8 M_\odot$; e.g., H. Lee et al. 2006; E. N. Kirby et al. 2013). This model has only two free parameters, the MZH normalization $[M/H]_0$ and the power-law slope α . The parameter $M_{*,0}$ can be chosen arbitrarily and simply defines the stellar mass at which the mean metallicity equals $[M/H]_0$. In this work we will set $M_{*,0} = 10^6 M_\odot$, matching the convention taken by E. N. Kirby et al. (2013) who measured the relation between stellar mass and stellar metallicity for Local Group dwarf galaxies at present-day (see their Equation 4 and Figure 9).

The form of this model is very similar to that of the AMR model from Paper I mentioned previously, $\langle [M/H] \rangle(t) = \alpha (T_{\max} - t) + \beta$; we have simply swapped the time dependence in the AMR for a stellar mass dependence in the MZH. Comparing the performance of the two models on observational data should be relatively straightforward, as both models have the same number of free parameters, and the free parameters consist only of a slope and a normalization for each model.

We implement this model in `StarFormationHistories.jl`⁵ alongside the AMR models developed in Paper I. Our implementation is general in the sense that it is easy to define new forms for $\langle [M/H] \rangle(M_*)$ that will plug into the existing infrastructure of `StarFormationHistories.jl` to measure resolved SFHs from photometry. This generality is important because this simple power-law model will be insufficient for some types of galaxies. In particular, it is well-established observationally that the MZR saturates at $\sim 10^{10.5} M_\odot$ (e.g., B. H. Andrews & P. Martini 2013; M. Curti et al. 2020) – modeling a similar turnoff in the MZH would require a more complicated model (e.g., Equation 2 of M. Curti et al. 2020), but is irrelevant for the lower mass galaxies we study here. Additionally, it is possible that the power-law MZH may not be appropriate at very low masses either – spectroscopic studies of ultra-faint dwarf galaxies with stellar masses below $10^5 M_\odot$ generally measure mean galaxy metallicities $\langle [M/H] \rangle \geq -3$ dex, indicating that there may be something like a metallicity floor in UFDs. In such a case, extrapolating a power-law MZH to $\langle [M/H] \rangle = -4$ dex would be inappropriate, and again a more complicated model would be required. In this work we stay between these regimes, where the power-law model is well-supported observationally – we may define alternative models in future work as necessary.

2.3. Interpreting the Mass-Metallicity History

We note that while the form of the MZH $\langle [M/H] \rangle(M_*)$ we propose in Equation 4 is motivated by observational results for low-redshift dwarf galaxies (e.g., H. Lee et al. 2006; E. N. Kirby et al. 2013), the observational measurements of the MZR differ in an important way from our definition of the MZH. The observational results take a population of different galaxies observed at one epoch, each of which have unique stellar masses and metallicities, and measure the correlation between their metallicities and stellar masses. Such observed MZR are thus valid at one particular redshift and cannot be used to infer the metallicities of the observed galaxies at earlier times. In our application, we are modeling $\langle [M/H] \rangle(M_*(t))$ – that is, we are assuming a time-independent form for the MZH and assuming that the galaxy evolves along the MZH as it accumulates stellar mass over time. Such a mass-metallicity *history* is therefore not identical to the MZR that have been measured observationally. Given that our MZH model is defined differently from the MZR, it may therefore deviate from

⁵ <https://github.com/cgarling/StarFormationHistories.jl>

the simple power-law form we have assumed based on the observational results for the MZR. In §6, we measure the MZH in several theoretical datasets to examine how well our power-law MZH model matches expectations from theory, taking into account the historical definition of our MZH model. We show that different galaxy formation models produce different predictions for the MZH, but the power-law MZH is sufficient to model their morphologies at dwarf galaxy masses.

We expect the MZH model to capture several important aspects of the relation between ISM enrichment and galactic stellar mass growth. The metallicity of the ISM is determined by the competing mechanisms of enrichment (due to stellar feedback) and dilution (due to accretion of low-metallicity gas). In equilibrium models of galaxy evolution, a relation between galactic stellar mass and metallicity arises naturally as a consequence of these processes (e.g., R. Davé et al. 2012; S. J. Lilly et al. 2013). However, the process of enrichment is complicated by the fact that not all metals ejected in a supernova are expected to stay in the ISM – particularly in the shallow potential wells of dwarf galaxies, supernovae can drive winds with significant metal content into the circumgalactic medium (CGM) or out of the halo entirely (e.g., R. Davé et al. 2012; S. J. Lilly et al. 2013; R. Feldmann 2015; A. L. Muratov et al. 2015, 2017; C. R. Christensen et al. 2016, 2018; D. Anglés-Alcázar et al. 2017; A. Emerick et al. 2018; T. Buck et al. 2019; D. Nelson et al. 2019; É. Tollet et al. 2019; O. Agertz et al. 2020; P. D. Mitchell et al. 2020; V. Pandya et al. 2021; L. Bassini et al. 2024). These metals will not be available in the ISM to form the next generation of stars, and so these metals do not effectively contribute to the enrichment of the ISM.

In the context of galactic chemical evolution models, this effect is quantified by the *effective yield* which is, by definition, less than or equal to the total nucleosynthetic yield of stellar enrichment processes – the difference between the canonical “closed box” and “leaky box” chemical evolution models is the substitution of the total nucleosynthetic yield in the former for the effective yield in the latter (see, e.g., section 5.1 of E. N. Kirby et al. 2013, and references therein). In high-resolution simulations, it is well established that the outflow mass-loading factor of these winds, defined as the ratio of the mass flux of the outflow to the galactic SFR ($\eta = \dot{M}_{\text{out}}/\text{SFR}$), correlates with halo properties (e.g., halo circular velocity) and galaxy properties (e.g., stellar mass), though these correlations differ depending on the galaxy formation model assumed (e.g., A. L. Muratov et al. 2015, 2017; C. R. Christensen et al. 2016, 2018; D. Nelson et al. 2019; P. D. Mitchell et al. 2020; V. Pandya et al. 2021;

M. P. Rey et al. 2025). Generally, the fraction of created metals that is retained in the ISM is expected to be low at dwarf galaxy scales, as a significant portion of the metals created in supernovae are blown out of the ISM by their associated winds. For example, analyses using the FIRE-1 and FIRE-2 galaxy evolution models predict that nearly all metals produced in core-collapse supernovae should be ejected from the ISM in galaxies with $M_* \leq 10^9 M_\odot$ (A. L. Muratov et al. 2017; V. Pandya et al. 2021). These metals persist in the circumgalactic medium of these galaxies and can be accreted into the ISM given enough time, resulting in the metallicity of accreted gas evolving as a function of time in the FIRE-2 model (L. Bassini et al. 2024). Other galaxy evolution models typically predict weaker metal outflows, but there is significant variation between models (see, e.g., C. R. Christensen et al. 2018; D. Nelson et al. 2019; P. D. Mitchell et al. 2020; R. J. Wright et al. 2024; A. M. Garcia et al. 2024a, 2025a). These galaxy evolution models also differ in the redshift dependence they predict for these outflow parameters at fixed galaxy stellar mass.

In summary, star-formation-driven outflows in dwarf galaxies are expected to entrain a significant quantity of metals so that the effective metal yield (the quantity of metals ejected in stellar feedback that is retained in the ISM) is substantially less than the total nucleosynthetic metal yield. However, variations in the effective metal yields between galaxy evolution models are significant – for example, P. Torrey et al. (2019) find that $\sim 50\%$ of the metal mass created in galaxies with $M_* \approx 10^9 M_\odot$ at present-day are retained in the ISM under the IllustrisTNG galaxy evolution model, while V. Pandya et al. (2021) find that nearly all metals created in galaxies of this mass are ejected from the ISM in the FIRE-2 galaxy evolution model. It is therefore of significant interest to design observational tests that can differentiate between these scenarios.

It is useful to consider what relation our power-law model for $\langle [M/H] \rangle (M_*)$ has to other chemical evolution models. Most obviously, our model tracks only the *relative abundance of metals and hydrogen* and does not consider the galaxy’s gas mass whatsoever, while traditional one-zone analytic galactic chemical evolution models (closed box, leaky box, etc.) track the total galactic gas and metal masses separately in order to calculate the metal mass fraction Z (see, e.g., M. Peimbert et al. 1994, for an overview of these models). These models require boundary conditions for the galactic gas and metal mass fractions in the earliest and latest time bins that are often not available observationally, requiring the researcher to either adopt reasonable values or fit these boundary conditions as part of the model. These

chemical evolution models can include free parameters to model metal-poor gas inflows, metal-rich outflows driven by stellar feedback, and other processes (e.g., M. Peimbert et al. 1994; E. N. Kirby et al. 2013; K. A. Kvasova & E. N. Kirby 2025), but priors on these parameters tend to be weak, increasing the number of free parameters in the MZH model and the risk of overfitting the photometric data. These models have been shown to successfully reproduce the time-integrated MDFs of observed dwarf galaxies (e.g., E. N. Kirby et al. 2011a, 2013, 2019; K. A. Kvasova & E. N. Kirby 2025) but are rarely used to predict the time-dependence of the metallicity and thus are mostly untested in the time domain (for a recent example, see Figure 3 of K. A. Kvasova & E. N. Kirby 2025). A promising solution is to use external spectroscopic measurements to constrain the parameters of a one-zone chemical evolution model jointly with the photometry. As significant technical challenges must be overcome to perform such joint photometric-spectroscopic measurements (A. E. Dolphin 2016), we leave this development for future work.

Due to the modularity of our modeling framework, it is straightforward to implement new functional forms for $\langle[M/H]\rangle(M_*)$. The model can even be extended to include a time dependence in the MZH, by generalizing $\mu_j = \langle[M/H]\rangle(M_*(t_j))$ to have additional time dependence beyond that implied by $M_*(t_j)$ – for example, by making the power-law slope α have a dependence on redshift. However, without priors on what form this dependence should take we would risk overfitting the data with a more complex MZH model. While higher redshift observations for higher mass dwarfs (generally $M_* \geq 10^8 M_\odot$) are becoming available thanks to JWST (e.g., M. Li et al. 2023; K. Nakajima et al. 2023; M. Curti et al. 2024; S. Jain et al. 2025), we leave investigation of time dependence in the MZH parameters to future work.

3. SYSTEMATIC UNCERTAINTIES DUE TO STELLAR MODELS

It is well-established that the stellar models used to forward model observed CMDs contribute significantly to the overall systematic uncertainty of the measurement and can even dominate the overall error budget for nearby galaxies with well-populated CMDs and deep photometry (e.g., C. Gallart et al. 2005; A. E. Dolphin 2012; D. R. Weisz et al. 2014; E. D. Skillman et al. 2017). It is therefore important to consider how the choice of stellar interior models, and the bolometric corrections (BCs) that transform them into observational magnitudes, affects the measured SFHs and chemical evolution parameters.

The methodology used by MATCH to quantify systematic uncertainties due to the assumed stellar models is described by A. E. Dolphin (2012). In brief, the method shifts the fiducial isochrone models in temperature and bolometric magnitude and refits the SFH with these altered isochrones. The sizes of the shifts are randomly sampled in a Monte Carlo procedure and are drawn from distributions designed to reproduce the age and metallicity differences observed under different stellar model libraries. Credible intervals can then be measured from these Monte Carlo samples, enabling the estimation of the systematic errors.

While this approach is flexible, simple shifts in temperature and bolometric magnitude cannot reproduce morphological differences between stellar models, such as the shape of the MSTO, nor does it provide a mechanism to separate the systematic uncertainty contribution of the stellar tracks (i.e., the stellar interior models) from the contribution due to the assumed BCs (i.e., the stellar atmosphere models).

For this reason we choose to estimate systematic uncertainties in our SFH measurements and chemical evolution parameters by refitting the data directly with different combinations of stellar interior models and BC libraries. This approach *can* be less robust than the method of A. E. Dolphin (2012), as often very few different stellar models are considered – often only two stellar model libraries are compared, and typically only one BC library is used for each stellar interior library. In order for this approach to be robust, several stellar libraries should be used, and ideally several sets of BCs should be considered as well.

Our software `StarFormationHistories.jl` is structured to work with generic isochrones, including those that can be downloaded from webforms maintained by different groups; such user-downloaded isochrones were used in Paper I. This approach is convenient when only a single stellar library is needed, but becomes cumbersome when one wishes to use several stellar interior and BC libraries. Additionally, most webforms only support a single library of BCs, and mixing different stellar tracks with different tables of BCs is generally not supported.

To support the calculation of systematic uncertainties due to stellar models, we have developed and publicly released new packages to interpolate isochrones on-the-fly. The `StellarTracks.jl`⁶ package provides access to stellar track libraries from several groups and can interpolate isochrones at arbitrary metallicities and ages.

⁶ <https://github.com/cgarling/StellarTracks.jl>

This integrates with the `BolometricCorrections.jl`⁷ package that provides access to pre-computed tables of BCs derived from several different libraries of synthetic spectra to transform the stellar bolometric magnitudes into the observed magnitudes. The packages are structured so that any stellar track library can be used with any BC library, allowing arbitrary combinations. This modularity allows us to separately examine the systematics due to the stellar interiors and those due to the BCs.

3.1. Stellar Tracks

All stellar tracks accessible through `StellarTracks.jl` include equivalent evolutionary points (EEPs) to support accurate isochrone interpolation using the method of A. Dotter (2016). The package currently provides access to the PARSEC, MIST, and BaSTI stellar model grids. All have been widely used for resolved SFH studies as they have wide coverage of stellar metallicity and initial stellar masses, and such wide coverage is critical to simultaneously model populations of many ages and metallicities, as is necessary when fitting resolved SFHs. The PARSEC, MIST, and BaSTI stellar model grids are described briefly below.

We utilize the PARSEC V1.2S stellar tracks (A. Bressan et al. 2012; Y. Chen et al. 2014; J. Tang et al. 2014; Y. Chen et al. 2015; P. Marigo et al. 2017) reprocessed with EEPs by P. Rosenfield et al. (2016)⁸. The tracks with EEPs were originally produced for use in the MATCH code and are still in use today. This library covers a wide range of stellar parameters with scaled-solar metallicities ($[M/H]$) ranging from -2.2 to 0.5 dex and initial stellar masses ranging from 0.1 to $350 M_{\odot}$, although the grid of available metallicities and stellar masses is not entirely regular. The models include evolution through the thermally-pulsating AGB phase by integrating with results from the COLIBRI code (P. Marigo et al. 2017). Horizontal branch evolution is also included.

The MIST stellar tracks (A. Dotter 2016; J. Choi et al. 2016) cover stars with scaled-solar metallicities ($[M/H]$) ranging from -4 to 0.5 dex and initial stellar masses ranging from 0.1 to $300 M_{\odot}$. These models were run with the MESA code (B. Paxton et al. 2013, 2015) and feature continuous evolution through many phases of stellar evolution, which is unique for these types of stellar track libraries. PARSEC, for comparison, computes the core hydrogen burning, core helium burning, and

thermally-pulsating AGB phases separately (see section 5.3 of A. Bressan et al. 2012). MIST isochrones are also included in MATCH. MIST includes both rotating and non-rotating models, and both are available in our package.

The previous generation of BaSTI stellar tracks (which we refer to as BaSTIv1 for short) presented in A. Pietrinferni et al. (2004, 2006, 2013) includes stars with metallicities ($[M/H]$) ranging from -3 to 0.5 dex and initial stellar masses ranging from 0.5 to $10 M_{\odot}$. While the limited range of initial stellar masses means this grid cannot be used on *all* data sets, sets of stellar models are available for a number of different modeling assumptions. For example, models are available with and without convective core overshooting (so-called non-canonical and canonical models), for different values of the Reimers mass loss parameter ($\eta = 0.2$ and 0.4), and for different relative α -element abundances ($[\alpha/Fe] = 0.0$ and 0.4 dex). All of these sets of tracks are made available and can be easily switched between in our package, enabling differential analyses as a function of these additional parameters. These models have been largely superseded by newer BaSTI models described below, but can still provide a useful point of comparison.

The current generation of BaSTI models (which we refer to as BaSTIv2 for short) presented in S. L. Hidalgo et al. (2018); A. Pietrinferni et al. (2021); M. Salaris et al. (2022); A. Pietrinferni et al. (2024) cover stars with metallicities ($[M/H]$) ranging from -3.2 to 0.45 dex and initial stellar masses ranging from 0.1 to $15 M_{\odot}$. This range of stellar initial masses is typically sufficient for modeling the CMDs of galaxies with little recent star formation (e.g., A. Savino et al. 2023, 2025; M. J. Durbin et al. 2025). Like BaSTIv1, this library also includes tracks for a wide range of modeling parameters – tracks were calculated with and without convective core overshooting, atomic diffusion, and mass loss (Reimers mass loss parameters $\eta = 0.0$ and 0.3). Additionally, tracks are available with different relative α -element abundances ($[\alpha/Fe] = -0.2, 0.0$ and 0.4 dex; A. Pietrinferni et al. 2021, 2024). He-enhanced tracks are also available for the α -enhanced models (A. Pietrinferni et al. 2021). All of these tracks are included in our package and can be easily selected by users.

As mentioned previously, `StellarTracks.jl` only considers stellar photospheric quantities (e.g., temperature, radius) and interpolates isochrones in the Hertzsprung-Russell diagram space (temperature and luminosity). To transform the isochrones into the required observational magnitudes, `StellarTracks.jl` integrates with the `BolometricCorrections.jl` package, which supports interpolation of multiple libraries

⁷ <https://github.com/cgarling/BolometricCorrections.jl>

⁸ https://github.com/philrosenfield/padova_tracks

of BCs. A common interface is defined between the two packages to facilitate the use of isochrones from any of the above stellar model sets with any of the defined BC libraries below. This modularity allows us examine systematics due to the stellar interior models separately from those due to the assumed BCs.

3.2. Bolometric Corrections

`BolometricCorrections.jl` currently supports the MIST (J. Choi et al. 2016) and YBC (Y. Chen et al. 2019) libraries of BCs. These libraries are chosen as they are publicly available, cover wide ranges of stellar parameters, and have been calculated for many observational filter sets. However, they have been calculated using different model atmospheres and spectral synthesis codes such that differences in the BCs should reflect the systematic uncertainties in the underlying theoretical models. Brief descriptions are given below.

The MIST BCs were presented by J. Choi et al. (2016). This library is composed of four sub-components that are combined to form the final BC tables that are publicly distributed.⁹ The principal component of the library are C3K synthetic spectra (C. Conroy et al. 2018) which use hydrostatic, plane-parallel atmospheres computed with the ATLAS12 code. Synthetic spectra were computed from the atmosphere models with SYNTH3 (R. L. Kurucz 2005, 2014). The C3K synthetic spectra are supplemented with the D. Koester (2010) spectral library for white dwarfs with H-rich atmospheres (DA type), blackbody spectra for stars hotter than 200,000 K, and new synthetic spectra for cool carbon stars with C/O = 1.05. After combining these sub-components, the final tables have extremely wide coverage of the stellar parameter space, covering scaled-solar metallicities ($[M/H]$) from -4 to 0.5 dex, effective temperature from 2,500 K to 1,000,000 K, and surface gravity¹⁰ from -4 to 9.5 dex. BCs are provided for V-band extinction $0 \leq A_V \leq 6$ mag with $R_V = 3.1$ assuming the J. A. Cardelli et al. (1989) reddening law.

While the large grid coverage is useful from a practical perspective, there are several phases of stellar evolution where these models are not appropriate; for example, hot O- and B-type stars are known to have radiation-driven winds that affect their spectra, and this effect is not captured in these BCs. Additionally, the MIST BCs were calculated with pre-launch filter curves for JWST/NIRCam and have not been updated to reflect the most recent measurements of the system through-

puts. While this is suboptimal, comparisons of the BCs in the F090W and F150W filters between MIST and YBC (which uses the updated filter curves) for hot MS stars shows very good agreement (~ 0.01 mag at $T_e = 5000$ K) as expected since both use variants of ATLAS models for these stars. By comparison, the YBC and MIST BCs differ much more for cool stars (~ 0.09 mag for $T_e = 2700$ K) as a result of the different atmospheres they adopt at low temperatures. As such, we estimate the outdated F090W and F150W filter curves for JWST/NIRCam used in MIST constitute a systematic error of $\sim 2\%$. It is worthwhile to compare SFH measurements using MIST BCs to measurements using YBC as this systematic is minor compared to the differences in the atmospheres between these libraries.

The YBC BCs were presented in Y. Chen et al. (2019). These are typically associated with the PARSEC stellar models as the YBC BCs are the default choice in the web-based interface to the PARSEC stellar models. YBC is also made up of several sub-components like MIST, but does not provide tables that combine them in a predetermined way. Rather, the BCs for each sub-component are made public¹¹ and user routines must then stitch them together in an appropriate way. We make use of four sub-components in our initial implementation. In all cases the transitions between the sub-components are smoothly interpolated over to prevent discontinuities in the joint BC tables. The BCs of all sub-components are provided for V-band extinction $0 \leq A_V \leq 20$ mag with $R_V = 3.1$ assuming the J. A. Cardelli et al. (1989) reddening law with the updated parameters of J. E. O'Donnell (1994). The sub-components are summarized below.

1. PHOENIX BT-Settl models (F. Allard et al. 2012) are used for cool stars with temperatures 2570 – 6000 K. The PHOENIX code assumes a hydrostatic, spherical geometry and is specially designed to model the atmospheres of cool systems, including stars and even sub-stellar objects. These models are available for metallicities between -4 and 0.5 dex and surface gravities between -0.5 and 6 dex. Sub-solar metallicities are α -enhanced relative to the solar chemical composition with $[\alpha/Fe] = 0.2$ dex at $[M/H] = -0.5$ dex and $[\alpha/Fe] = 0.4$ dex for lower metallicities.
2. The ATLAS9 ODFNEW models of F. Castelli & R. L. Kurucz (2003) are used for hot stars with temperatures 6000 – 50,118 K. These are hydrostatic, plane-parallel atmospheres computed with

⁹ https://waps.cfa.harvard.edu/MIST/model_grids.html

¹⁰ When discussing surface gravity, we always mean $\log(g)$ with g in cgs units.

¹¹ https://gitlab.com/cycyustc/ybc_tables

the opacity distribution function method which is less accurate for cool stars with significant molecular features compared to direct opacity sampling as is used in PHOENIX and ATLAS12 (see, e.g., B. Plez 2011). These models are available for scaled-solar metallicities between -2.5 and 0.5 dex and surface gravities between 0 and 5 dex.

3. The white dwarf models of P. E. Tremblay & P. Bergeron (2009); D. Koester (2010) are used when the surface gravity is greater than 6 dex and the temperature is greater than 5700 K. These synthetic spectra assume H-rich atmospheres (DA type).
4. Models for hot O- and B-type stars computed with the `WM-basic` code by Y. Chen et al. (2019) are used for stars with temperatures greater than $21,000$ K and mass outflow rates greater than 10^{-7} solar masses per year. Such stars are luminous enough to drive significant outflows that can greatly affect their observed spectra (e.g., O. G. Telford et al. 2024) and these models explicitly include the effects of the outflows on the resulting synthetic spectra. Generally stellar evolution codes do not provide mass outflow rates as they only evolve stellar interior quantities and so do not simultaneously resolve outflows driven from the atmosphere. If stellar tracks include mass loss rates, they are typically calculated from scaling relations that depend on the interior properties – for example, section 2.3 of J. Tang et al. (2014) and Y. Chen et al. (2015) describe the PARSEC implementation and section 3.7 of J. Choi et al. (2016) describes the MIST implementation. BaSTI only uses the well-known Reimers mass loss prescription for RGB stars (D. Reimers 1975). Recently, some commonly used mass-loss prescriptions (e.g., J. S. Vink et al. 2001) have been shown to over-predict the mass-loss rates of low-metallicity stars (e.g., C. Hawcroft et al. 2024; O. G. Telford et al. 2024), resulting in spectral models that strongly disagree with observations, particularly at short wavelengths. As most resolved SFH work focuses on populations with sub-solar metallicities, we deem it prudent to support alternative mass-loss prescriptions. We therefore include the ability to calculate mass-loss rates on-the-fly from the stellar interior quantities using different scaling relations. Our fiducial choice is the mass-loss prescription of R. Björklund et al. (2021) which shows significantly better agreement with observations of low-metallicity stars (C. Hawcroft et al. 2024; O. G. Telford et al. 2024).

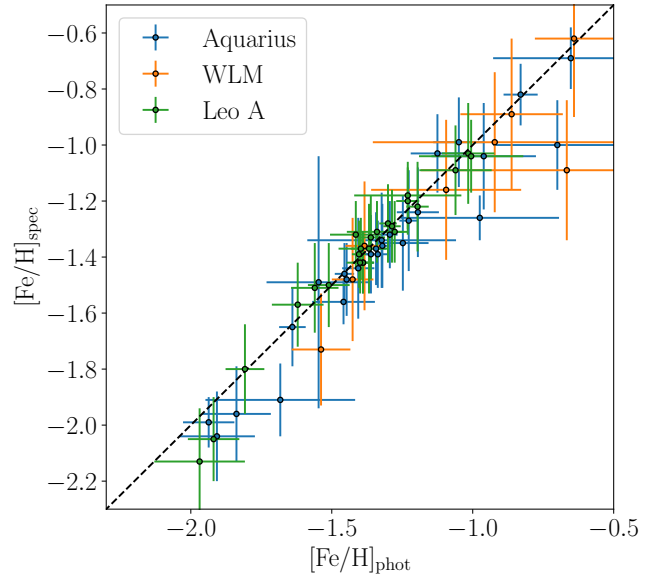


Figure 1. Comparison of $[\text{Fe}/\text{H}]$ measurements of single red giants from Aquarius, WLM, and Leo A. The vertical axis shows the spectroscopic $[\text{Fe}/\text{H}]$ measurements, which are used as a prior when measuring the metallicity and ages from the photometry in §4. The resulting photometrically-measured $[\text{Fe}/\text{H}]$ values are shown on the horizontal axis. The line where $[\text{Fe}/\text{H}]_{\text{spec}} = [\text{Fe}/\text{H}]_{\text{phot}}$ is overplotted for comparison. Agreement between the two is generally excellent, although the photometric technique prefers marginally higher metallicities for stars with $[\text{Fe}/\text{H}]_{\text{spec}} < -1.8$ dex.

3.3. Systematic Uncertainty Estimation Procedure

Given these available libraries of stellar tracks and BCs, we estimate the model-dependent systematic uncertainties in the following straightforward manner: using the PARSEC, MIST, and BaSTIv2 stellar track libraries and the MIST and YBC BC libraries, we repeat the CMD fitting procedure under each of their six possible combinations and quote the systematic uncertainties in quantities like the cumulative SFH and metallicity as function of time as the smallest interval that contains all six solutions. We always use non-rotating MIST models and for BaSTIv2 we use scaled-solar models with convective overshooting, atomic diffusion, and Reimers mass-loss parameter $\eta = 0.3$.

4. AGES FOR INDIVIDUAL STARS

For Leo A (E. N. Kirby et al. 2017), Aquarius (E. N. Kirby et al. 2017; L. Hermosa Muñoz et al. 2020), and WLM (R. Leaman et al. 2009) there are available catalogs of spectroscopic metallicities for red giant stars. With stellar metallicities for individual stars, we can estimate their ages as well based on our high-precision photometry. With ages and metallicities for individual stars in these galaxies, we can perform an independent

check of the metallicity evolutions determined from our resolved SFH fits. If a star is observed in a sufficient number of filters, multi-band photometry can be used to extract stellar masses, ages, and metallicities simultaneously (e.g., [K. D. Gordon et al. 2016](#)), but given that we have only 2–3 broad bands of photometry for the galaxies in our sample, we require metallicity priors in order to obtain robust ages. Additionally, we marginalize over the range of possible stellar masses for each star in order to increase the precision of our age estimates as the stellar masses are not of particular interest here.

For a proposed age t and metallicity Z we interpolate an appropriate isochrone using the methods of [3.1](#) and [3.2](#). For all calculations we assume the distance moduli and interstellar reddening values shown in [Table 1](#), which are also used for the resolved SFH fits in the next section. Letting the list of apparent magnitudes of the star be \mathbf{m} , the associated magnitude uncertainties be σ^{12} , the apparent magnitude (error) in filter i be \mathbf{m}_i (σ_i), and the predicted apparent magnitude from the isochrone for age t , stellar mass M , and metallicity Z in filter i be $I(t, Z, M)_i$, we write the likelihood of the data given the model as

$$L(\mathbf{m}|t, Z, M) = \prod_i \left(\frac{1}{\sqrt{2\pi} \sigma_i} \exp \left[-\frac{(\mathbf{m}_i - I(t, Z, M)_i)^2}{2\sigma_i^2} \right] \right) \quad (5)$$

We then apply Bayes’ theorem, multiplying this likelihood with our priors to form a probability distribution that is proportional to the posterior. As is common, we neglect the Bayesian evidence $P(\mathbf{m})$ that appears in the denominator of Bayes’ theorem as it is unnecessary for the BFGS optimization scheme we employ (see [Section 6.1](#) of [J. Nocedal 2006](#)). We assume the [P. Kroupa \(2001\)](#) initial mass function (IMF) as the prior on the stellar mass and a uniform prior on the stellar age from 1 – 13.7 Gyr. The lower limit is a rough estimate of the youngest stars that could fall within the RGB selection region of these studies, while the upper limit is the approximate age of the Universe. The spectroscopically measured metallicity is used as the prior on the metallicity, modeled as a Gaussian distribution with standard deviation equal to the reported metallicity uncertainty. We additionally increase the weighting of the metallicity prior by multiplying it by the number of filters to better match the scale of the photometric likelihood function,

which is a product over the i filters. We marginalize over the stellar mass M to estimate t and Z for each star.

To account for systematic uncertainties due to the assumed stellar models, we repeat the above procedure for each combination of the PARSEC, MIST, and BaSTIv2 stellar track libraries and the MIST and YBC BC libraries – therefore, six measurements are made in total for each star. Our final t and Z values are taken to be the sample mean of these six measurements and we report errors as the sample standard deviation. We note that these uncertainties are several times larger than the formal random uncertainties obtained, for example, via MCMC sampling of the likelihood function as the photometric uncertainties that enter into [Equation 5](#) are small, typically $\sigma \leq 0.02$ mag. This again highlights the importance of considering the systematic impact of stellar model choice when performing comparisons against high-precision photometry.

The metallicities we find by optimizing [Equation 5](#) are generally consistent with the spectroscopic measurements – this can be seen quantitatively in [Figure 1](#), which compares the spectroscopic [Fe/H] measurements to our photometric measurements that use the spectroscopic values as a prior. These spectrophotometric metallicities and ages are shown superposed with our metallicity evolutions derived from the global resolved SFH in the next section.

5. OBSERVATIONAL RESULTS

Here we present results applying our MZH SFH model to four isolated Local Group dwarf galaxies. As environmental processes can affect the star formation of dwarf galaxies after infall to a more massive host ([J. Woo et al. 2013](#); [Y. Zu & R. Mandelbaum 2016](#); [L. Kawinwanichakij et al. 2017](#); [T. Moutard et al. 2018](#); [C. Papovich et al. 2018](#); [L. J. M. Davies et al. 2019](#); [J. Van Nest et al. 2023](#); [Y. Wang et al. 2024](#); [G. Torres-Ríos et al. 2024](#)), we select only isolated Local Group dwarfs that do not lie within the halo of a more massive galaxy to facilitate comparisons with theory in [§6](#). We apply our methodology to the WLM, Aquarius, Leo A, and Leo P dwarf galaxies in this work, as they all have high-precision archival photometry available as well as literature SFH and metallicity measurements that we can compare our results to. Properties of these galaxies relevant to our application are summarized in [Table 1](#). Summary τ statistics for our SFH fits are given in [Table 2](#), where τ_x is the lookback time at which a galaxy formed $x\%$ of its total stellar mass (e.g., τ_{10} is the lookback time at which the galaxy formed 10% of its total stellar mass).

¹² The uncertainties of the observed magnitudes that enter into [Equation 5](#) (σ) are estimated from artificial star tests in the same way as the uncertainties are estimated when performing the full resolved SFH measurements in [§7](#).

Table 1. Galaxy Properties

Galaxy	R.A. (J2000)	Decl. (J2000)	$E(B - V)$	M_*	M_{HI}	D_\odot	μ
	(hms)	(dms)	(mag)	(M_\odot)	(M_\odot)	(kpc)	(mag)
WLM	00:01:58.53 (1)	-15:27:27.20 (1)	0.032 (2)	4.3×10^7 (3)	6.3×10^7 (4)	968 ± 41 (5)	24.93 ± 0.09 (5)
Leo A	09:59:26.5 (3)	+30:44:47.0 (3)	0.018 (2)	1.3×10^6 (6)	6.91×10^6 (7)	798 ± 44 (8)	24.51 ± 0.12 (8)
Aquarius	20:46:51.8 (3)	-12:50:53.0 (3)	0.043 (2)	2.6×10^6 (3)	4.1×10^6 (9)	977 ± 45 (10)	24.95 ± 0.10 (10)
Leo P	10:21:42.509 (6)	+18:05:16.09 (6)	0.022 (2)	5.7×10^5 (6)	8.1×10^5 (11, 12)	1620 ± 150 (11)	26.05 ± 0.20 (11)

References—(1) R. E. Cohen et al. (2025); (2) D. J. Schlegel et al. (1998) & E. F. Schlafly & D. P. Finkbeiner (2011); (3) A. W. McConnachie (2012); (4) A. A. Kepley et al. (2007); (5) S. M. Albers et al. (2019); (6) K. B. W. McQuinn et al. (2024a); (7) D. A. Hunter et al. (2012); (8) A. E. Dolphin (2002); (9) M. E. Putman et al. (2021); (10) A. A. Cole et al. (2014); (11) K. B. W. McQuinn et al. (2015); (12) R. Giovanelli et al. (2013)

We use the P. Kroupa (2001) IMF for all calculations. A metallicity spread of $\sigma = 0.1$ dex (see Equation 2) is used for all galaxies except WLM, where a value $\sigma = 0.2$ dex gives a better fit to the data. When making our measurements, we assume color excesses $E(B - V)$ based on the dust maps of D. J. Schlegel et al. (1998) with the updated scaling of E. F. Schlafly & D. P. Finkbeiner (2011) and calculate V-band extinctions (A_V) assuming $R_V = 3.1$. Reddening is added to the synthetic CMD models via interpolation of the BC tables (see §3.2) – both the MIST and YBC tables are tabulated on a grid of A_V values, taking into account the integrated effect of the reddening over each filter in a self-consistent fashion. MIST uses the J. A. Cardelli et al. (1989) reddening law and YBC uses the same functional form but with the updated coefficients from J. E. O’Donnell (1994). These differ by a few percent at near-UV wavelengths, but in the optical (where our data lie) the typical difference between the two averages to $< 1\%$.

5.1. WLM

We first apply our new MZH metallicity evolution model to the WLM dwarf irregular galaxy ($M_v \approx -14.2$ mag, $M_* \approx 4.3 \times 10^7 M_\odot$, A. W. McConnachie 2012) which we previously studied with an AMR metallicity evolution model in C. T. Garling et al. (2025). WLM is isolated and gas-rich ($M_{\text{HI}}/M_* > 1$) with a distance modulus of $\mu = 24.93 \pm 0.09$ mag ($d = 968_{-40}^{+41}$ kpc, S. M. Albers et al. 2019) – it is therefore near enough that deep imaging with HST/ACS and JWST/NIRCAM has enabled robust measurement of its resolved SFH (S. M. Albers et al. 2019; K. B. W. McQuinn et al. 2024b; R. E. Cohen et al. 2025; C. T. Garling et al. 2025). These works have demonstrated that WLM has been actively star-forming over most of its history, as expected for isolated, gas-rich dwarf galaxies, with the notable ex-

ception of a period of reduced star formation in the ~ 3 Gyr following reionization.

We utilize the public JWST/NIRCam photometric catalogs and artificial star tests (ASTs) for WLM that were released as part of the JWST Resolved Stellar Populations Early Release Science Program (D. R. Weisz et al. 2024). We apply photometric quality cuts following the recommendations of D. R. Weisz et al. (2024) such that filtered photometric catalog and ASTs should be essentially identical to those used by R. E. Cohen et al. (2025), who measured the global SFH of WLM and additionally examined spatially-resolved trends in SFH across the galaxy. We note that the global SFH measurement of R. E. Cohen et al. (2025) is also nearly identical to that of K. B. W. McQuinn et al. (2024b), who used the same measurement techniques (e.g., the MATCH code) with earlier versions of the photometry and ASTs prior to the public release.

We compare the observed Hess diagram of WLM with our best-fit MZH metallicity evolution model in Figure 2. The features in the residuals are largely the same as those shown in Figure 8 of C. T. Garling et al. (2025), which fit the SFH of WLM using the linear AMR model. As discussed in that work, the main areas of poor fit are

1. An excess of stars in the model along the red side of the RGB.
2. Large residuals around the red clump.
3. An excess of observed stars on the red side of the upper main sequence (e.g., $x = 0$, $y = 24$).
4. An excess of stars in the model on the blue side of the main sequence at faint magnitudes (e.g., $x = 0$, $y = 26.5$).

Similar residual patterns were observed by K. B. W. McQuinn et al. (2024b) who used the MATCH code to measure the resolved SFH from the same JWST/NIRCam data.

Table 2. Summary Statistics of SFH Measurements

τ	PARSEC + YBC	PARSEC + MIST	BaSTIv2 + YBC	BaSTIv2 + MIST	MIST + YBC	MIST + MIST
WLM						
τ_{10}	$11.50^{+0.08}_{-0.09}$	$11.69^{+0.04}_{-0.06}$	$12.49^{+0.04}_{-0.05}$	$12.28^{+0.05}_{-0.05}$	$12.54^{+0.02}_{-0.02}$	$13.21^{+0.01}_{-0.01}$
τ_{25}	$8.18^{+0.02}_{-0.03}$	$7.41^{+0.02}_{-0.03}$	$7.86^{+0.04}_{-0.05}$	$7.63^{+0.03}_{-0.03}$	$11.66^{+0.02}_{-0.02}$	$7.88^{+0.01}_{-0.02}$
τ_{50}	$4.68^{+0.07}_{-0.05}$	$4.68^{+0.12}_{-0.08}$	$4.74^{+0.02}_{-0.02}$	$4.64^{+0.02}_{-0.02}$	$5.81^{+0.04}_{-0.06}$	$5.39^{+0.05}_{-0.08}$
τ_{75}	$2.41^{+0.03}_{-0.01}$	$2.37^{+0.03}_{-0.02}$	$2.26^{+0.01}_{-0.01}$	$2.26^{+0.01}_{-0.01}$	$2.65^{+0.01}_{-0.01}$	$2.54^{+0.02}_{-0.01}$
τ_{90}	$1.24^{+0.01}_{-0.01}$	$1.21^{+0.01}_{-0.01}$	$1.14^{+0.01}_{-0.01}$	$1.08^{+0.01}_{-0.02}$	$1.12^{+0.01}_{-0.01}$	$1.09^{+0.01}_{-0.01}$
Leo A						
τ_{10}	$7.04^{+0.17}_{-0.07}$	$7.36^{+0.21}_{-0.17}$	$7.52^{+0.14}_{-0.09}$	$7.75^{+0.13}_{-0.06}$	$7.94^{+0.43}_{-0.03}$	$8.45^{+0.10}_{-0.08}$
τ_{25}	$5.36^{+0.05}_{-0.04}$	$5.38^{+0.06}_{-0.05}$	$5.69^{+0.09}_{-0.05}$	$5.79^{+0.09}_{-0.06}$	$5.97^{+0.07}_{-0.03}$	$5.94^{+0.12}_{-0.09}$
τ_{50}	$3.58^{+0.03}_{-0.04}$	$3.54^{+0.05}_{-0.07}$	$3.89^{+0.04}_{-0.04}$	$3.95^{+0.04}_{-0.04}$	$4.02^{+0.06}_{-0.04}$	$3.94^{+0.05}_{-0.05}$
τ_{75}	$2.18^{+0.01}_{-0.03}$	$2.16^{+0.01}_{-0.03}$	$2.32^{+0.02}_{-0.04}$	$2.30^{+0.03}_{-0.04}$	$2.38^{+0.03}_{-0.04}$	$2.33^{+0.02}_{-0.03}$
τ_{90}	$1.13^{+0.01}_{-0.05}$	$1.11^{+0.01}_{-0.04}$	$1.04^{+0.01}_{-0.02}$	$1.06^{+0.01}_{-0.02}$	$1.00^{+0.01}_{-0.04}$	$1.02^{+0.01}_{-0.03}$
Aquarius						
τ_{10}	$13.23^{+0.01}_{-0.02}$	$13.21^{+0.01}_{-0.02}$	$13.21^{+0.01}_{-0.03}$	$13.18^{+0.01}_{-0.04}$	$13.09^{+0.03}_{-0.04}$	$13.20^{+0.02}_{-0.05}$
τ_{25}	$8.87^{+0.25}_{-0.08}$	$8.86^{+0.09}_{-0.07}$	$12.35^{+0.09}_{-0.19}$	$12.15^{+0.07}_{-0.25}$	$9.79^{+0.04}_{-0.03}$	$10.89^{+0.81}_{-0.90}$
τ_{50}	$6.70^{+0.05}_{-0.10}$	$6.50^{+0.11}_{-0.12}$	$7.73^{+0.05}_{-0.15}$	$8.20^{+0.02}_{-0.14}$	$7.74^{+1.00}_{-0.56}$	$7.95^{+0.23}_{-0.65}$
τ_{75}	$4.26^{+0.03}_{-0.03}$	$4.27^{+0.03}_{-0.04}$	$4.76^{+0.04}_{-0.09}$	$4.77^{+0.06}_{-0.17}$	$4.75^{+0.08}_{-0.10}$	$4.53^{+0.35}_{-0.09}$
τ_{90}	$2.36^{+0.01}_{-0.04}$	$2.36^{+0.02}_{-0.04}$	$2.49^{+0.06}_{-0.05}$	$2.51^{+0.20}_{-0.05}$	$2.67^{+0.03}_{-0.03}$	$2.66^{+0.09}_{-0.05}$
Leo P						
τ_{10}	$13.29^{+0.01}_{-0.04}$	$13.28^{+0.01}_{-0.04}$	$13.09^{+0.03}_{-0.08}$	$13.06^{+0.03}_{-0.11}$	$13.30^{+0.01}_{-0.04}$	$13.32^{+0.01}_{-0.04}$
τ_{25}	$12.70^{+0.03}_{-0.10}$	$12.67^{+0.02}_{-2.86}$	$8.87^{+0.62}_{-0.21}$	$8.84^{+1.26}_{-0.28}$	$12.72^{+0.02}_{-0.10}$	$12.78^{+0.01}_{-0.10}$
τ_{50}	$5.81^{+0.31}_{-0.22}$	$5.84^{+0.12}_{-0.10}$	$5.30^{+0.15}_{-0.08}$	$5.46^{+0.38}_{-0.33}$	$6.17^{+0.09}_{-0.16}$	$5.96^{+0.16}_{-0.24}$
τ_{75}	$3.08^{+0.50}_{-0.09}$	$3.13^{+0.18}_{-0.08}$	$3.20^{+0.12}_{-0.46}$	$2.99^{+0.37}_{-0.12}$	$3.84^{+0.12}_{-0.16}$	$3.31^{+0.13}_{-0.12}$
τ_{90}	$1.62^{+0.09}_{-0.06}$	$1.62^{+0.07}_{-0.03}$	$1.37^{+0.12}_{-0.05}$	$1.40^{+0.18}_{-0.03}$	$1.91^{+0.15}_{-0.13}$	$1.45^{+0.13}_{-0.03}$

NOTE— τ_x values indicate the lookback time at which the galaxy formed x percent of its stellar mass – for example, τ_{10} indicates the lookback time at which the galaxy formed 10% of its total stellar mass. All values are in Gyr and all uncertainties are random (statistical) uncertainties. τ values measured under our new MZH metallicity evolution model assuming each combination of stellar track library (PARSEC, BaSTIv2, and MIST) and bolometric correction library (YBC and MIST) are given.

Our SFH and metallicity evolution measurements are shown in Figure 3. We present solutions under both the traditional linear AMR model and our new MZH metallicity evolution model. For comparison we also plot the solution of *K. B. W. McQuinn et al. (2024b)*, who measured the SFH of WLM with the same data using the MATCH code. On the upper right panel we overplot ages and metallicities for single red giant stars measured by combining our photometry with the spectroscopic metal-

licities of *R. Leaman et al. (2009)* using the method presented in §4.

We note first that the measurement we present here with the linear AMR model shows excellent agreement with our previous measurement in *C. T. Garling et al. (2025)* which used isochrones obtained from the PARSEC webform. Quantitatively, the differences between the two measurements are of similar magnitude to their respective random uncertainties, which are quite low as

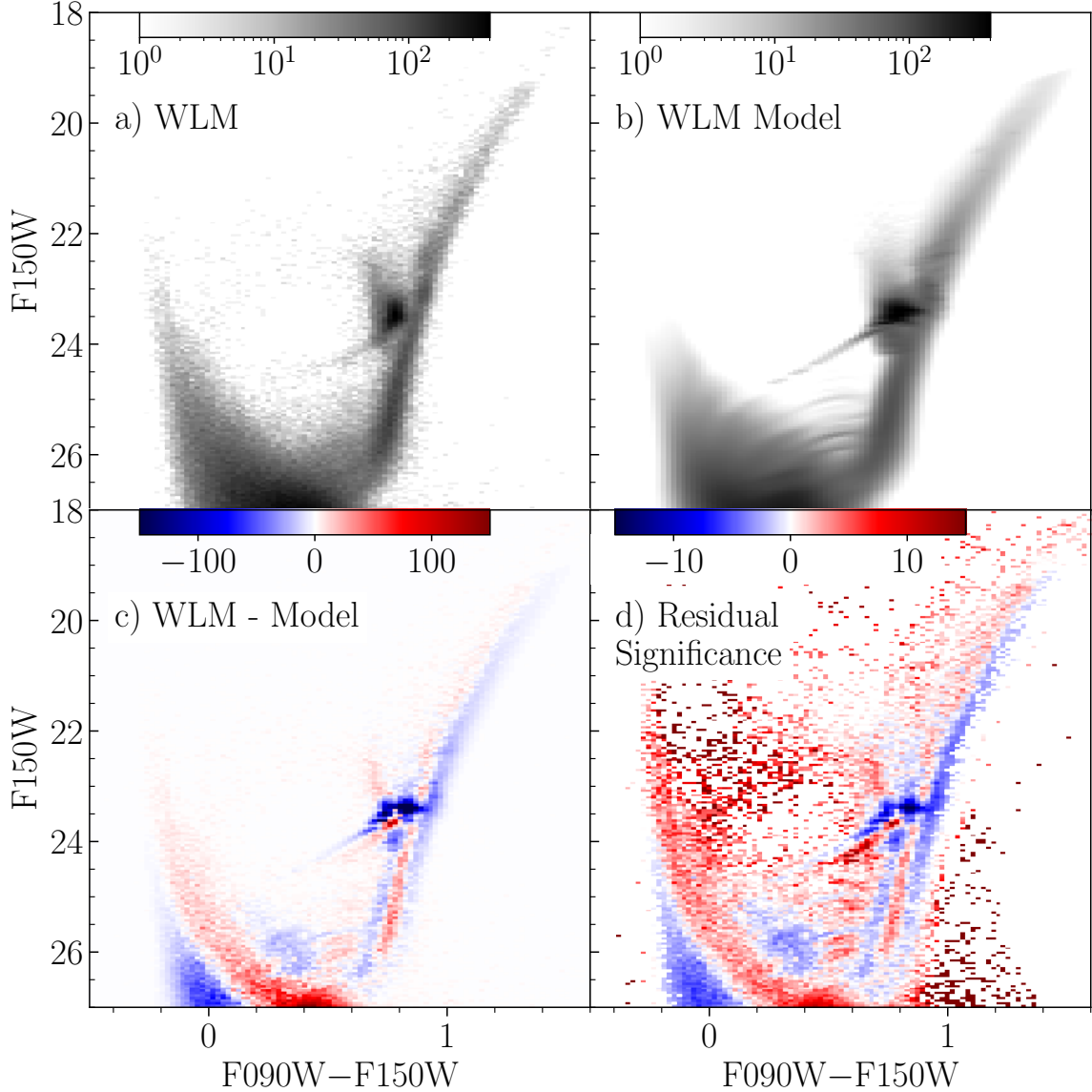


Figure 2. Comparison of the Hess diagram of WLM with our best-fit model. (a) Hess diagram of WLM constructed from the JWST/NIRCam photometric catalog of [D. R. Weisz et al. \(2024\)](#). (b) Best-fit model Hess diagram using our MZH metallicity evolution model with PARSEC stellar tracks and YBC bolometric corrections. (c) Residual between the observed Hess diagram and the best-fit model in raw star counts. (d) Residual between the observed Hess diagram and the best-fit model in units of standard deviations (i.e., the residual significance).

the CMD of WLM is densely populated. Note that in [Figure 3](#), the light shaded region shows the systematic uncertainty region, within which there is a much smaller random uncertainty region shaded more darkly. As the PARSEC stellar tracks and YBC BCs underlying the webform are mostly the same as those included in our interpolation routines presented in [§3.1](#) and [§3.2](#), the fact that the measurements agree so well provides a real-world demonstration that our new on-the-fly interpolation schemes perform as expected.

As in [C. T. Garling et al. \(2025\)](#), our measurement under the linear AMR model agrees quite well with that of [K. B. W. McQuinn et al. \(2024b\)](#). We find a linear AMR slope that is nearly identical and an intercept that is ~ 0.1 dex higher. Our result under the MZH model is somewhat different – the metallicity evolution converges to nearly the same metallicity at present-day, but prefers a lower metallicity at early times which results in some deviation from the linear AMR in the earliest time bins ($t > 10$ Gyr). Agreement with both [K. B. W. McQuinn et al. \(2024b\)](#) and our linear AMR model solution is still

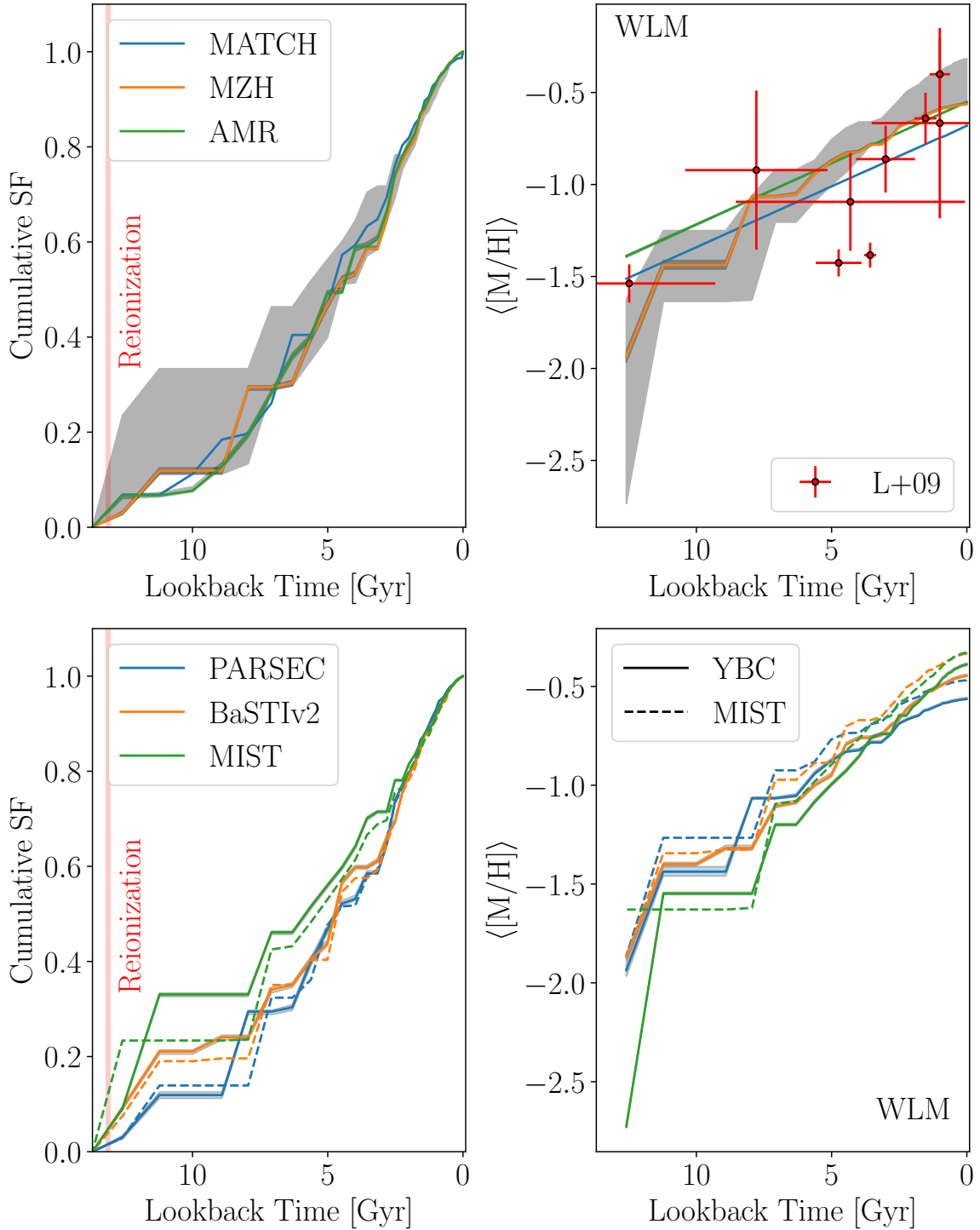


Figure 3. *Top row:* The cumulative SFHs (left) and AMRs (right) of WLM derived from the JWST/NIRCam imaging. Included are measurements with a linear AMR (green line) and with our hierarchical MZH model (orange line), both of which assume the PARSEC stellar models (§3.1) with the YBC bolometric corrections (§3.2). For comparison we also show the result of K. B. W. McQuinn et al. (2024b) (blue line), who used the MATCH code on the same data. The systematic uncertainty on the MZH SFH and metallicity evolution is shown as a light shaded region (see §3 for more details). The (much smaller) random uncertainty is shaded more darkly. Overplotted on the right panel are age and metallicity measurements for individual red giant stars obtained by combining the spectroscopic metallicities of R. Leaman et al. (2009) with our photometry (see §4). *Bottom row:* The six individual measurements of the SFH of WLM under the MZH model for different combinations of stellar tracks (PARSEC, MIST, and BaSTIv2) and bolometric corrections (MIST, YBC) that were used to define the systematic uncertainty region in the upper row. The PARSEC and BaSTIv2 tracks give fairly consistent results, while the MIST stellar tracks prefer more early star formation. The measurements under the MIST bolometric corrections prefer higher present-day metallicities (by ~ 0.1 dex) compared to the solutions with the YBC bolometric corrections.

quite good for the MZH model – as WLM has had relatively steady star formation over the last ~ 9 Gyr, our MZH model naturally produces a fairly linear relation between age and metallicity.

The systematic uncertainties shown in Figure 3 are measured using the method described in §3; in short, the MZH model is used to derive the SFH of WLM under each combination of three stellar model libraries (PARSEC, MIST, and BaSTIv2) and two bolometric corrections libraries (MIST, YBC). The individual solutions are shown in the bottom row of Figure 3 and show some interesting patterns. The MIST stellar tracks consistently prefer more early star formation compared to the PARSEC and BaSTIv2 stellar tracks. Quantified by τ_{50} , the lookback time at which the galaxy formed half of its stellar mass, PARSEC and BaSTIv2 are consistent with values of $4.68^{+0.07}_{-0.05}$ Gyr and $4.74^{+0.02}_{-0.02}$ Gyr respectively, while the MIST stellar tracks prefer a value $5.81^{+0.04}_{-0.06}$ Gyr, which is about a Gyr earlier. The differences in the SFH caused by varying the stellar tracks are larger than those caused by varying the BCs. However, the bottom right panel shows that the MIST BCs prefer systematically higher metallicities compared to the YBC BCs, though the difference is minor; the mean difference between solutions using different BC libraries when fixing the stellar track library is ~ 0.1 dex.

The upper right panel of Figure 3 also shows the ages and metallicities we measure for nine red giant stars in WLM by combining the spectroscopic metallicities of R. Leaman et al. (2009) with our photometry using the methodology described in §4. Unfortunately, these measurements are not very precise, due predominantly to the large metallicity uncertainties on the spectroscopic measurements of R. Leaman et al. (2009), which are typically $\sigma \geq 0.25$ dex. While there are few stars in the sample, and they have fairly high age and metallicity uncertainties, most of the stars lie around the AMRs found via resolved SFH fitting. We note that there are two outliers at $[M/H] \sim -1.5$ dex with ages ≤ 5 Gyr. These stars are on the extreme blue edge of the RGB in our JWST/NIRCam photometry, which has significant overlap with core helium burning blue loop stars. If these are blue loop stars, then the metallicity calibration for red giants used by R. Leaman et al. (2009) would be inappropriate, and so our metallicity prior for these stars would be incorrect, which could account for their deviation from the rest of the sample.

5.2. Aquarius

To extend our MZH results to lower stellar masses, we apply our MZH model to the Aquarius dwarf irregular galaxy ($M_v \approx -10.47$ mag, $M_* \approx 2.6 \times 10^6 M_\odot$,

A. W. McConnachie 2012) – as the present-day stellar mass of Aquarius is about an order of magnitude lower than that of WLM, Aquarius probes a different regime of $\langle [M/H] \rangle (M_*)$. However, Aquarius has several properties that are similar to WLM – both are isolated, gas-rich ($M_{\text{HI}}/M_* > 1$), and about 1 Mpc away (we assume $d = 977 \pm 45$ kpc for Aquarius; A. A. Cole et al. 2014). At this distance, the HST/ACS imaging presented in A. A. Cole et al. (2014) is deep enough to resolve the subgiant branch and enable measurements of lifetime SFHs. The SFH measurement presented in A. A. Cole et al. (2014) has poor time resolution by modern standards, but K. B. W. McQuinn et al. (2024a) applied the MATCH code to the same HST/ACS data to derive an independent SFH measurement with better time resolution (equal, in fact, to the time resolution of the WLM SFH measurements of K. B. W. McQuinn et al. 2024b; R. E. Cohen et al. 2025). We use the same photometric catalogs and ASTs (including quality cuts) as used by K. B. W. McQuinn et al. (2024a) for our analysis here.

We compare the observed Hess diagram of Aquarius with our best-fit MZH model in Figure 4. In our discussion of the WLM fit (Figure 2), we noted a color offset between the model and the data along the upper RGB. In comparison, the upper RGB of Aquarius is very well fit, while the lower RGB (fainter than the red clump) in the model Hess diagram of Aquarius exhibits a minor color offset. Residuals around the red clump remain large, as was the case for WLM. We observe a less significant, but still present, excess of model stars on the blue side of the faint MS. Similar residual patterns can be seen in Figure 3 of A. A. Cole et al. (2014) showing their model Hess diagram for Aquarius.

Our SFH and metallicity evolution measurements are shown in Figure 5. We present solutions under both the traditional linear AMR model and our new MZH metallicity evolution model. We also show the solution of K. B. W. McQuinn et al. (2024b), who measured the SFH of Aquarius with the same data using the MATCH code. While our measurements are statistically consistent with those of K. B. W. McQuinn et al. (2024b), there are a few differences between our measurements that are apparent. While we reproduce the pause in star formation from roughly 10–13 Gyr ago noted by K. B. W. McQuinn et al. (2024a), our measurements find larger initial bursts of star formation. In our fiducial MZH measurement, we find that Aquarius formed $\sim 25\%$ of its stellar mass in the first 2 Gyr of cosmic time, while K. B. W. McQuinn et al. (2024a) found that only $\sim 10\%$ of the stellar mass formed in this period. In our measurement, this difference is compensated by lower average SFR from 5–8 Gyr ago com-

pared to K. B. W. McQuinn et al. (2024a). Therefore, the average age of stars in Aquarius is slightly older in our measurement compared to K. B. W. McQuinn et al. (2024a). As older stellar populations have higher stellar mass-to-light ratios, we find a slightly higher total stellar mass formed in Aquarius of $4.35_{-0.41}^{+0.58} \times 10^6 M_{\odot}$, while K. B. W. McQuinn et al. (2024a) find $3.9 \times 10^6 M_{\odot}$.

We perform an independent check of the metallicity evolution found in our resolved SFH fit by comparing against the ages and metallicities of individual red giant stars following the methods in §4. E. N. Kirby et al. (2017) measured the metallicities of 23 RGB stars from Keck/DEIMOS spectra and found a median $[\text{Fe}/\text{H}] = -1.49$ dex with standard deviation 0.37 dex. Later, L. Hermosa Muñoz et al. (2020) measured the metallicities of 53 RGB stars from VLT/FORS2 spectra and found a median $[\text{Fe}/\text{H}] = -1.58$ dex with standard deviation 0.29 dex. By combining these spectroscopic metallicity measurements with our high-precision photometry we are able to measure the ages of the stars that fall within the HST/ACS field of view. These single-star age and metallicity measurements are shown overplotted on the upper right panel of Figure 5. At older ages (> 8 Gyr ago), the single-star measurements have slightly higher metallicities compared to the resolved SFH result (~ 0.2 dex). We note that seven of the eight stars with measured ages < 2 Gyr are found to have ages ~ 1 Gyr, which is the youngest age allowed by our prior. If we allow younger ages for these stars we obtain better fits (statistically speaking), but this is physically unlikely given that these stars are selected to be on the upper RGB. Overall, the young stars for which we measure ages ≈ 1 Gyr are likely not well fit, and so their metallicities and ages may not be reliable. Overall, the majority of the stars in the sample have intermediate ages (2 – 8 Gyr ago) and show excellent agreement with the results from the resolved SFH fits.

5.3. *Leo A*

Leo A is of similar stellar mass to Aquarius with $M_{*} \approx 1.3 \times 10^6 M_{\odot}$ (K. B. W. McQuinn et al. 2024a) and is similarly isolated and gas-rich ($M_{\text{HI}}/M_{*} \geq 2$; D. A. Hunter et al. 2012; A. W. McConnachie 2012; M. E. Putman et al. 2021). The first global SFH for Leo A was presented by A. A. Cole et al. (2007) based on HST/ACS observations in the F475W and F814W filters. These data were recently reanalyzed by K. B. W. McQuinn et al. (2024a), who used MATCH to derive a new SFH with improved time resolution. We utilize the same photometric catalogs and ASTs as were used by K. B. W. McQuinn et al. (2024a) to facilitate compari-

son between our work. We take the distance of Leo A to be 798 ± 44 kpc ($\mu = 24.51 \pm 0.12$ mag) based on measurements of standard candle RR Lyrae stars by A. E. Dolphin (2002). This measurement is generally consistent with others from the literature measured via other methods, such as the TRGB magnitude (E. J. Bernard et al. 2013) and Cepheid variable stars (G. A. Tammann et al. 2011; E. J. Bernard et al. 2013).

Figure 6 compares the observed Hess diagram of Leo A with our best-fit MZH metallicity evolution model. Overall, the residual patterns we observe are very similar to those we saw in Aquarius (Figure 4). Of particular note in Leo A is the significant population of young, high-mass main sequence stars – these are reasonably fit in our model, but the upper main sequence in the data is noticeably broader than in the model. This has been noted in previous works and improved fits may be obtained by randomly adding extinction to the young stars in order to broaden and redden the main sequence (e.g., A. E. Dolphin et al. 2003; S. M. Albers et al. 2019). We experimented with this approach and found that it could reduce the statistical significance of the residuals on the upper main sequence, but it did not noticeably affect the overall SFH or metallicity evolution results. Additionally, as all of the galaxies studied in this work are low metallicity and therefore likely to be dust-poor, it is unclear from a physical standpoint what model one should use for the distribution of extinction values to apply to young stars. Therefore, we do not include such age-dependent differential extinction in our models here.

From spectroscopy of young blue supergiants, the metallicity of Leo A is estimated to be $[\text{M}/\text{H}] \approx -1.35$ dex (M. A. Urbaneja et al. 2023). The young stars appear to have solar α -element abundance patterns as the oxygen abundance is consistent with the overall metallicity; $12 + \log(\text{O}/\text{H}) = 7.4 \pm 0.2$ has been measured from HII regions (L. van Zee et al. 2006; F. Ruiz-Escobedo et al. 2018), corresponding to roughly $[\text{O}/\text{H}] \approx -1.3$ dex. E. N. Kirby et al. (2017) measured spectroscopic metallicities of 113 RGB stars and found a median $[\text{Fe}/\text{H}] = -1.59$ dex with standard deviation 0.35 dex. This is only ~ 0.2 dex lower than the metallicities of the young supergiants, indicating that the chemical evolution of Leo A has been slow in comparison to other galaxies of similar stellar mass. A slow chemical evolution is also implied by the AMR measured by E. N. Kirby et al. (2017) based on single-star age and metallicity estimates (see their Figure 12). This conclusion is consistent with the AMR fit by A. A. Cole et al. (2007) in their resolved SFH measurement – they find the data can be adequately explained with a constant metallicity of $[\text{M}/\text{H}] = -1.4 \pm 0.2$ dex.

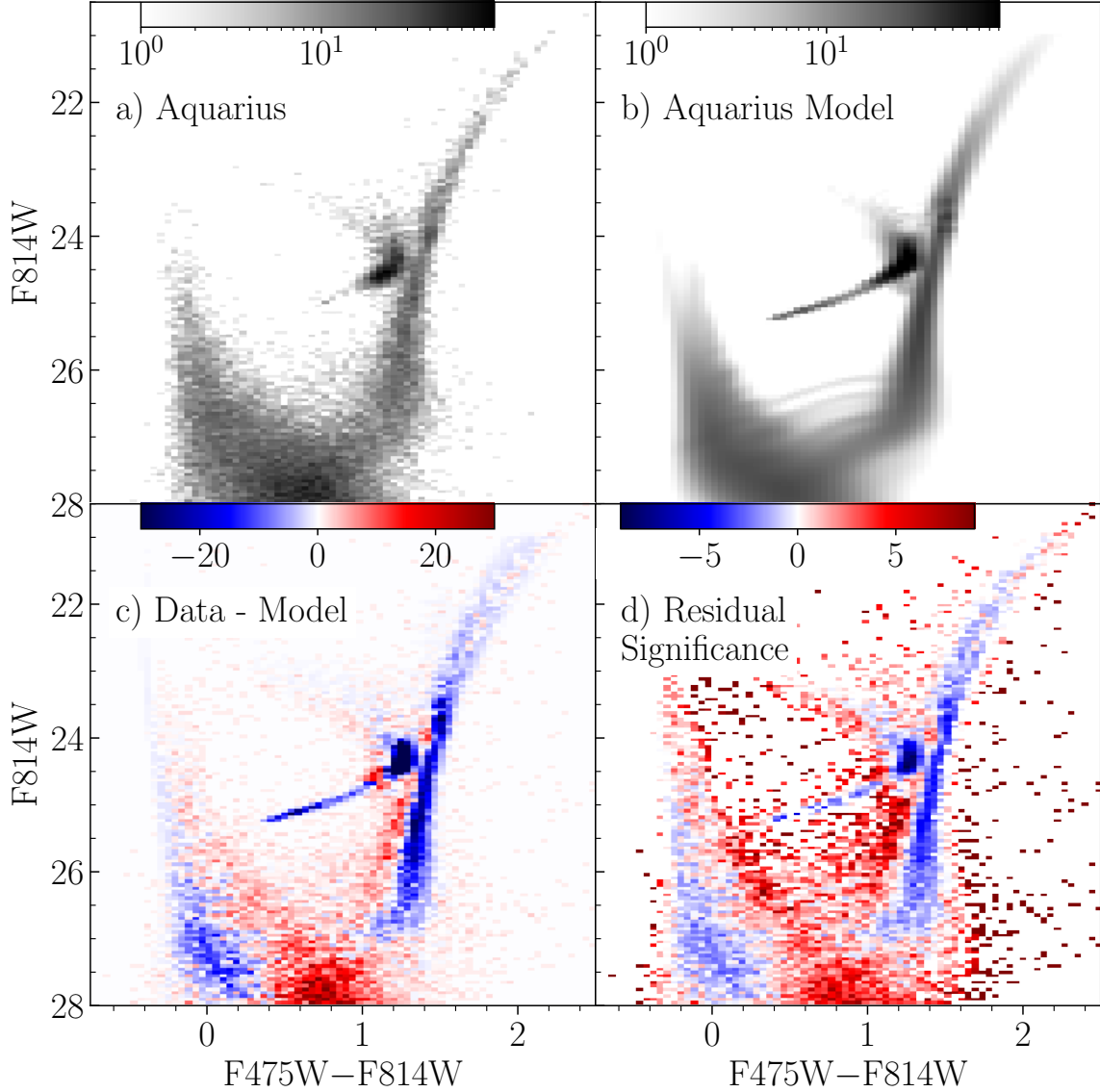


Figure 4. Comparison of the Hess diagram of Aquarius with our best-fit model. The panels follow the same layout as in Figure 2.

In contrast, our best-fit resolved SFH solution under the MZH model, shown in Figure 7, shows significant metallicity evolution – this measurement indicates that stars formed > 10 Gyr ago in Leo A should have metallicities $[M/H] \sim -2.0$ dex, while stars forming in Leo A at present-day have metallicities $[M/H] \sim -1.3$ dex, in good agreement with the metallicity measurements of young supergiants by *M. A. Urbaneja et al. (2023)*. The AMR fit of *K. B. W. McQuinn et al. (2024a)* also prefers substantial metallicity evolution. Using the methodology of §4 we leverage the spectroscopic metallicities of *E. N. Kirby et al. (2017)* in combination with our high-precision HST/ACS photometry to measure ages for single red giant stars in Leo A in order to perform an independent check of the AMR. We note that our photome-

try is much more precise than the ground-based photometry that *E. N. Kirby et al. (2017)* used to estimate ages for these stars – the random errors on the HST/ACS photometry for these bright red giants is typically less than 0.02 mag. Shown overplotted in the upper right panel of Figure 7, these single star ages illustrate that the old stars of Leo A (> 5 Gyr old) do indeed have low metallicities (< -1.8 dex). Overall, the single star measurements agree very well with the metallicity evolution from the resolved SFH.

The previous results favoring little metallicity evolution may be understood as a result of Leo A showing very little early star formation. Compared to other galaxies of similar present-day stellar mass, the bulk of Leo A’s stellar mass has been formed relatively recently

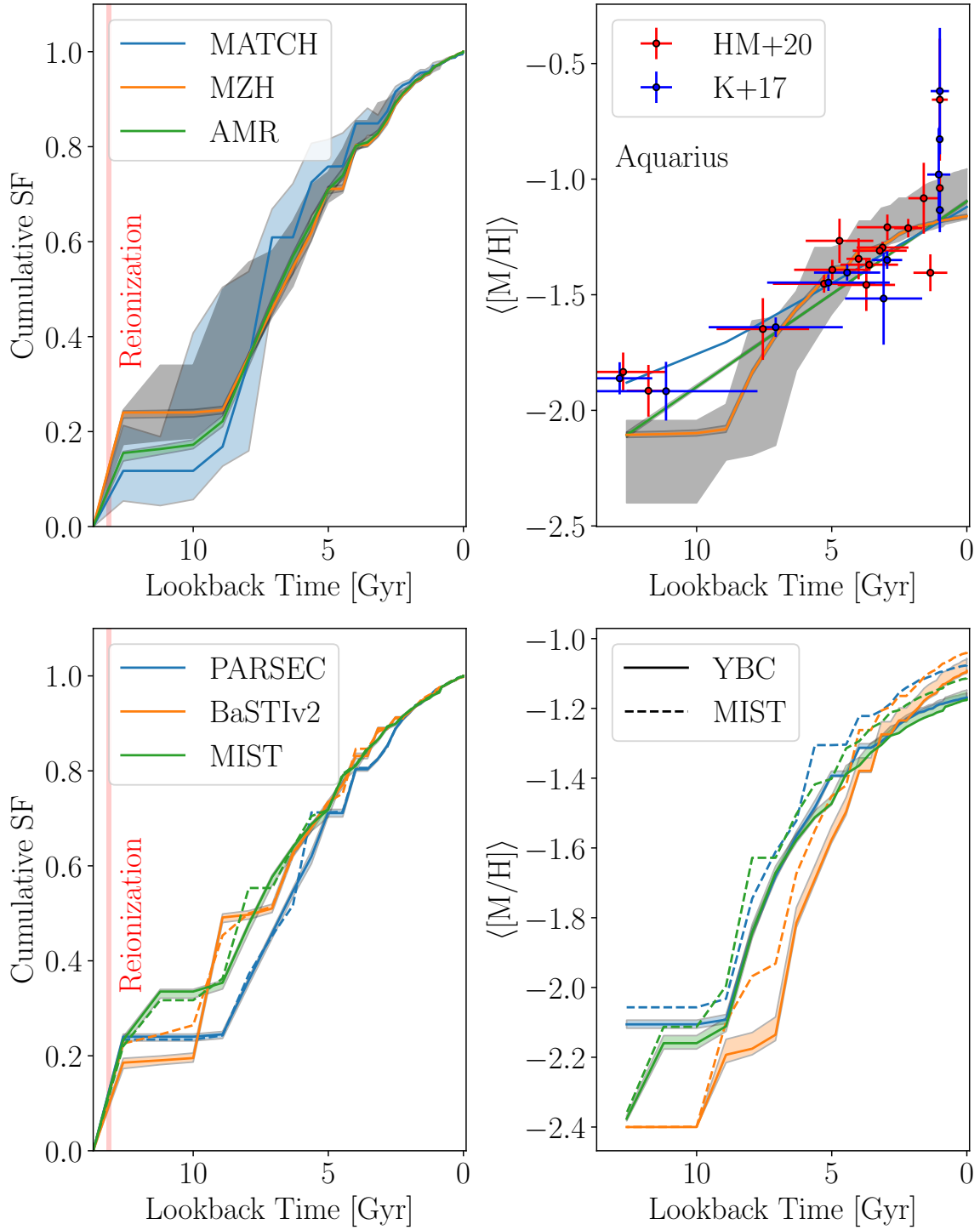


Figure 5. The results of our resolved SFH and metallicity evolution fit for Aquarius based on the HST/ACS data following the same format as Figure 3. In the top row the result of *K. B. W. McQuinn et al. (2024a)* (blue line), who used the MATCH code on the same data, is shown for comparison. Overplotted on the upper right panel are age and metallicity measurements for individual red giant stars obtained by combining the spectroscopic metallicities of *L. Hermosa Muñoz et al. (2020)* (HM+20, red) and *E. N. Kirby et al. (2017)* (K+17, blue) with our photometry (see §4).

– about 80% of its stellar mass was formed in the last 5 Gyr. As a result, there are many more young stars (ages < 5 Gyr) on the upper RGB than old stars. We illustrate this in Appendix A by generating a Monte Carlo simulation of the CMD of Leo A assuming our best-fit SFH. We then examine the age distribution of stars that lie on the upper RGB, where the spectroscopic sample of E. N. Kirby et al. (2017) lies. Our mock CMD predicts that roughly 19% of stars on the upper RGB should have ages > 5 Gyr; this is in reasonable agreement with the observations, as only 14% of the stars for which we measure ages are older than 5 Gyr. Given the paucity of bright, old stars in Leo A, it is understandable that its metallicity evolution has been difficult to measure accurately.

5.4. *Leo P*

Leo P is less massive ($M_* \approx 5.7 \times 10^5 M_\odot$; K. B. W. McQuinn et al. 2024a) and more metal-poor ($Z \approx 0.03 Z_\odot$; E. D. Skillman et al. 2013) than the other galaxies in this section, extending our census of the metallicity evolution of dwarf galaxies. Leo P is isolated and gas-rich ($M_{\text{HI}}/M_* \approx 2$; E. Z. Bernstein-Cooper et al. 2014) but is more distant than the other galaxies in our sample with $d \approx 1.62 \pm 0.15$ Mpc ($\mu = 26.05 \pm 0.20$ mag; K. B. W. McQuinn et al. 2015).

The resolved SFH of Leo P was measured with HST/ACS data by K. B. W. McQuinn et al. (2015) and remeasured with new JWST/NIRCam data by K. B. W. McQuinn et al. (2024a). While the SFHs of the two measurements are fairly consistent, the metallicity models differ – both solutions find a flat (or nearly flat) AMR, but the HST/ACS data prefer a metallicity $[M/H]$ between -1.6 and -1.7 dex (see Figure 8 of K. B. W. McQuinn et al. 2015) while the JWST/NIRCam data prefer a higher metallicity between -1.4 and -1.2 dex (see Figure 7 of K. B. W. McQuinn et al. 2024a). Presently the best estimate of the metallicity of Leo P comes from the oxygen abundance of its single known HI region, $12 + \log(O/H) = 7.17 \pm 0.04$ (E. D. Skillman et al. 2013), corresponding to roughly $[O/H] \approx -1.5$ dex. Spectroscopy targeting candidate massive stars in Leo P was presented by C. J. Evans et al. (2019), but these data were insufficient to measure stellar metallicities. Spectroscopy of a bright O star in Leo P was presented by O. G. Telford et al. (2024) who found that the star’s metallicity is consistent with the nebular oxygen abundance and that no internal extinction due to dust in Leo P is required to fit the star’s spectral energy distribution.

In Figure 8 we compare the observed Hess diagram of Leo P with our best-fit MZH metallicity evolution model. The model fits the data reasonably well, with

the main area of disagreement being the color of the upper RGB – in the model Hess diagram, the upper RGB (brighter than the red clump) is noticeably redder than in the data. This mismatch is also present in the models presented by K. B. W. McQuinn et al. (2024a) (see their Figure 6).

As Leo P is fainter and more distant than the other galaxies in our sample, the random uncertainties in the SFH solution are accordingly larger. This is illustrated in Figure 9, where we present our SFH and metallicity evolution measurements using our new MZH model. Our fiducial solution agrees well with that of K. B. W. McQuinn et al. (2024a), though our solution prefers a larger initial burst of star formation and does not show the same burst in star formation 10 Gyr ago as found by K. B. W. McQuinn et al. (2024a). We find negligible metallicity evolution under all combinations of stellar tracks and BCs except for the combination of MIST stellar tracks and MIST BCs. Interestingly, our fit prefers a higher metallicity of roughly $-0.9^{+0.1}_{-0.2}$ dex – the SFH measurement of K. B. W. McQuinn et al. (2024a) also found negligible metallicity evolution, but they measured $[M/H]$ between -1.4 and -1.2 dex, although they only included isochrones in their model with metallicities $[M/H] \leq -0.9$ dex. Both measurements prefer a higher metallicity than implied by the oxygen abundance of the single HII region in Leo P of $[O/H] \approx -1.5$ dex (E. D. Skillman et al. 2013). To explore this discrepancy, we performed experiments fixing the variables describing the metallicity evolution to better match that measured from the HII region with results shown in Appendix B. Assuming $[M/H] \approx -1.5$ dex gives a better fit to the upper RGB, but results in a poorer fit on the lower RGB and the upper main sequence. As there are many more stars in these areas than on the upper RGB, the overall fit quality is worse when assuming $[M/H] \approx -1.5$ dex than in our fiducial model. Overall, the metallicity of Leo P’s stellar population is poorly constrained as there are no spectroscopic measurements available for red giants in Leo P as there are for the other galaxies in our sample. Future work probing the stellar metallicities of Leo P is needed to understand this discrepancy.

6. HISTORICAL MASS-METALLICITY HISTORIES FROM THEORY

The MZH is an important point of comparison between observations and theory as stellar feedback processes regulate the enrichment of the ISM. These stellar feedback models have significant uncertainties and the strength of stellar feedback varies considerably between different galaxy evolution models, leading to differences

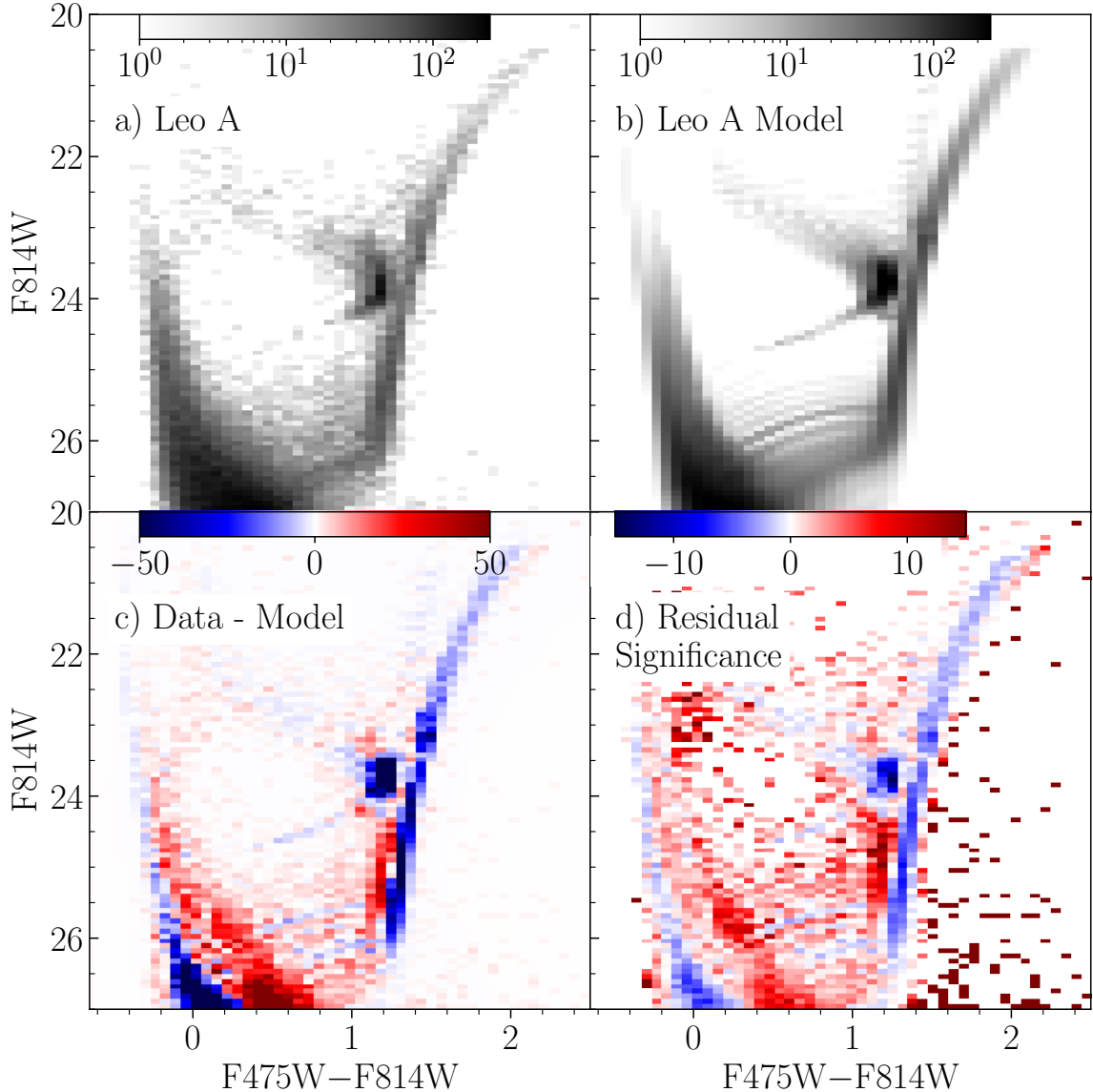


Figure 6. Comparison of the Hess diagram of Leo A with our best-fit model. The panels follow the same layout as in Figure 2.

in ISM metal abundances of a factor of two or more for massive galaxies ($M_* \geq 10^9 M_\odot$; see, e.g., Figure 10 of [S. Roca-Fàbrega et al. 2024](#)). We expect these differences to be even more significant for low-mass dwarf galaxies as their dark matter halos have shallower potential wells, allowing for significant metal-loaded outflows in models with strong stellar feedback (e.g., [A. L. Muratov et al. 2015, 2017](#); [C. R. Christensen et al. 2016, 2018](#); [D. Nelson et al. 2019](#); [P. D. Mitchell et al. 2020](#); [V. Pandya et al. 2020, 2021](#); [M. P. Rey et al. 2025](#)). Therefore, observationally probing the MZH at dwarf scales using our SFH-informed methodology can constrain stellar feedback models, but only if the observations and theoretical models are compared in a consistent way.

Observationally, traditional MZR are typically measured from statistical samples of galaxies with different stellar masses in small redshift bins (e.g., [B. H. Andrews & P. Martini 2013](#); [G. A. Blanc et al. 2019](#); [M. Curti et al. 2020](#)) – in the limit of infinitesimally small redshift bins, this amounts to measuring metallicity as a function of stellar mass at fixed time. The MZR measured from theoretical sources (e.g., cosmological hydrodynamic simulations and semi-analytic models) mirror this design (e.g., [X. Ma et al. 2016](#); [R. Davé et al. 2019](#); [P. Torrey et al. 2019](#); [L. Bassini et al. 2024](#); [S. Roca-Fàbrega et al. 2024](#); [A. Marszewski et al. 2024, 2025](#)). In contrast, our MZH model is historical – it models the metallicity of stars forming at time t as a function of the total stellar mass formed prior to t . As such, the only

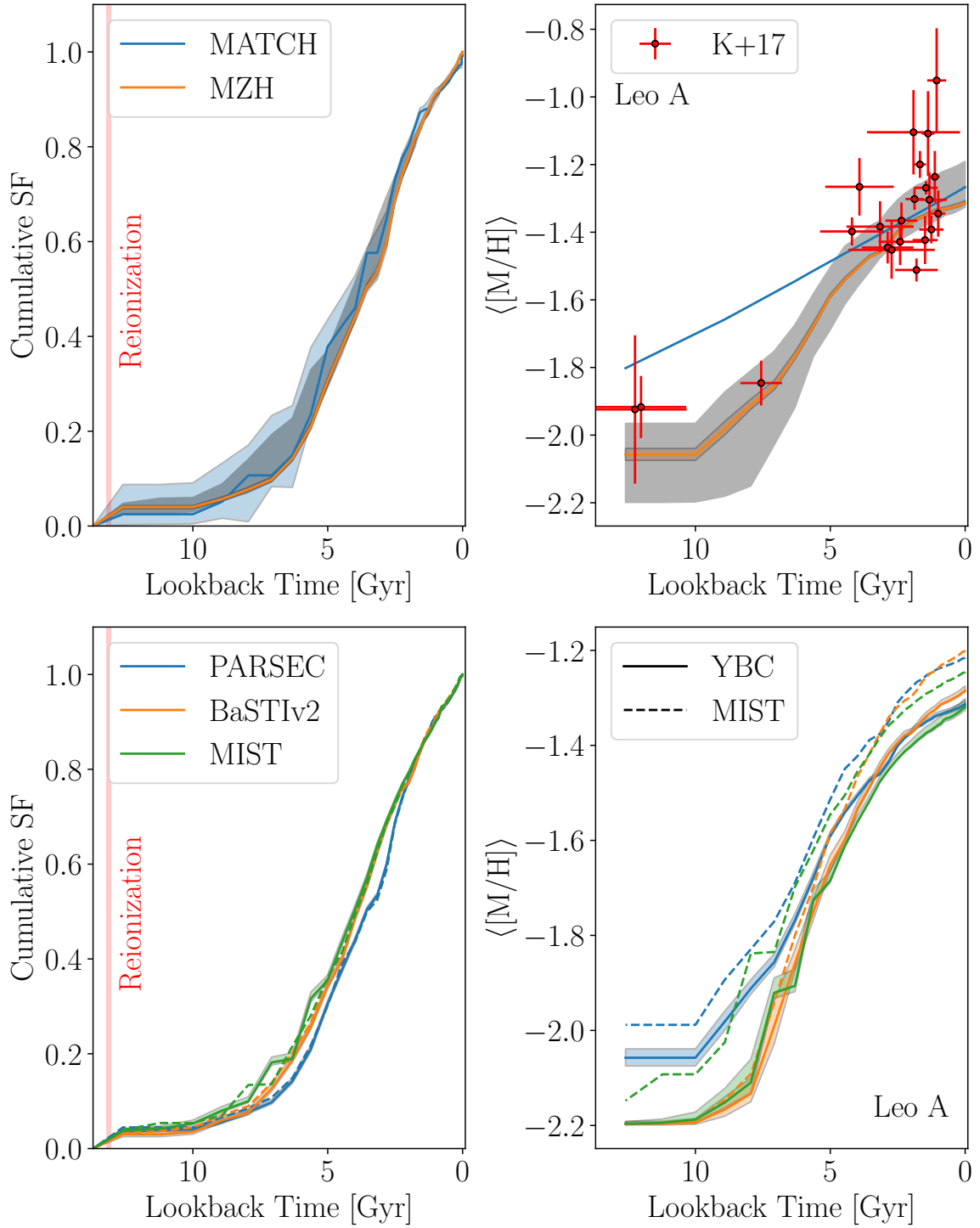


Figure 7. The results of our resolved SFH and metallicity evolution fit for Leo A based on the HST/ACS data following the same format as Figure 3. In the top row the result of *K. B. W. McQuinn et al. (2024a)* (blue line), who used the MATCH code on the same data, is shown for comparison. Overplotted on the upper right panel are age and metallicity measurements for individual red giant stars obtained by combining the spectroscopic metallicities of *E. N. Kirby et al. (2017)* with our photometry (see §4).

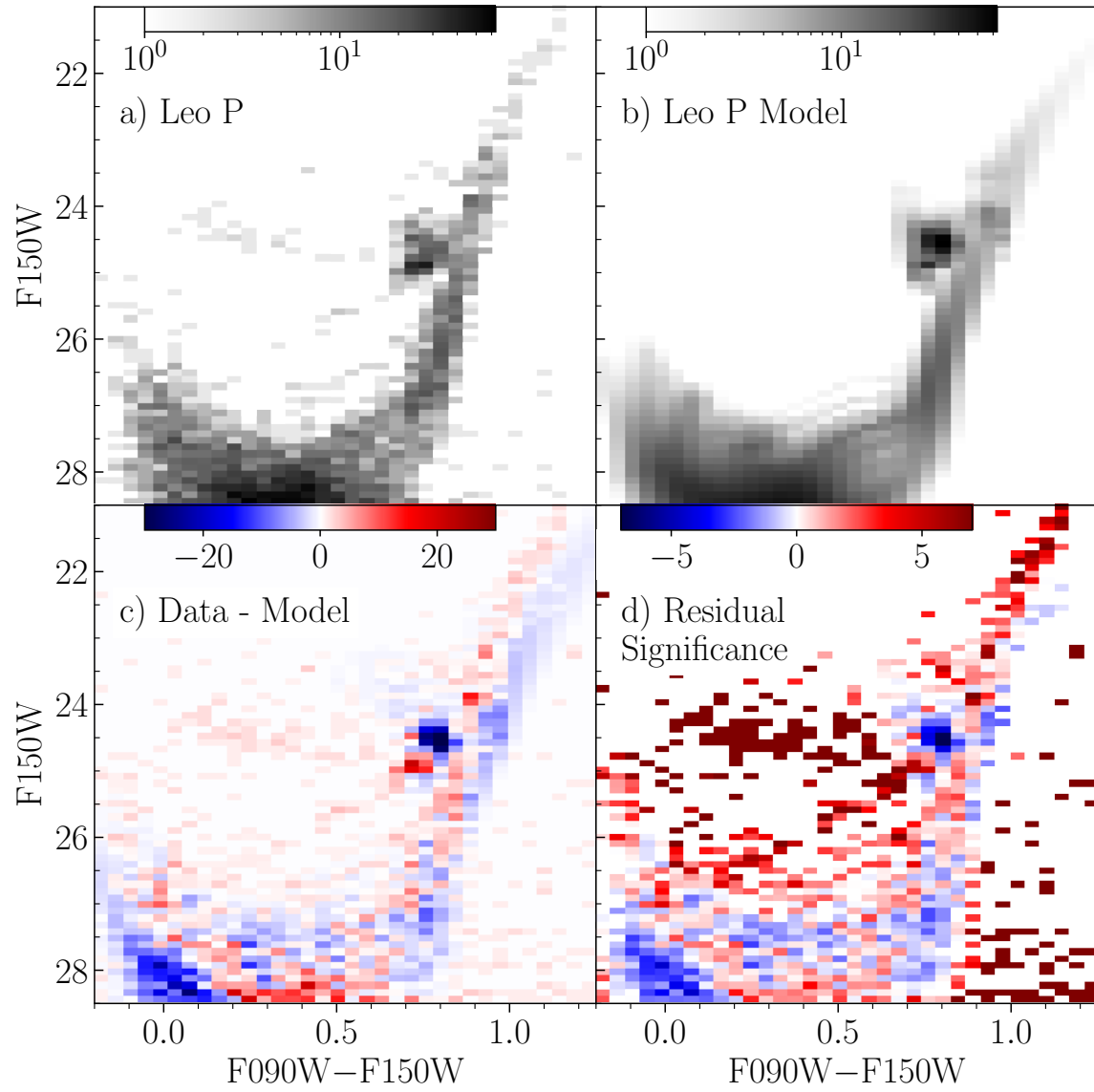


Figure 8. Comparison of the Hess diagram of Leo P with our best-fit model. The panels follow the same layout as in Figure 2.

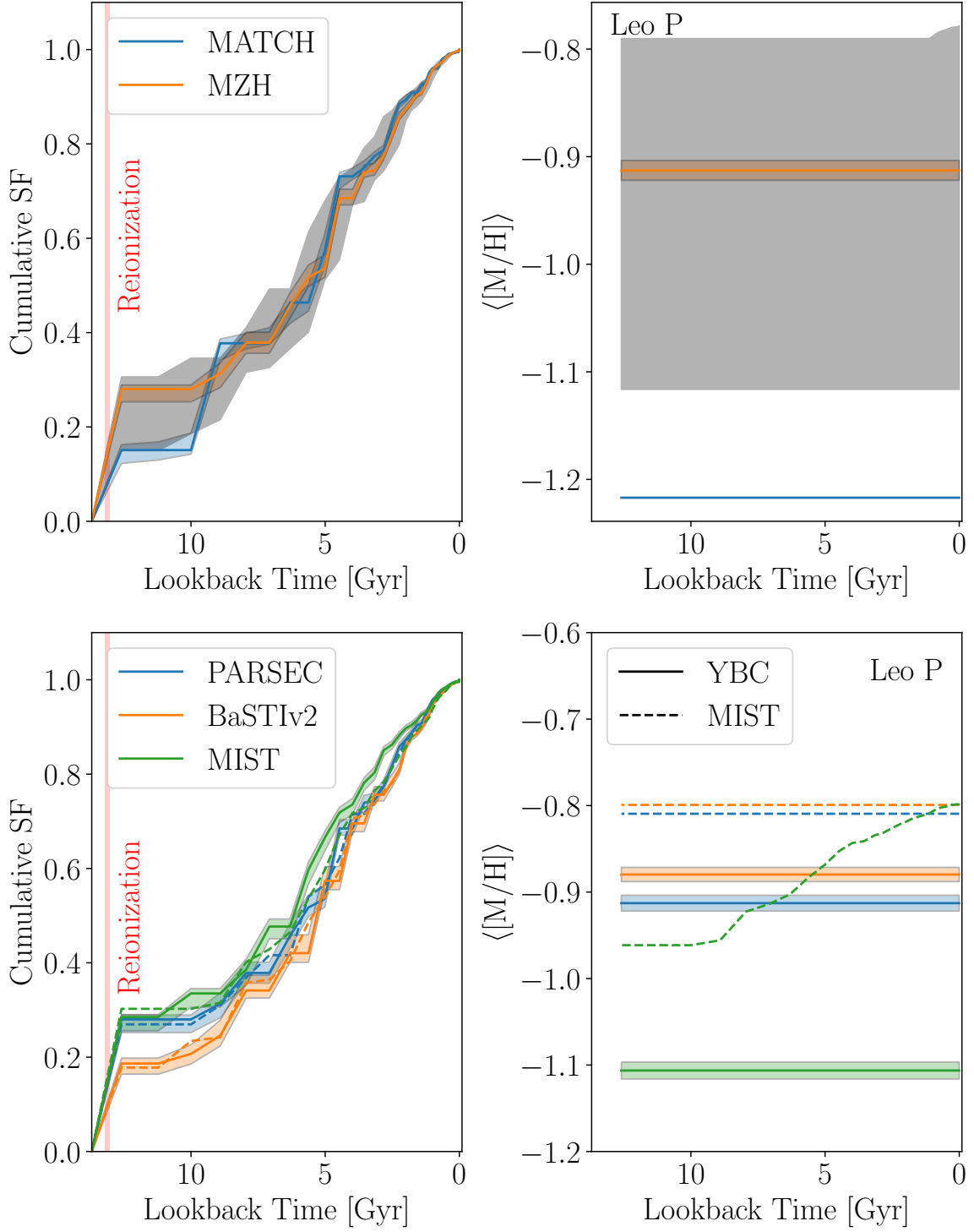


Figure 9. The results of our resolved SFH and metallicity evolution fit for Leo P based on the JWST/NIRCam data following the same format as Figure 3. In the top row the result of K. B. W. McQuinn et al. (2024a) (blue line), who used the MATCH code on the same data, is shown for comparison.

time-dependent parameters of our model are the SFRs. We must therefore analyze the theoretical data in the same historical fashion to derive MZHs that mirror the definition we use in our model.

To provide context and comparisons to our observational results, we analyze the TNG50 (D. Nelson et al. 2019; A. Pillepich et al. 2019) and FIREbox (R. Feldmann et al. 2023) cosmological hydrodynamic simulations, as well as results from the GALACTICUS (A. J. Benson 2012; N. Ahvazi et al. 2024) semi-analytic model. While TNG50 uses a galaxy evolution model whose stellar feedback is relatively smooth, the stellar feedback model used in FIREbox is comparatively bursty and drives stronger mass- and metal-loaded outflows in dwarf galaxies (A. L. Muratov et al. 2015; D. Nelson et al. 2019; V. Pandya et al. 2021). Given the differences in the models, it is reasonable to expect their MZHs may differ at dwarf scales. We additionally consider GALACTICUS to contrast the predictions of a state-of-the-art semi-analytic model with the aforementioned hydrodynamical simulations. GALACTICUS is somewhat unique amongst semi-analytic models in how much attention has been given to improving its agreement with observations at dwarf scales (e.g., S. Weerasooriya et al. 2023, 2024; N. Ahvazi et al. 2024) making it particularly interesting for our application.

In this section we will describe our methodologies for measuring the MZHs from the theoretical data in order to mirror the definition of the MZH used in our observational work. We then present the measured MZHs in §7 and discuss how the results compare amongst the theoretical models and against the observational results.

6.1. Analog Selection

As neither TNG50 nor FIREbox have sufficient baryonic resolution to resolve low-mass dwarf galaxies with $M_* \leq 10^6 M_\odot$, we are limited to considering higher mass dwarf galaxies. These simulations do have sufficient resolution to study analogs of the WLM dwarf irregular, which has $M_* \approx 4.3 \times 10^7 M_\odot$ —we therefore choose to focus our theoretical analysis on analogs of WLM to compare against the MZH we measured for WLM from JWST/NIRCAM photometry in §5.

Since it is known that the classical MZR exhibits secondary correlations with other galaxy properties in several galaxy evolution models (e.g., specific star formation rate and ISM gas mass; see, for example, S. J. Lilly et al. 2013; R. Davé et al. 2019; P. Torrey et al. 2019; A. M. Garcia et al. 2024b, 2025b), we first select galaxies from the theoretical data that resemble WLM in several important ways. All selection criteria are imposed at present-day. We select only central galaxies in the the-

oretical data since WLM is not a satellite of a more massive host galaxy. We further select only galaxies with stellar masses in the range $7 \leq \log(M_* [M_\odot]) \leq 9$ to ensure that the selected galaxies are of similar stellar mass to WLM. As WLM is actively forming stars (e.g., S. M. Albers et al. 2019; K. B. W. McQuinn et al. 2024b; C. T. Garling et al. 2025), we further select only galaxies with specific star formation rates (i.e., star formation rate per unit stellar mass) greater than 10^{-11} yr^{-1} . Like most star-forming dwarf galaxies, WLM is relatively gas-rich with a ratio of gas mass to stellar mass of order unity (A. A. Kepley et al. 2007; R. Ianjamasimanana et al. 2020). We therefore select only galaxies with $M_{\text{gas}}/M_* \geq 0.75$ to ensure the simulated galaxies are similarly gas-rich.

6.2. TNG50

The IllustrisTNG galaxy evolution model (A. Pillepich et al. 2018) was purpose-built to enable simulation of large cosmological volumes with magnetohydrodynamics. As such, it uses a subgrid star formation model that forms stars stochastically in gas denser than $n_{\text{H}} \simeq 0.1 \text{ cm}^{-3}$ following an empirical Kennicutt-Schmidt relation (V. Springel & L. Hernquist 2003). Generally speaking, the IllustrisTNG model is designed to operate at resolutions insufficient to resolve the dense molecular clouds where most star formation is thought to occur ($n_{\text{H}} \geq 100 \text{ cm}^{-3}$). The computational efficiency of these methods has allowed IllustrisTNG to be run in cosmological volumes with resolutions sufficient to resolve dwarf galaxies.

The TNG50 simulation (D. Nelson et al. 2019; A. Pillepich et al. 2019) applies the IllustrisTNG galaxy formation and evolution model (R. Weinberger et al. 2017; A. Pillepich et al. 2018) to a cosmological volume of $(51.7 \text{ Mpc})^3$ with a baryon particle mass of $8.5 \times 10^4 M_\odot$ which is sufficient to resolve isolated dwarf galaxies like WLM with $\sim 10^3$ star particles. The MZR was studied in the larger volume, lower resolution TNG100 simulation by P. Torrey et al. (2019) who found good agreement with observations for galaxies with $M_* \geq 10^9 M_\odot$ (see their Figure 6). The MZR and the fundamental metallicity relation in the IllustrisTNG model were compared to results from other galaxy evolution models in A. M. Garcia et al. (2024b, 2025b). Below we describe the procedure used to measure the MZH (metallicity as a function of cumulative stellar mass *regardless of time*) for comparison to our observational results.

We first perform the analog selection described in §6.1 to identify galaxies in TNG50 that resemble WLM. We identify 6261 galaxies in the simulation that pass our selection criteria. Our subsequent procedure is similar

to that developed in section 4.2 of I. Escala et al. (2018) to measure dispersions in stellar metallicities in FIRE-2 simulations. Each star particle in TNG50 is tagged at birth with its formation time and metallicity. The metallicity of the star particle is inherited from its progenitor gas particle and therefore reflects the metallicity of the star-forming ISM at the time it was formed. Given the population of star particles in a galaxy at present-day, one can fully reconstruct the stellar mass of the galaxy over time ($M_*(t)$) under the assumption of in-situ star formation. As such, if star particle i was formed at time t_i with metallicity Z_i , we can correlate time t_i with a total stellar mass of $M_*(t_i)$, allowing us to form the MZH that we require ($Z(M_*)$). While there is likely to be some contamination due to star particles formed ex-situ (i.e., in other galaxies that were later accreted), I. Escala et al. (2018) found that $\geq 98\%$ of star particles in their sample of isolated dwarf galaxies had formed in-situ, indicating that contamination from ex-situ stars should be minimal.

Considering the above, we proceed as follows. For each of the 6261 galaxies that pass our selection criteria, we use the SUBFIND V. Springel et al. (2001) halo catalog to identify star particles bound to the galaxy at present-day and extract their formation times and metallicities. We then form $M_*(t)$ and $Z(t)$ by discretizing the formation times of the star particles onto a regular grid. For each time bin, the total stellar mass formed in the time bin is simply the sum of the birth stellar masses of all particles formed in the time bin. Calculating the birth mass of a star particle is non-trivial as star particles in TNG50 and FIREbox have non-uniform birth stellar masses and the mass decreases over time following models of the mass loss from evolved massive stars. In Appendix C, we describe how we calculate an approximate correction for this stellar mass loss to infer the birth stellar masses of star particles based on their present-day masses in TNG50 and FIREbox. We find that the birth stellar masses can be reasonably approximated from the present-day stellar mass as $M_{*,\text{born}} = M_*(z=0) \div (1 - R)$ assuming a population-averaged recycled fraction of $R = 0.25$ at present-day ($R = 0.30$ for FIREbox). This approximation adds no computational complexity and is correct to better than 10% precision for star particles older than 1 Gyr. A 10% uncertainty in the birth masses of the star particles makes no significant difference to our results. Once we know how much stellar mass was formed in each time bin, the cumulative stellar mass $M_*(t)$ can then be found by taking the cumulative sum from the first snapshot to the present-day. Under this definition, $M_*(t)$ is the total stellar mass formed prior to time t – we

have explicitly removed the effect of stellar mass loss due to the evolution of massive stars. This is the easiest way to compare to the observational SFHs, as the observational results give the SFR as a function of time – forming $M_*(t)$ from the observational results therefore only requires integrating the SFRs over time. The metallicity in the time bin $Z(t)$ is measured as the median metallicity of all star particles formed in the time bin.

Once $M_*(t)$ and $Z(t)$ have been measured, we form the MZH by combining the time series data from all the selected galaxies to form a single dataset consisting of total stellar masses and corresponding metallicities. We bin these data logarithmically in stellar mass and calculate the median and 68% confidence interval to form our final MZH measurements for TNG50, shown in Figure 10.

6.3. FIREbox

When it was first introduced, the FIRE galaxy evolution model (P. F. Hopkins et al. 2014) was unique in its approach to resolving the multiphase ISM in simulations of galaxy evolution. FIRE was particularly notable for its treatment of the cold, dense ISM – resolving temperatures ~ 10 K and densities $n_{\text{H}} \geq 100 \text{ cm}^{-3}$, FIRE formed stars in gas that was colder and denser than other contemporary models. Star formation in these cold, dense regions of the ISM could be highly efficient, and after a short period of forming stars, these regions would be destroyed due to significant stellar feedback. This cycling between the formation of dense, star-forming clouds and violent dissolution due to stellar feedback resulted in star formation that was more “bursty” (i.e., more time variable and spatially inhomogeneous) in FIRE simulations compared to other models like IllustrisTNG. Over the years, the FIRE model been updated with new and revised physics in FIRE-2 (P. F. Hopkins et al. 2018) and FIRE-3 (P. F. Hopkins et al. 2023). Until recently, the FIRE models had only been applied to zoom-in simulations due to computational constraints (see section 2.3 of A. Wetzel et al. 2023). With the completion of FIREbox (R. Feldmann et al. 2023), the first application of FIRE-2 to a cosmological volume, we now have a large statistical sample of galaxies across a range of environments that we can compare to other volume simulations like TNG50.

The FIREbox simulation (R. Feldmann et al. 2023) applies the FIRE-2 galaxy evolution model (P. F. Hopkins et al. 2018) to a cosmological volume of $(22.1 \text{ Mpc})^3$ with a baryonic particle mass of $6.26 \times 10^4 M_{\odot}$. The baryonic particle mass is of the same order of magnitude as TNG50 and the volume of FIREbox is roughly

8% that of TNG50. Given that we identified about 6000 galaxies matching our selection criteria in TNG50, we expected to find of order 500 galaxies matching our criteria in FIREbox given the differences in the volumes of the simulations. Applying the selection criteria described in §6.1 to FIREbox left us with 574 galaxies, well in line with our expectations. We select star particles associated with these galaxies at present-day from halo catalogs built with AHF (S. P. D. Gill et al. 2004; S. R. Knollmann & A. Knebe 2009).

Conveniently, the star particles in FIREbox have formation time and metallicity tags that are analogous to those we used when measuring the MZH in TNG50, enabling us to use the same procedure to measure the MZH in FIREbox. As our analysis procedure is essentially identical for both TNG50 and FIREbox, any differences in their MZHs should be attributable solely to their different galaxy evolution models.

6.4. *Galacticus*

We make predictions using the GALACTICUS semi-analytic model (A. J. Benson 2012) to compare against the hydrodynamic simulations described above. As a semi-analytic model, GALACTICUS requires merger trees to define the halos within which galaxies will form and evolve. We generate random merger trees using the built-in mechanisms based on the extended Press-Schechter formalism (W. H. Press & P. Schechter 1974; J. R. Bond et al. 1991; S. Cole et al. 2000; N. Cole et al. 2008; A. J. Benson et al. 2005; A. R. Zentner 2007; H. Parkinson et al. 2008; J. Zhang et al. 2008; F. Jiang & F. C. van den Bosch 2014; A. J. Benson 2017; E. O. Nadler et al. 2023). In this study, we track the evolution of 340 galaxy merger trees with present-day halo masses in the range 8×10^9 to $8 \times 10^{10} M_{\odot}$ and apply the selection criteria described in §6.1 to the galaxy population at present-day, leaving us with a sample of 78 galaxies that we use to derive the MZH.

The modeling of baryonic processes in GALACTICUS includes prescriptions for gas cooling, star formation, feedback, gas re-incorporation and metal enrichment, and many other processes important in galaxy evolution (see A. J. Benson 2012 for an overview of the physical processes modeled). Gas cooling is implemented based on S. D. M. White & C. S. Frenk (1991) to calculate the cooling radius, with the cooling time set by the halo’s dynamical time. Cooling rates are metallicity-dependent and computed using CLOUDY (v23.01, C. M. Gunasekera et al. 2023) assuming collisional ionization equilibrium. Star formation in the disk is modeled using a hydrostatic pressure-based formulation following L. Blitz & E. Rosolowsky (2006). The star

formation rate in the spheroid component of galaxies depends on the gas mass and the system’s dynamical time. In GALACTICUS, star formation drives gaseous outflows whose strength scales with the circular velocity of the halo and the rate of energy input due to the stellar populations (Equation A2 in N. Ahvazi et al. 2024). Gas expelled from galaxies by winds is retained in an outflow reservoir, from which it gradually returns to the hot halo on a timescale proportional to the halo’s dynamical time. Metal enrichment follows an instantaneous recycling approximation, assuming a fixed recycled fraction and metal yield, with metals fully mixed within all gas phases to track their transport between different reservoirs (for more details, see section 2.2 of A. Knebe et al. 2018 and Appendix A of N. Ahvazi et al. 2024).

As GALACTICUS can save output at any user-requested times, we output results on the same redshift grid as that of TNG50 for consistency. We can measure $M_*(t)$ for each galaxy straightforwardly from the stellar mass of the galaxy along the main progenitor branch of the merger tree. Once we have $M_*(t)$ and $Z(t)$ for each galaxy, we form the time-independent MZH the same way as we did for TNG50 and FIREbox.

7. RESULTS AND DISCUSSION

In Figure 10 we present the MZHs measured from TNG50, FIREbox, and GALACTICUS compared to our observational results for nearby isolated dwarfs. As discussed above, the selection of analogs from the theoretical sources was designed to select galaxies similar to WLM due to the limited resolution of TNG50 and FIREbox; Leo A, Leo P, and Aquarius are all an order of magnitude less massive than WLM, so we expect they may not be well-represented in this comparison, but we include them in Figure 10 for completeness. The stellar masses on the horizontal axis represent the cumulative stellar mass formed neglecting stellar mass loss due to massive star evolution. The field of view of our imaging covers the majority of Leo A, Leo P, and Aquarius, so we take the total stellar mass formed directly from our SFH measurements; no additional corrections are performed.

For WLM, the JWST/NIRCam data we use to measure the SFH are insufficient to cover the entire galaxy, so we must correct the normalization of our SFRs to reflect the true total stellar mass of WLM. We do this by first assuming the present-day stellar mass of WLM to be $4.3 \times 10^7 M_{\odot}$ (A. W. McConnachie 2012). The present-day stellar mass is typically converted into the cumulative stellar mass formed by assuming a recycling fraction of order 30–50% (F. Vincenzo et al. 2016; K. B. W. McQuinn et al. 2024a), with the specific value depending on the assumed IMF and SFH of the popu-

lation. However, calculating the recycling fraction requires making an assumption of the mass of stellar remnants (e.g., white dwarfs, neutron stars, and black holes) as a function of initial stellar mass and metallicity which adds uncertainty to the calculation of the present-day stellar mass (see, e.g., Equation 3 of F. Vincenzo et al. 2016). It is more straightforward to calculate the fraction of the total stellar mass formed that remains in stars using the IMF and stellar lifetimes directly. We use stellar lifetimes from the same PARSEC models used to measure our fiducial SFH to determine, for each stellar population of unique age i and metallicity j , the initial stellar mass of the most massive star that is still alive at present-day, $u_{i,j}$. Using our fiducial SFH, we then calculate the surviving stellar mass fraction as

$$f_{\text{surv}} = \frac{\sum_{i,j} c_{i,j} \int_l^{u_{i,j}} m \phi(m) dm}{\langle m \rangle \sum_{i,j} c_{i,j}} \quad (6)$$

where $c_{i,j}$ is the total stellar mass formed in the stellar population with age i and metallicity j , $\phi(m)$ is the IMF, l is the lower mass limit of the IMF, and $\langle m \rangle$ is the mean stellar mass of the IMF. Assuming $l = 0.08 M_{\odot}$, we find $f_{\text{surv}} = 0.47$. We therefore estimate the total stellar mass formed in WLM to be $\frac{4.3}{0.47} \times 10^7 \approx 9.1 \times 10^7 M_{\odot}$. We use this value to renormalize our SFRs when plotting the MZH for WLM in Figure 10.

7.1. The Mass-Metallicity History of WLM

We find that the best-fit power law slope for WLM is $\alpha \approx 1$ (see Equation 4). GALACTICUS shows a nearly constant power law slope of $\alpha \approx 0.4$ across the entire stellar mass range, while the MZH in TNG50 shows scaling more similar to a broken power law. At early times, when the stellar mass of the simulated galaxies was $M_* \leq 10^7 M_{\odot}$, the power law scaling in TNG50 is $\alpha \approx 1.0$ and becomes $\alpha \approx 0.2$ above this mass. As such, the low-mass slope of the TNG50 MZH actually agrees with the slope we find for WLM, but the metallicity normalization is much higher – at $M_* = 10^7 M_{\odot}$, the TNG50 prediction is about 0.9 dex higher than what we measure for WLM. In contrast to TNG50 and GALACTICUS, FIREbox does not exhibit simple power law, or even broken power law, scaling. Across nearly the entire range of the predictions from $10^6 \leq M_* \leq 10^9$, the slope of the MZH in FIREbox is larger than in GALACTICUS and TNG50. While FIREbox agrees fairly well with the other simulations at higher masses, it predicts much lower metallicities at low stellar masses compared to the other simulations ($[M/H] \leq -1.5$ dex for $M_* \leq 10^7 M_{\odot}$). This ends up putting the FIREbox prediction in quite good agreement with our result for WLM.

Comparing the theoretical results, they are all roughly consistent at the high-mass end ($M_* \geq 10^8 M_{\odot}$), which we expect as they all reasonably reproduce the traditional MZR at these masses (e.g., P. Torrey et al. 2019; N. Ahvazi et al. 2024; L. Bassini et al. 2024; A. M. Garcia et al. 2024b, 2025b). As a result, the MZH cannot meaningfully distinguish between the models in the stellar mass range $10^8 \leq M_* \leq 10^9 M_{\odot}$. However, at lower masses the models predict significantly different metallicities. The TNG50 MZH predicts the highest metallicities between $10^7 \leq M_* \leq 10^8 M_{\odot}$, while FIREbox predicts the lowest. At $M_* = 10^7 M_{\odot}$, TNG50 predicts $[M/H] \approx -0.6$ dex for our sample of WLM analogs, while GALACTICUS predicts $[M/H] \approx -1.1$ dex and FIREbox predicts $[M/H] \approx -1.3$ dex. At this stellar mass, the observational result for WLM shows $[M/H] \approx -1.5$ dex, consistent with the FIREbox result given the uncertainties. Observationally, we are able to measure WLM’s MZH starting from when it had formed $\sim 2 \times 10^6 M_{\odot}$ of stars up to the present-day when it has formed a total of $\sim 9 \times 10^7 M_{\odot}$ of stars – across this full range, the results agree best with the predictions of FIREbox.

A possible explanation for the difference between the predictions of TNG50 and FIREbox are the supernova metal yields. However, the differences between the metal yields in TNG50 and FIREbox are too minor to explain the ~ 0.7 dex difference in their predicted metallicities for $M_* \leq 10^7 M_{\odot}$ (A. Pillepich et al. 2018; P. F. Hopkins et al. 2018). For our purposes we will discuss the total metal yield as none of our analysis depends on specific elemental abundances. For SN-Ia, where no compact remnant is produced, both simulations eject a Chandrasekhar mass ($\sim 1.4 M_{\odot}$) of metals into the ISM. For core-collapse supernova (CCSN), FIRE-2 assumes the yield tables of K. Nomoto et al. (2006) but renormalizes the total ejecta mass to match a set of STARBURST99 (C. Leitherer et al. 1999) models. FIRE-2 assumes the P. Kroupa (2001) IMF, resulting in an IMF-averaged metal ejecta mass of about $2 M_{\odot}$ per CCSN. The only element with a metallicity-dependent yield in FIRE-2 is N such that the average metal ejecta mass per CCSN is nearly constant as a function of initial stellar metallicity. In comparison, the IllustrisTNG model uses the C. Kobayashi et al. (2006) yield table and extends the mass coverage with the L. Portinari et al. (1998) yield table (A. Pillepich et al. 2018). The joint table is renormalized so that the yield ratios between species match that of the C. Kobayashi et al. (2006) yield table and the total ejected metal mass matches the L. Portinari et al. (1998) yield table. In the IllustrisTNG model, the metallicity dependence of the CCSN yields follows that of the yield tables; no other alterations are made.

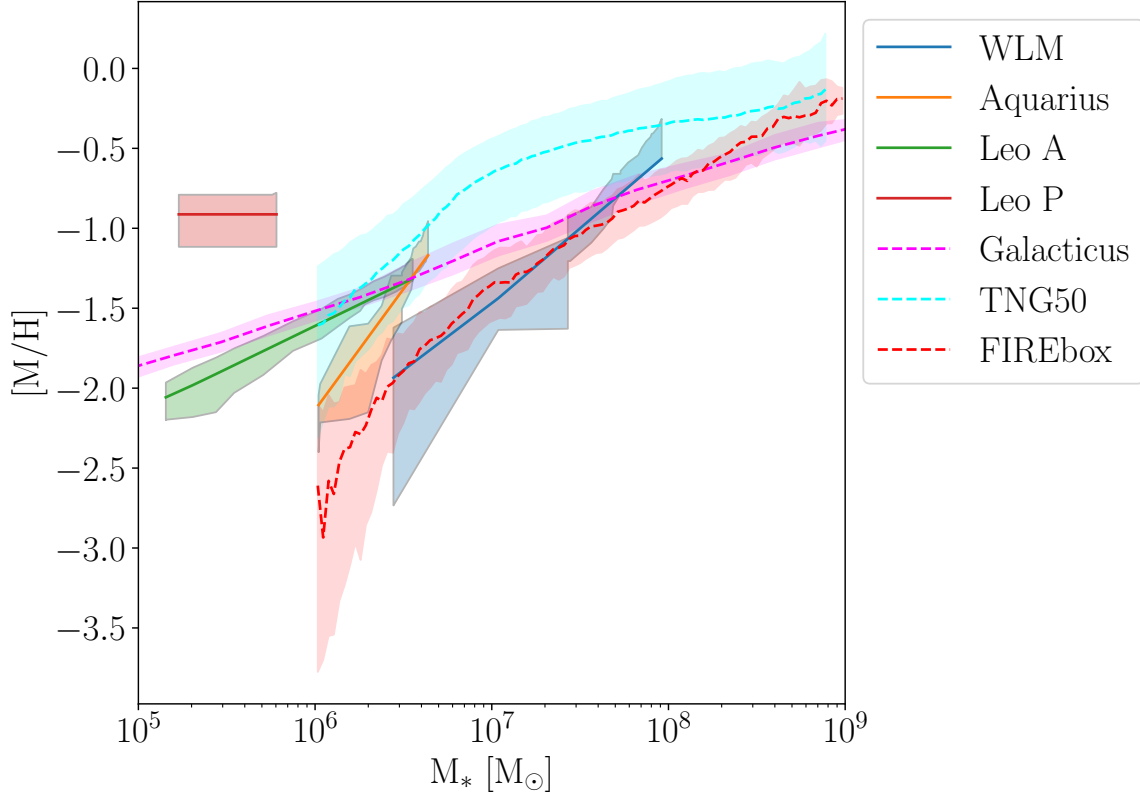


Figure 10. MZHs for WLM-analog galaxies measured from TNG50, FIREbox, and GALACTICUS (dashed lines) compared to our observational results for nearby isolated dwarfs (solid lines). For the simulation measurements, the shaded regions represent the 68% confidence interval on the median metallicity in each stellar mass bin. The solid lines show our fiducial observational measurements under our new MZH model, with shaded regions representing the systematic uncertainty region (measured as discussed in §3).

Using the [G. Chabrier \(2003\)](#) IMF assumed by the IllustrisTNG model, we estimate an IMF-averaged metal ejecta mass of about $2.14 M_\odot$ of metals per CCSN at $[M/H] = -1.5$ dex. This is only $\sim 7\%$ higher than the IMF-averaged metal ejecta mass in FIRE-2 and is insufficient to explain the ~ 0.7 dex difference in the MZH predictions between TNG50 and FIREbox at $M_* = 10^7 M_\odot$. The occurrence rates of SN-Ia and CCSN (in terms of the number of supernovae per solar mass of star formation) are also comparable between FIRE-2 and TNG, such that differences between their MZHs cannot be due to differences in the supernova rates either.

We hypothesize that differences between the MZHs of TNG50 and FIREbox are likely attributable to their different implementations of stellar feedback. While both stellar feedback models drive galaxy-scale outflows at dwarf masses ($M_* \leq 10^7 M_\odot$; [A. L. Muratov et al. 2015](#); [D. Nelson et al. 2019](#); [V. Pandya et al. 2021](#)) the mass-loading factors ($\eta = \frac{M_{\text{outflow}}}{M_{\text{SFR}}}$) in FIRE-2 can be an order of magnitude larger than those in TNG50 at dwarf scales ([A. L. Muratov et al. 2015](#); [D. Nelson et al. 2019](#); [V. Pandya et al. 2021](#)). While these outflows can push a sig-

nificant amount of gas out of the ISM, such outflows are typically more metal-rich than the star-forming ISM as they retain a significant fraction of the metals ejected in the supernova events ([J. Chisholm et al. 2018](#)). The degree to which the outflows are metal-enhanced depends on simulation details such as the adopted metal diffusion model (e.g., [I. Escala et al. 2018](#); [Z. Hafen et al. 2019](#); [A. M. Garcia et al. 2025a](#); [U. P. Steinwandel et al. 2025](#)), but it is generally accepted that outflows driven by supernovae push a significant fraction of the metals formed in dwarf galaxies out of the ISM. These theoretical results are reinforced by observational studies of the traditional MZR at dwarf scales that show that dwarf galaxy metallicities are lower than would be expected if they retained all of the metals they create, necessitating significant metal-loaded outflows to reproduce the observed MZR (e.g., [E. N. Kirby et al. 2011b, 2013](#); [E. Kado-Fong et al. 2024](#)).

If the differences in the MZHs of TNG50 and FIREbox are indeed due to differences in their supernova-driven outflows, this should manifest differences in the CGM properties they predict at dwarf scales as well. Ob-

servationally, the CGM metallicity can be probed via metal-line absorption studies. In [F. Li et al. \(2021\)](#), CGM metal-line absorption predictions for galaxies with $8.1 \leq \log(M_*) \leq 10.4$ simulated with FIRE-2 were compared against observations, with results indicating reasonably good agreement across several different metal ions probing different phases of the CGM (e.g., C IV and O VI). These galaxies are more massive than WLM, so extending this work to dwarf galaxies of lower mass in the future would provide a better comparison. Interestingly, [Z. Hafen et al. \(2019\)](#) find that low-mass FIRE-2 galaxies host significantly more metals in their CGM than in their ISM, highlighting the importance of the CGM as a metal reservoir (see their Figure 3). Recycling of metals from the CGM back into the ISM can then be a critical mechanism by which the ISM metallicity is regulated – all accreted baryons, including pristine gas from the intergalactic medium, must pass through the CGM to reach the ISM, providing an opportunity for the metal-enriched CGM to mix with the accreting material (e.g., [P.-C. Tung & K.-J. Chen 2025](#)). In a study examining the time evolution of the MZR for galaxies with $8 \leq \log(M_*) \leq 11$ in FIREbox, [L. Bassini et al. \(2024\)](#) find that the time dependence of the MZR is due to the average metallicity of accreted gas increasing over time as the metal-enriched CGM mixes with gas inflows from other sources.

In contrast, the analysis of [P. Torrey et al. \(2019\)](#) ascribes the cause of the redshift evolution of the MZR to a different mechanism in the IllustrisTNG model. Studying galaxies with $9 \leq \log(M_*) \leq 10.5$, they find that redshift evolution in the gas fraction of galaxies is the primary driver of the redshift evolution of the MZR. As the metallicity of the ISM is a relative quantity (the relative abundance of metals to hydrogen), increasing the gas mass in the ISM at fixed ISM metal mass decreases the overall metallicity of the ISM (and vice versa). [L. Bassini et al. \(2024\)](#) do not find the same mechanism to be effective in the FIRE-2 galaxy evolution model. This is interesting as both models have been shown to agree well with measurements of the MZR for $M_* \geq 10^9 M_\odot$ ([P. Torrey et al. 2019](#); [L. Bassini et al. 2024](#); [S. Jain et al. 2025](#)). However, these analyses looked at galaxies at least an order of magnitude more massive than WLM, so these results cannot be directly compared to our measurements. Additionally, most of the work done looking at the CGM in the IllustrisTNG model has focused on higher mass galaxies like the MW (e.g., [D. Nelson et al. 2020](#); [R. Ramesh et al. 2023a,b](#)), so it is unclear how significant a role metal recycling from the CGM back into the ISM plays in regulating the ISM metallicities of dwarf galaxies in the IllustrisTNG model.

Further work examining the early-time CGM and ISM properties of dwarf galaxies in the IllustrisTNG model is needed to determine if the higher metallicities it predicts at $M_* \leq 10^7 M_\odot$ in our MZHs can be explained by the impact of supernova-driven outflows and metal recycling from the CGM.

The stellar feedback model in GALACTICUS is also capable of driving significant outflows in dwarf galaxies. These outflows are captured in a CGM-like reservoir from which gas can re-accrete onto the galaxy. As shown by [N. Ahvazi et al. \(2024\)](#), increasing the metallicity of accreting gas over time is critical to match the metallicities of MW dwarf satellites with $M_* \leq 10^5 M_\odot$; this mechanism is similar to that found to be responsible for the time dependence of the MZR in FIRE-2 by [L. Bassini et al. \(2024\)](#). GALACTICUS uses a model for supernova-driven outflows that scales as a power-law with the ratio of outflow velocity (with fiducial value $V_{\text{out}} = 200 \text{ km/s}$) to the galaxy’s circular velocity ($\dot{M}_{\text{out}} \propto \left(\frac{V_{\text{out}}}{V_{\text{circ}}}\right)^\alpha$); we believe this is the primary reason GALACTICUS predicts a MZH that is nearly a power law in Figure 10 with $\langle [M/H](M_*) \rangle \approx -1.5 + 0.38 (\log(M_*) - 6)$. In contrast, the hydrodynamic simulations both show deviations from a constant power law starting at $M_* \approx 10^7 M_\odot$. In hydrodynamic simulations, supernova ejecta must expand into an ISM which provides mechanical resistance to the expanding shock; this effect is not modeled in GALACTICUS and could explain why the hydrodynamic simulations do not exhibit simple power-law scaling in the MZH.

At $M_* = 10^7 M_\odot$, the GALACTICUS MZH lies between the predictions of TNG50 and FIREbox, but the hydrodynamic simulations show a steepening of the MZH below this mass while GALACTICUS does not. As a result, GALACTICUS predicts the highest metallicity of the three models at $M_* = 10^6 M_\odot$, which is the lowest mass for which we measure the MZHs in the hydrodynamic simulations due to resolution concerns. The sample variance in the MZH in GALACTICUS is also lower than in the hydrodynamic simulations. The standard deviation in $[M/H]$ at fixed M_* is typically $\sigma \lesssim 0.1$ dex, indicating that the metallicity of the ISM correlates very strongly with the total stellar mass formed and secondary variables like the SFH and accretion history impact the MZH less in GALACTICUS than in the hydrodynamic simulations. This is, again, likely a result of the simple power law scaling between the supernova-driven outflow rate and the galactic circular velocity in GALACTICUS introducing little variance into the MZH.

7.2. Aquarius, Leo A, and Leo P

Our simulation results are limited to galaxies that are of similar mass to WLM at present-day due to resolution concerns in TNG50 and FIREbox. Therefore, we would not necessarily expect these simulation results to agree well with the results for Aquarius, Leo A, and Leo P, which have formed an order of magnitude less stellar mass over their histories compared to WLM. Additional work making similar measurements with higher resolution simulations is warranted to better interpret these measurements, but we offer some general comments here.

We note first that comparing our measured MZHs for WLM, Leo A, and Aquarius indicates that the MZH is not universal. If the MZH was universal, we would expect that the MZHs for these galaxies would form a continuous power law in Figure 10, but they do not. In the limited stellar mass range where they overlap ($2\text{--}4 \times 10^6 M_\odot$) our measurement for WLM shows a significantly lower metallicity ($[M/H] \sim -2$ dex) compared to Aquarius and Leo A ($[M/H] \gtrsim -1.5$ dex).

The most likely explanation for this is that the MZH has an additional redshift dependence – WLM formed a total stellar mass of $2 \times 10^6 M_\odot$ over 12 Gyr ago, while Aquarius and Leo A reached this stellar mass only a few Gyr ago. Hydrodynamic simulations predict that the MZR should have such a redshift dependence, although the quantitative scaling of the redshift dependence and the underlying causal mechanism that creates the redshift dependence differs between galaxy evolution models (e.g., P. Torrey et al. 2019; L. Bassini et al. 2024; A. M. Garcia et al. 2025b, see also the discussion in §7.1). Observations also indicate the existence of a redshift-dependent MZR, though these studies target galaxies of greater masses than we consider here (M. Li et al. 2023; K. Nakajima et al. 2023; M. Curti et al. 2024; S. Jain et al. 2025).

Such a redshift dependence could be added to our MZH model by modifying Equation 4. In studies of the MZR, redshift dependence is often modeled by making the power law slope α and/or the normalization $[M/H]_0$ functions of redshift. This could be added to our model without much difficulty, but constraining the redshift dependence requires forming a statistical sample of measurements for galaxies that probe $\langle [M/H] \rangle (M_*)$ for the same range of M_* at different redshifts to constrain $\alpha(z)$ and $[M/H]_0(z)$. Our present sample is too small for such an analysis to be robust, but future extensions of this work measuring the MZHs of additional galaxies in the Local Universe will enable us to constrain the redshift dependence of the MZH.

Even in comparing just Leo A and Aquarius we can see indications of a time dependence in the MZH. While both galaxies have comparable stellar mass and metallicity at present-day, our measurements show that they have different MZHs. We fit power law slopes of $\alpha \approx 1.5$ for Aquarius and $\alpha \approx 0.5$ for Leo A; even considering the range of α values fit under different stellar tracks and BCs, the two galaxies show inconsistent power law slopes. The most conspicuous difference between these galaxies that could explain these results are their SFHs (i.e., *when* they formed their stars). Relative to other Local Group dwarfs, Leo A formed its stellar mass quite late – our measurement indicates that Leo A formed 10% of its total stellar mass only ~ 7 Gyr ago ($\tau_{10} \approx 7$; see Table 2), while Aquarius has $\tau_{10} > 13$ Gyr. Even their τ_{50} values are significantly different, as $\tau_{50} \approx 3.6$ Gyr for Leo A and $\tau_{50} \approx 6.7$ Gyr for Aquarius. In the presence of a time-dependent MZH, it would be expected that these galaxies would show different metallicities at fixed total stellar mass formed as the *time* at which they reached that stellar mass would be different.

As discussed in §5.4, the metallicity we fit for Leo P is ~ 0.6 dex higher than is implied by the oxygen abundance of its single HII region E. D. Skillman et al. (2013) and no other metallicity constraints are available to constrain the metallicity of Leo P’s stellar population. If Leo P is currently forming stars at $[M/H] \approx -1.5$ dex as implied by the HII region oxygen abundance, then it would be roughly consistent with the GALACTICUS prediction. As Leo P is nearly 2 dex lower in stellar mass compared to the mean stellar mass of the simulated galaxies, we refrain from commenting on it further – additional work with higher resolution simulations, probing an appropriate range of stellar mass, is needed to better interpret the result for Leo P.

8. CONCLUSION

We have developed a new framework that directly links the chemical enrichment history of galaxies to their resolved SFHs by modeling metallicity evolution as a function of cumulative stellar mass formed. We apply this methodology to four isolated, gas-rich Local Group dwarf galaxies—WLM, Aquarius, Leo A, and Leo P—and present new measurements for their global SFHs and chemical evolution history. We validate our chemical evolution measurements against independent measurements of the ages and metallicities of individual red giant stars in WLM, Leo A, and Aquarius, finding good agreement with our results. We measure systematic uncertainties by repeating our measurements using multiple stellar evolution and bolometric correction

libraries, demonstrating the effect these modeling assumptions have on our results.

We examine the chemical enrichment history of WLM-analog galaxies in the TNG50 and FIREbox cosmological hydrodynamic simulations and the GALACTICUS semi-analytic model in order to examine how our observations can help to constrain galaxy evolution physics. We find that all three models predict similar metallicities at higher masses ($M_* \geq 10^8 M_\odot$) but deviate significantly at lower masses, highlighting the importance of studying low-mass dwarf galaxies to constrain galaxy evolution physics. The chemical evolution history we measure for WLM is most similar to the predictions of FIREbox, with TNG50 and GALACTICUS predicting higher metallicities at early times. We ascribe the differences between the model predictions to their stellar feedback predictions that regulate the metallicity of the ISM by driving metal-enriched outflows out of the ISM. We suggest that studying the outflow properties of dwarf galaxies at early times may further reveal the mechanisms by which the chemical enrichment of dwarf galaxies is regulated.

Our results underscore the power of combining resolved SFHs with physically motivated chemical evolution models to constrain the physics of galaxy formation, especially in the low-mass regime. They also emphasize the need for further observational and theoretical work to better understand stellar feedback, metal retention, and the cycling of metals between the ISM and the CGM. This framework opens new avenues for testing galaxy evolution models using observations of nearby galaxies.

ACKNOWLEDGMENTS

We thank Leo Girardi for helpful discussions on stellar tracks and bolometric corrections. We thank James Johnson for helpful discussions on galactic chemical evolution models. The authors acknowledge [Research Com-](#)

puting at [The University of Virginia](#) for providing computational resources and technical support that have contributed to the results reported within this publication. We acknowledge useful discussions during Galaxy Evolution and Cosmology (GECO) lunches at the University of Virginia.

AUTHOR CONTRIBUTIONS

CTG is the primary author responsible for planning, executing, and presenting the work. AMG performed the selection of WLM analogs from the TNG50 simulation. NA ran the GALACTICUS simulations presented in this work and assisted with analyzing the results. NK helped plan, organize, and direct the work. KBWM provided the photometric data products for Aquarius, Leo A, and Leo P and the MATCH SFH measurements from [K. B. W. McQuinn et al. \(2024a\)](#) to facilitate comparison to the new measurements. RF provided access to the FIREbox simulations and assisted CTG in working with the data products. RC assisted with editing of the manuscript.

Facilities: JWST (NIRCAM), HST(ACS)

Software: This research made use of the following software packages:

1. [StarFormationHistories.jl](#) (C. Garling 2025)
2. [InitialMassFunctions.jl](#)
3. [BolometricCorrections.jl](#)
4. [StellarTracks.jl](#)
5. The Julia programming language (J. Bezanson et al. 2017)
6. [Matplotlib](#) (J. D. Hunter 2007)
7. [Distributions.jl](#) (M. Besançon et al. 2021; D. Lin et al. 2025)
8. [DynamicHMC.jl](#) (T. K. Papp et al. 2023)
9. [Optim.jl](#) (P. K. Mogensen & A. N. Riseth 2018)
10. [LBFGS.jl](#) (C. Zhu et al. 1997).

APPENDIX

A. THE AGE DISTRIBUTION ON THE RED GIANT BRANCH OF LEO A

Here we examine the age distribution of stars on the upper RGB of Leo A in order to understand the difficulty inherent in measuring its metallicity evolution. Using the methods described in appendix A of [C. T. Garling et al. \(2025\)](#), we use PARSEC stellar tracks and YBC BCs to sample a random realization of Leo A's CMD assuming our best-fit SFH. Other relevant parameters (e.g., distance, reddening, IMF) are the same as were used in the SFH fit. We add photometric error and account for incompleteness using the same methods as are used when measuring the SFH. In the left panel of Figure 11 we show the mock CMD; stars with spectroscopic metallicities from [E. N. Kirby et al. \(2017\)](#) for which we also have HST/ACS photometry are shown overplotted as red star symbols. The red boxed region encloses the sample of [E. N. Kirby et al. \(2017\)](#). We plot the age distribution of stars that fall within this region in

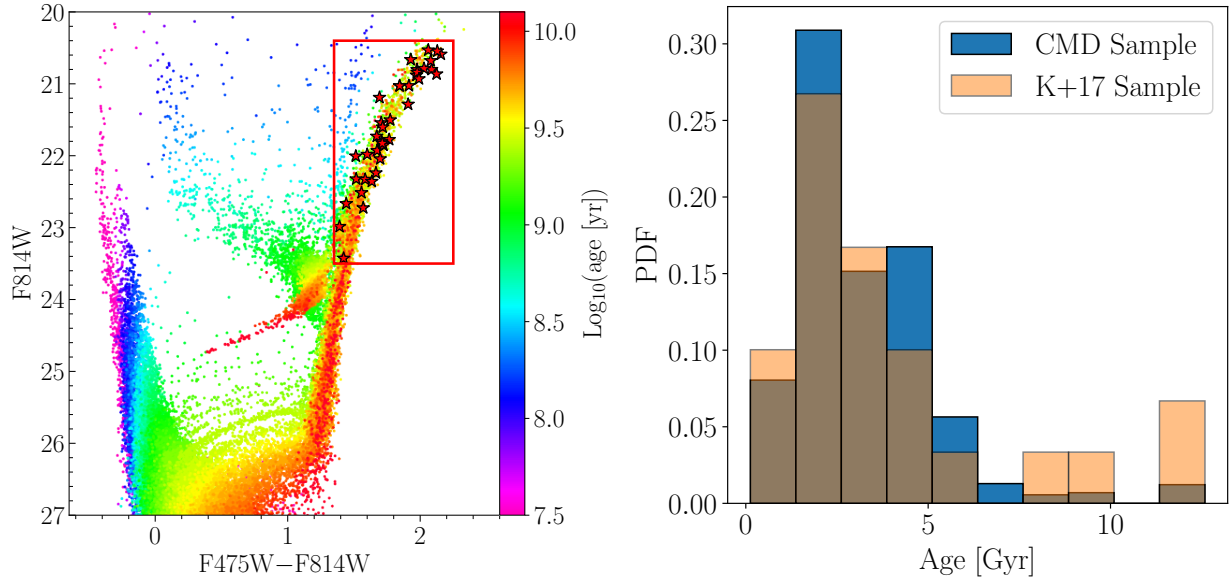


Figure 11. *Left:* A mock CMD simulated assuming the best-fit SFH of Leo A. Stars are colored according to the logarithms of their ages. Stars with spectroscopic metallicities from E. N. Kirby et al. (2017) are overplotted as red stars. The red box contains the sample of E. N. Kirby et al. (2017). *Right:* The distribution of ages for all randomly sampled stars in the red box region from the left panel (blue) compared to the age distribution of observed red giant stars with spectroscopic metallicities from E. N. Kirby et al. (2017) (orange) illustrating that about 80% of the stars in this region are expected to be younger than 5 Gyr.

the right panel. This distribution demonstrates a clear and significant skew to young ages (< 5 Gyr), with only 19% of stars in the region being older than 5 Gyr. This is in reasonable agreement with the observations, as 14% of the stars for which we measure ages are older than 5 Gyr. We hypothesize that the relative paucity of bright, old stars in Leo A has made it difficult for previous work to accurately measure the historical metallicity evolution in Leo A (e.g., A. A. Cole et al. 2007), as younger stars with higher metallicities are far more numerous on the upper RGB.

B. THE STAR FORMATION HISTORY OF LEO P WITH FIXED METALLICITY

Here we present the results of an experiment fitting the SFH of Leo P assuming a present-day metallicity of $[M/H] = -1.5$ dex, consistent with the oxygen abundance measured from the single HII region in Leo P (E. D. Skillman et al. 2013). The MZH slope parameter (α in Equation 4) is left free to vary, but is found to be 0 for all solutions. We performed other experiments with different fixed metallicities, but these results are representative of the general trends we observed. Our best-fit model Hess diagram is compared to the data in Figure 12 and the resulting SFH is shown in Figure 13.

Assuming this lower metallicity results in a better fit to the upper RGB than in our fiducial fit (Figure 8), but the lower RGB and upper main sequence show significant residuals that are not present in our fiducial fit. As these areas of the CMD contain many more stars than the upper RGB, the overall fit quality is worse than in our fiducial fit. The resulting SFH shows a very large initial burst of star formation in which Leo P forms roughly 40% of its total stellar mass. Generally this solution indicates that Leo P formed more stellar mass earlier than in our fiducial fit. Future work constraining the metallicity of Leo P’s stellar population is needed to improve the modeling of this low mass dwarf galaxy.

C. INFERRING BIRTH MASSES OF STAR PARTICLES

In both the IllustrisTNG and FIRE-2 galaxy evolution models, star particles are born with irregular masses as the initial mass of each star particle is inherited from its parent gas resolution element (the gas resolution elements are cells in IllustrisTNG simulations and particles in FIRE-2). The masses of the gas resolution elements change over time in order to conserve mass in the presence of stellar winds, supernovae, and other processes that transfer mass between gas resolution elements. In both models, star particles are massive enough that they are modeled as SSPs and the evolution of their properties is tracked accordingly. In particular, star particle masses decrease over time following

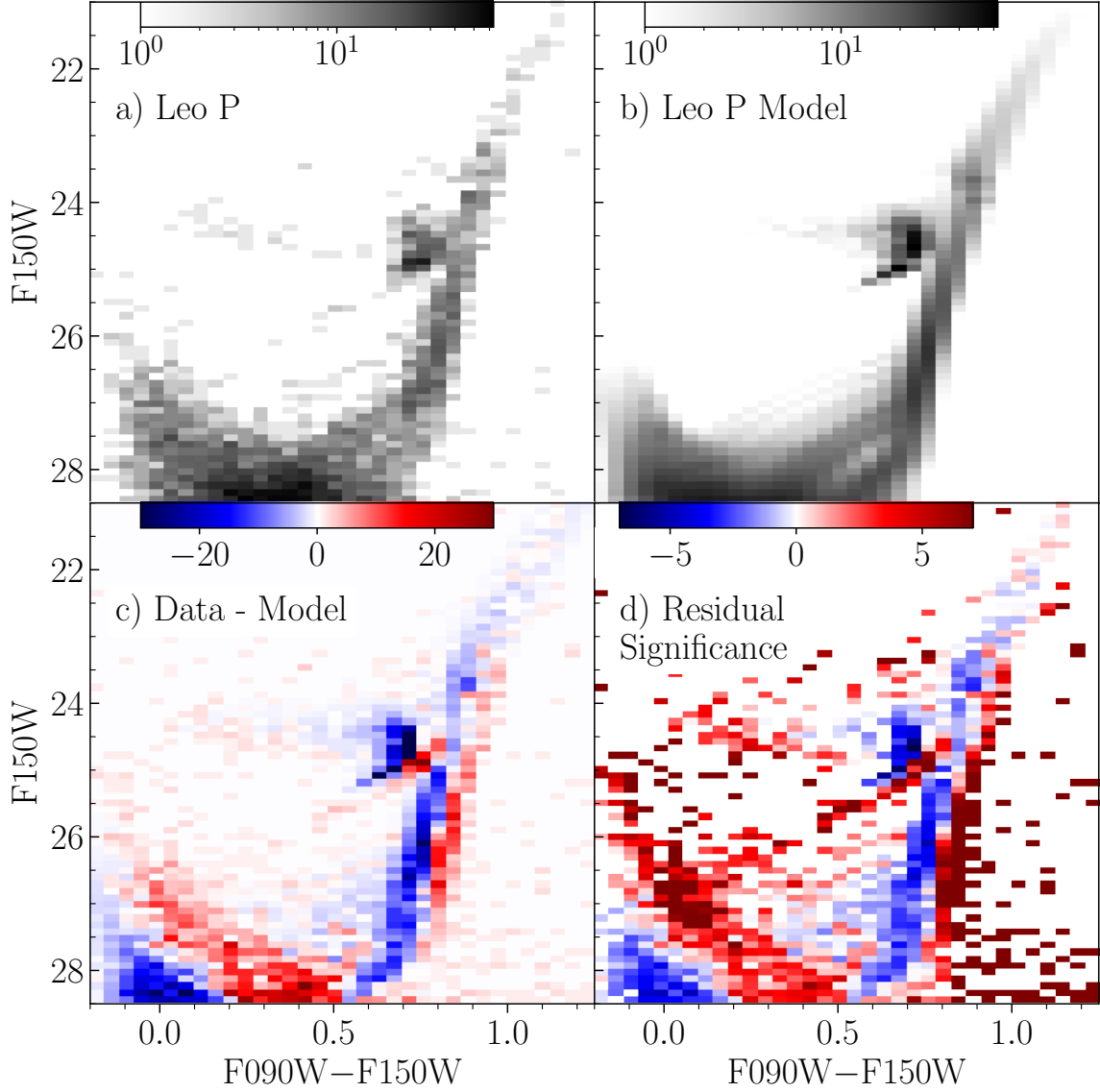


Figure 12. Comparison of the JWST/NIRCam Hess diagram of Leo P with our best-fit model assuming $[M/H] = -1.5$ dex at present-day. The panels follow the same layout as in Figure 2. While the upper RGB in the model is a better match to the data than in our fiducial fit (Figure 8), the lower RGB and upper main sequence show significant residuals and the fit quality is worse overall.

models of stellar mass loss due to massive star evolution. Stellar mass lost due to massive star winds and supernovae is returned to the ISM, and the so the fraction of stellar mass lost is also known as the recycled fraction (R). The recycled fraction as a function of the SSP age can be calculated given models for stellar lifetimes, an assumed IMF, and appropriate yield tables for each relevant type of massive star. The recycled fraction will be highest for the oldest star particles which have $R \approx 0.3$ in both IllustrisTNG and FIRE-2 (see, e.g., Figure 1 of [A. Pillepich et al. 2018](#) and Figure 4 of [P. F. Hopkins et al. 2023](#)).

Conveniently, appendix A of [P. F. Hopkins et al. \(2018\)](#) gives IMF-averaged yields and fitting functions for the occurrence rates of SN-Ia and CCSN in FIRE-2, as well as stellar mass-loss rates from winds driven by massive O and B-type stars as well as evolved AGB stars. We use this information to calculate the recycled fraction as a function of SSP age shown in Figure 14 (blue). We show the fraction of stellar mass lost due to supernovae (dotted), stars (dashed), and the total recycled fraction (solid). This simple model based on fitting functions reproduces Figure 4 of

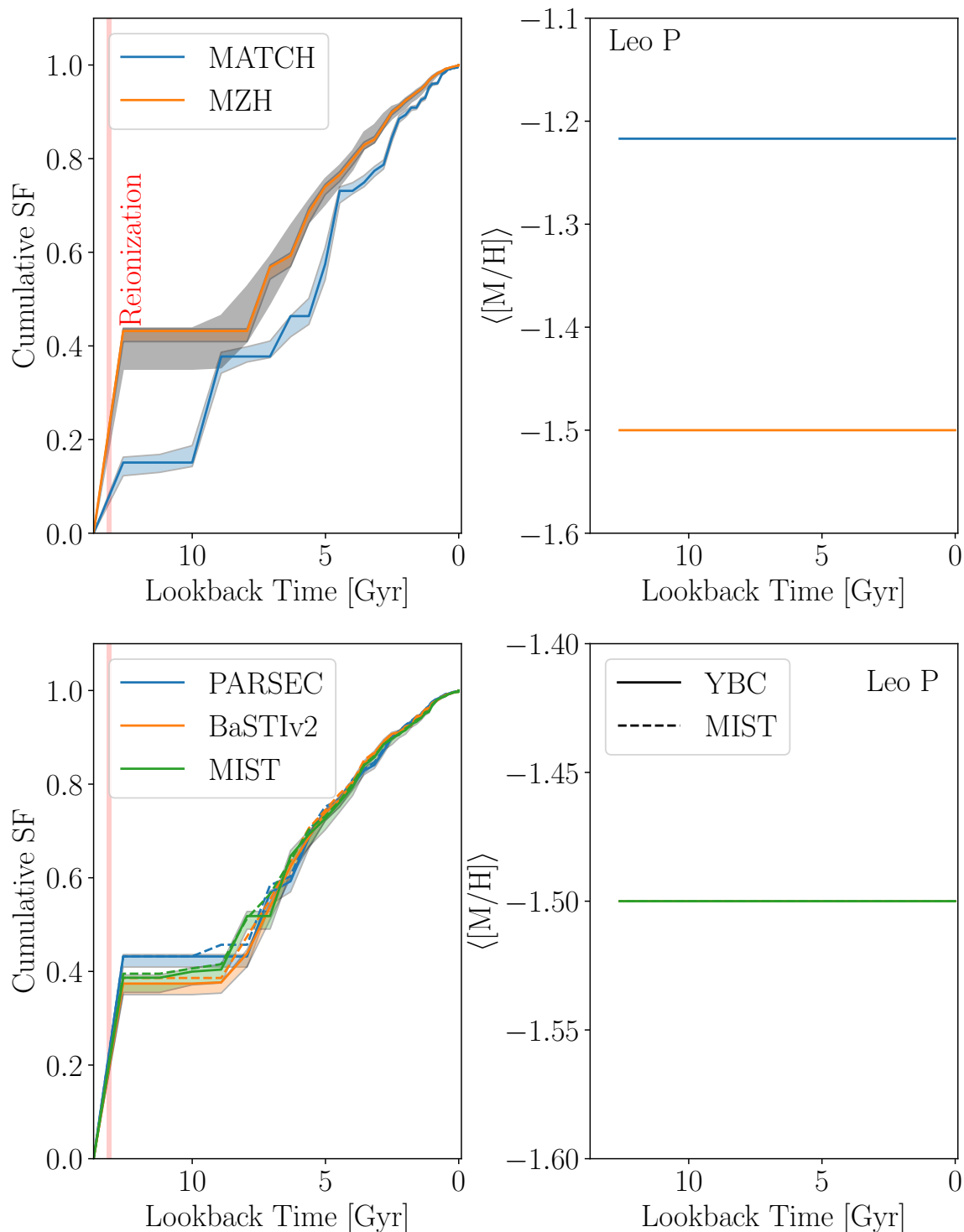


Figure 13. The results of our resolved SFH and metallicity evolution fit for Leo P assuming $[M/H] = -1.5$ dex at present-day. The panels follow the same format as Figure 3. In the top row the result of K. B. W. McQuinn et al. (2024a) (blue line), who used the MATCH code on the same data, is shown for comparison. Assuming a lower metallicity than our fiducial fit results in a very large initial burst of star formation in which Leo P forms roughly 40% of its total stellar mass. Overall, Leo P formed more stellar mass earlier in this model than in our fiducial fit.

P. F. Hopkins et al. (2023) well, which compares the stellar mass fraction lost as a function of SSP age for the FIRE-2 and FIRE-3 galaxy evolution models.

No similar fitting functions are available for IllustrisTNG, so we calculate the recycled fraction from first principles. The assumed stellar evolution physics for IllustrisTNG is discussed in section 2.3.3 of A. Pillepich et al. (2018) and is summarized in their Table 2 (see also section 2.1 of P. Torrey et al. 2019). Following the above references, we adopt the IMF from G. Chabrier (2003), total CCSN ejecta masses and stellar lifetimes from L. Portinari et al. (1998), SN-Ia rates from D. Maoz et al. (2012), and total AGB wind masses from A. I. Karakas (2010). We note that the abundance ratios for CCSN in IllustrisTNG follow C. Kobayashi et al. (2006), but the total ejecta masses are normalized to match L. Portinari et al. (1998), which is the relevant quantity for computing the fraction of stellar mass lost from an SSP as a function of age. Additionally, IllustrisTNG integrates yield tables from other sources for AGB stars with initial masses between 6–7 M_{\odot} but we omit these for simplicity, using only the A. I. Karakas (2010) yields for AGB stars with initial masses 1–6 M_{\odot} which are sufficient to capture the majority of the mass loss due to AGB star winds. Using these as inputs, we calculate the recycled fraction as a function of SSP age under the IllustrisTNG model, shown in Figure 14 (orange). The fractions of stellar mass lost after 10 Gyr ($\sim 21\%$ due to AGB stars and $\sim 7\%$ due to supernovae, for $\sim 28\%$ total) agree well with the values shown in Figure 1 of A. Pillepich et al. (2018).

Given these full models, it is possible to infer the birth mass of each star particle based on its age and present-day mass by interpolating the recycled fraction as a function of SSP age. However, this would be somewhat excessive as $> 99\%$ of the star particles are older than 40 Myr at present-day, meaning that there will be no further recycling from CCSN. Additionally, the total mass recycling from SN-Ia is $< 1\%$ over a Hubble time (see also section 2.2 of M. C. Segers et al. 2016), making AGB star winds the only significant contributor to the evolution of the recycled fraction for SSPs older than 40 Myr. Additionally, the fraction of mass lost due to AGB star winds only changes by 10–15% for SSP ages older than 1 Gyr in both models, indicating that the recycled fraction changes slowly over most of cosmic time. As a result, the birth stellar masses of the star particles in our WLM-analog galaxies can be well approximated by simply assuming a population-averaged recycled fraction (e.g., R evaluated at $\tau_{50} = 4.68$ Gyr; see Table 2) and computing the birth stellar mass based on the present-day stellar mass as $M_{*}(z=0) \div (1-R)$. We find the appropriate average recycling fractions to be $R = 0.25$ for the IllustrisTNG model and $R = 0.3$ for FIRE-2. Neglecting the age dependence results in a birth mass uncertainty of $\sim 10\%$, which does not meaningfully impact our MZH results shown in Figure 10 as our measurements span several orders of magnitude in stellar mass.

As noted in the main text, GALACTICUS uses the instantaneous recycling approximation for returning stellar material back into the ISM with a fixed recycled fraction ($R = 0.46$; section 2.2 of A. Knebe et al. 2018) so that inferring the amount of stellar mass born as a function of time is trivial.

REFERENCES

- Agertz, O., Pontzen, A., Read, J. I., et al. 2020, MNRAS, 491, 1656, doi: [10.1093/mnras/stz3053](https://doi.org/10.1093/mnras/stz3053)
- Ahvazi, N., Benson, A., Sales, L. V., et al. 2024, MNRAS, 529, 3387, doi: [10.1093/mnras/stae761](https://doi.org/10.1093/mnras/stae761)
- Albers, S. M., Weisz, D. R., Cole, A. A., et al. 2019, MNRAS, 490, 5538, doi: [10.1093/mnras/stz2903](https://doi.org/10.1093/mnras/stz2903)
- Allard, F., Homeier, D., & Freytag, B. 2012, Philosophical Transactions of the Royal Society of London Series A, 370, 2765, doi: [10.1098/rsta.2011.0269](https://doi.org/10.1098/rsta.2011.0269)
- Andrews, B. H., & Martini, P. 2013, ApJ, 765, 140, doi: [10.1088/0004-637X/765/2/140](https://doi.org/10.1088/0004-637X/765/2/140)
- Anglés-Alcázar, D., Faucher-Giguère, C.-A., Kereš, D., et al. 2017, MNRAS, 470, 4698, doi: [10.1093/mnras/stx1517](https://doi.org/10.1093/mnras/stx1517)
- Aparicio, A., & Gallart, C. 2004, AJ, 128, 1465, doi: [10.1086/382836](https://doi.org/10.1086/382836)
- Bassini, L., Feldmann, R., Gensior, J., et al. 2024, MNRAS, 532, L14, doi: [10.1093/mnras/slae036](https://doi.org/10.1093/mnras/slae036)
- Benson, A. J. 2012, New Astronomy, 17, 175, doi: [10.1016/j.newast.2011.07.004](https://doi.org/10.1016/j.newast.2011.07.004)
- Benson, A. J. 2017, MNRAS, 467, 3454, doi: [10.1093/mnras/stx343](https://doi.org/10.1093/mnras/stx343)
- Benson, A. J., Kamionkowski, M., & Hassani, S. H. 2005, MNRAS, 357, 847, doi: [10.1111/j.1365-2966.2005.08679.x](https://doi.org/10.1111/j.1365-2966.2005.08679.x)
- Bernard, E. J., Monelli, M., Gallart, C., et al. 2013, MNRAS, 432, 3047, doi: [10.1093/mnras/stt655](https://doi.org/10.1093/mnras/stt655)
- Bernstein-Cooper, E. Z., Cannon, J. M., Elson, E. C., et al. 2014, AJ, 148, 35, doi: [10.1088/0004-6256/148/2/35](https://doi.org/10.1088/0004-6256/148/2/35)
- Besançon, M., Papamarkou, T., Anthoff, D., et al. 2021, Journal of Statistical Software, 98, doi: [10.18637/jss.v098.i16](https://doi.org/10.18637/jss.v098.i16)
- Bezanson, J., Edelman, A., Karpinski, S., & Shah, V. B. 2017, SIAM Review, 59, 65, doi: [10.1137/141000671](https://doi.org/10.1137/141000671)

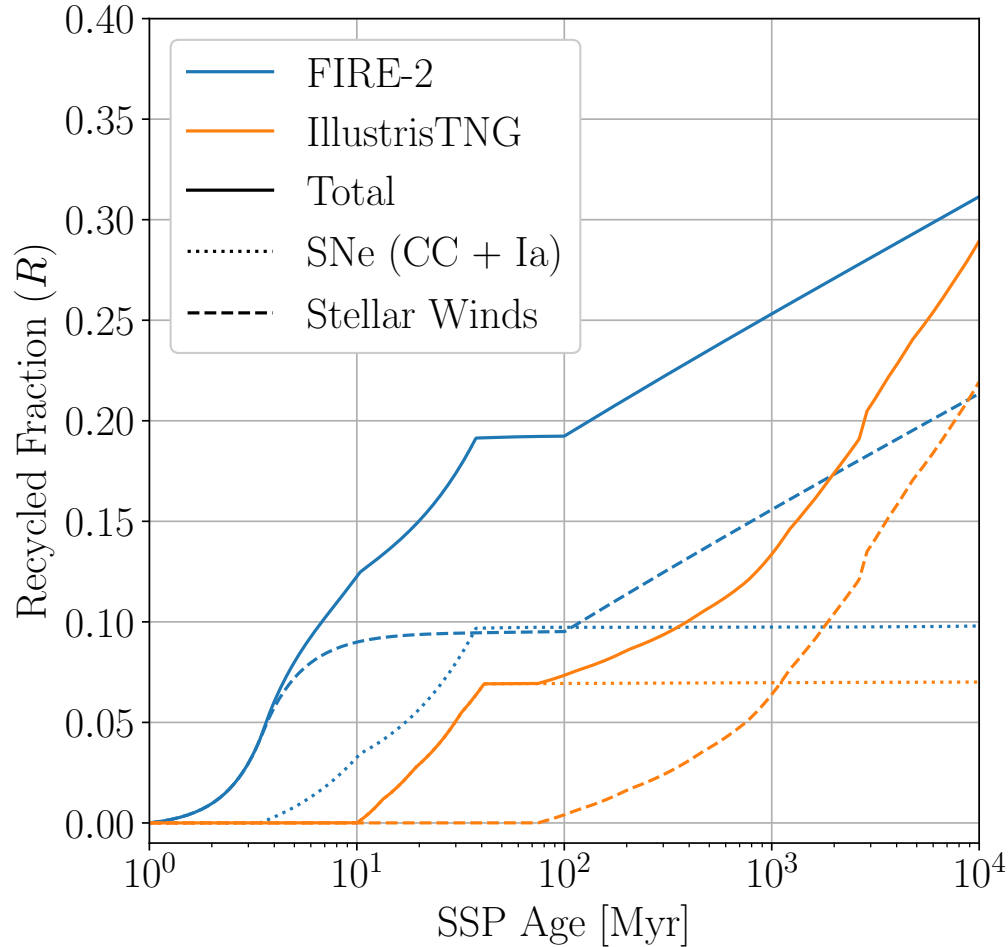


Figure 14. The recycled fraction (i.e., the fraction of stellar mass returned to the ISM) as a function of SSP age under the FIRE-2 (blue) and IllustrisTNG (orange) models. Shown are the total fractional mass loss (solid lines), as well as the fractional mass loss separated by source (dotted lines show fractional mass loss due to supernovae, dashed lines show fractional mass loss due to stellar winds).

Björklund, R., Sundqvist, J. O., Puls, J., & Najarro, F. 2021, *A&A*, 648, A36, doi: [10.1051/0004-6361/202038384](https://doi.org/10.1051/0004-6361/202038384)

Blanc, G. A., Lu, Y., Benson, A., Katsianis, A., & Barraza, M. 2019, *ApJ*, 877, 6, doi: [10.3847/1538-4357/ab16ec](https://doi.org/10.3847/1538-4357/ab16ec)

Blitz, L., & Rosolowsky, E. 2006, *ApJ*, 650, 933, doi: [10.1086/505417](https://doi.org/10.1086/505417)

Bond, J. R., Cole, S., Efstathiou, G., & Kaiser, N. 1991, *ApJ*, 379, 440, doi: [10.1086/170520](https://doi.org/10.1086/170520)

Bressan, A., Marigo, P., Girardi, L., et al. 2012, *MNRAS*, 427, 127, doi: [10.1111/j.1365-2966.2012.21948.x](https://doi.org/10.1111/j.1365-2966.2012.21948.x)

Buck, T., Dutton, A. A., & Macciò, A. V. 2019, *MNRAS*, 486, 1481, doi: [10.1093/mnras/stz969](https://doi.org/10.1093/mnras/stz969)

Cappellari, M. 2023, *MNRAS*, 526, 3273, doi: [10.1093/mnras/stad2597](https://doi.org/10.1093/mnras/stad2597)

Cardelli, J. A., Clayton, G. C., & Mathis, J. S. 1989, *ApJ*, 345, 245, doi: [10.1086/167900](https://doi.org/10.1086/167900)

Castelli, F., & Kurucz, R. L. 2003, in *IAU Symposium*, Vol. 210, *Modelling of Stellar Atmospheres*, ed. N. Piskunov, W. W. Weiss, & D. F. Gray, A20, doi: [10.48550/arXiv.astro-ph/0405087](https://doi.org/10.48550/arXiv.astro-ph/0405087)

Chabrier, G. 2003, *PASP*, 115, 763, doi: [10.1086/376392](https://doi.org/10.1086/376392)

Chen, Y., Bressan, A., Girardi, L., et al. 2015, *MNRAS*, 452, 1068, doi: [10.1093/mnras/stv1281](https://doi.org/10.1093/mnras/stv1281)

Chen, Y., Girardi, L., Bressan, a., et al. 2014, *MNRAS*, 444, 2525, doi: [10.1093/mnras/stu1605](https://doi.org/10.1093/mnras/stu1605)

Chen, Y., Girardi, L., Fu, X., et al. 2019, *A&A*, 632, A105, doi: [10.1051/0004-6361/201936612](https://doi.org/10.1051/0004-6361/201936612)

Chisholm, J., Tremonti, C., & Leitherer, C. 2018, *MNRAS*, 481, 1690, doi: [10.1093/mnras/sty2380](https://doi.org/10.1093/mnras/sty2380)

Choi, J., Dotter, A., Conroy, C., et al. 2016, *ApJ*, 823, 102, doi: [10.3847/0004-637x/823/2/102](https://doi.org/10.3847/0004-637x/823/2/102)

Christensen, C. R., Davé, R., Governato, F., et al. 2016, *ApJ*, 824, 57, doi: [10.3847/0004-637X/824/1/57](https://doi.org/10.3847/0004-637X/824/1/57)

- Christensen, C. R., Davé, R., Brooks, A., Quinn, T., & Shen, S. 2018, *ApJ*, 867, 142, doi: [10.3847/1538-4357/aae374](https://doi.org/10.3847/1538-4357/aae374)
- Cohen, R. E., McQuinn, K. B. W., Savino, A., et al. 2025, *ApJ*, 981, 153, doi: [10.3847/1538-4357/adb61d](https://doi.org/10.3847/1538-4357/adb61d)
- Cole, A. A., Weisz, D. R., Dolphin, A. E., et al. 2014, *ApJ*, 795, 54, doi: [10.1088/0004-637X/795/1/54](https://doi.org/10.1088/0004-637X/795/1/54)
- Cole, A. A., Skillman, E. D., Tolstoy, E., et al. 2007, *ApJL*, 659, L17, doi: [10.1086/516711](https://doi.org/10.1086/516711)
- Cole, N., Newberg, H. J., Magdon-Ismail, M., et al. 2008, *ApJ*, 683, 750, doi: [10.1086/589681](https://doi.org/10.1086/589681)
- Cole, S., Lacey, C. G., Baugh, C. M., & Frenk, C. S. 2000, *MNRAS*, 319, 168, doi: [10.1046/j.1365-8711.2000.03879.x](https://doi.org/10.1046/j.1365-8711.2000.03879.x)
- Conroy, C. 2013, *ARA&A*, 51, 393, doi: [10.1146/annurev-astro-082812-141017](https://doi.org/10.1146/annurev-astro-082812-141017)
- Conroy, C., Villaume, A., van Dokkum, P. G., & Lind, K. 2018, *ApJ*, 854, 139, doi: [10.3847/1538-4357/aaab49](https://doi.org/10.3847/1538-4357/aaab49)
- Curti, M., Mannucci, F., Cresci, G., & Maiolino, R. 2020, *MNRAS*, 491, 944, doi: [10.1093/mnras/stz2910](https://doi.org/10.1093/mnras/stz2910)
- Curti, M., Maiolino, R., Curtis-Lake, E., et al. 2024, *A&A*, 684, A75, doi: [10.1051/0004-6361/202346698](https://doi.org/10.1051/0004-6361/202346698)
- Davé, R., Anglés-Alcázar, D., Narayanan, D., et al. 2019, *MNRAS*, 486, 2827, doi: [10.1093/mnras/stz937](https://doi.org/10.1093/mnras/stz937)
- Davé, R., Finlator, K., & Oppenheimer, B. D. 2012, *MNRAS*, 421, 98, doi: [10.1111/j.1365-2966.2011.20148.x](https://doi.org/10.1111/j.1365-2966.2011.20148.x)
- Davies, L. J. M., Robotham, A. S. G., del P Lagos, C., et al. 2019, *MNRAS*, 483, 5444–5458, doi: [10.1093/mnras/sty3393](https://doi.org/10.1093/mnras/sty3393)
- Dolphin, A. 1997, *New Astronomy*, 2, 397, doi: [10.1016/S1384-1076\(97\)00029-8](https://doi.org/10.1016/S1384-1076(97)00029-8)
- Dolphin, A. E. 2002, *MNRAS*, 332, 91, doi: [10.1046/j.1365-8711.2002.05271.x](https://doi.org/10.1046/j.1365-8711.2002.05271.x)
- Dolphin, A. E. 2012, *ApJ*, 751, 60, doi: [10.1088/0004-637x/751/1/60](https://doi.org/10.1088/0004-637x/751/1/60)
- Dolphin, A. E. 2016, *ApJ*, 825, 153, doi: [10.3847/0004-637X/825/2/153](https://doi.org/10.3847/0004-637X/825/2/153)
- Dolphin, A. E., Saha, A., Skillman, E. D., et al. 2003, *AJ*, 126, 187, doi: [10.1086/375761](https://doi.org/10.1086/375761)
- Dotter, A. 2016, *ApJS*, 222, 8, doi: [10.3847/0067-0049/222/1/8](https://doi.org/10.3847/0067-0049/222/1/8)
- Durbin, M. J., Choi, Y., Savino, A., et al. 2025, *ArXiv e-prints*, arXiv:2505.18252, doi: [10.48550/arXiv.2505.18252](https://doi.org/10.48550/arXiv.2505.18252)
- Emerick, A., Bryan, G. L., & Mac Low, M.-M. 2018, *ApJL*, 865, L22, doi: [10.3847/2041-8213/aae315](https://doi.org/10.3847/2041-8213/aae315)
- Escala, I., Wetzel, A., Kirby, E. N., et al. 2018, *MNRAS*, 474, 2194, doi: [10.1093/mnras/stx2858](https://doi.org/10.1093/mnras/stx2858)
- Evans, C. J., Castro, N., Gonzalez, O. A., et al. 2019, *A&A*, 622, A129, doi: [10.1051/0004-6361/201834145](https://doi.org/10.1051/0004-6361/201834145)
- Feldmann, R. 2015, *MNRAS*, 449, 3274, doi: [10.1093/mnras/stv552](https://doi.org/10.1093/mnras/stv552)
- Feldmann, R., Quataert, E., Faucher-Giguère, C.-A., et al. 2023, *MNRAS*, 522, 3831, doi: [10.1093/mnras/stad1205](https://doi.org/10.1093/mnras/stad1205)
- Gallart, C., Zoccali, M., & Aparicio, A. 2005, *ARA&A*, 43, 387, doi: [10.1146/annurev.astro.43.072103.150608](https://doi.org/10.1146/annurev.astro.43.072103.150608)
- Garcia, A. M., Torrey, P., Grasha, K., et al. 2024a, *MNRAS*, 529, 3342, doi: [10.1093/mnras/stae737](https://doi.org/10.1093/mnras/stae737)
- Garcia, A. M., Torrey, P., Ellison, S., et al. 2024b, *MNRAS*, 531, 1398, doi: [10.1093/mnras/stae1252](https://doi.org/10.1093/mnras/stae1252)
- Garcia, A. M., Torrey, P., Bhagwat, A., et al. 2025a, *ApJ*, 989, 147, doi: [10.3847/1538-4357/adea51](https://doi.org/10.3847/1538-4357/adea51)
- Garcia, A. M., Torrey, P., Ellison, S. L., et al. 2025b, *MNRAS*, 536, 119, doi: [10.1093/mnras/stae2587](https://doi.org/10.1093/mnras/stae2587)
- Garling, C. 2025, *Zenodo*, doi: [10.5281/zenodo.14963317](https://doi.org/10.5281/zenodo.14963317)
- Garling, C. T., Kallivayalil, N., McQuinn, K. B. W., et al. 2025, *ApJS*, 277, 25, doi: [10.3847/1538-4365/adbb64](https://doi.org/10.3847/1538-4365/adbb64)
- Gill, S. P. D., Knebe, A., & Gibson, B. K. 2004, *MNRAS*, 351, 399, doi: [10.1111/j.1365-2966.2004.07786.x](https://doi.org/10.1111/j.1365-2966.2004.07786.x)
- Giovanelli, R., Haynes, M. P., Adams, E. A. K., et al. 2013, *AJ*, 146, 15, doi: [10.1088/0004-6256/146/1/15](https://doi.org/10.1088/0004-6256/146/1/15)
- Gordon, K. D., Fouesneau, M., Arab, H., et al. 2016, *ApJ*, 826, 104, doi: [10.3847/0004-637X/826/2/104](https://doi.org/10.3847/0004-637X/826/2/104)
- Gunasekera, C. M., van Hoof, P. A. M., Chatzikos, M., & Ferland, G. J. 2023, *RNAAS*, 7, 246, doi: [10.3847/2515-5172/ad0e75](https://doi.org/10.3847/2515-5172/ad0e75)
- Hafen, Z., Faucher-Giguère, C.-A., Anglés-Alcázar, D., et al. 2019, *MNRAS*, 488, 1248, doi: [10.1093/mnras/stz1773](https://doi.org/10.1093/mnras/stz1773)
- Harvey, T., Conselice, C. J., Adams, N. J., et al. 2025, *MNRAS*, 542, 2998, doi: [10.1093/mnras/staf1396](https://doi.org/10.1093/mnras/staf1396)
- Hawcroft, C., Mahy, L., Sana, H., et al. 2024, *A&A*, 690, A126, doi: [10.1051/0004-6361/202348478](https://doi.org/10.1051/0004-6361/202348478)
- Hermosa Muñoz, L., Taibi, S., Battaglia, G., et al. 2020, *A&A*, 634, A10, doi: [10.1051/0004-6361/201936136](https://doi.org/10.1051/0004-6361/201936136)
- Hidalgo, S. L., Pietrinferni, A., Cassisi, S., et al. 2018, *ApJ*, 856, 125, doi: [10.3847/1538-4357/aab158](https://doi.org/10.3847/1538-4357/aab158)
- Hopkins, P. F., Kereš, D., Oñorbe, J., et al. 2014, *MNRAS*, 445, 581, doi: [10.1093/mnras/stu1738](https://doi.org/10.1093/mnras/stu1738)
- Hopkins, P. F., Wetzel, A., Kereš, D., et al. 2018, *MNRAS*, 480, 800, doi: [10.1093/mnras/sty1690](https://doi.org/10.1093/mnras/sty1690)
- Hopkins, P. F., Wetzel, A., Wheeler, C., et al. 2023, *MNRAS*, 519, 3154, doi: [10.1093/mnras/stac3489](https://doi.org/10.1093/mnras/stac3489)
- Hunter, D. A., Ficut-Vicas, D., Ashley, T., et al. 2012, *AJ*, 144, 134, doi: [10.1088/0004-6256/144/5/134](https://doi.org/10.1088/0004-6256/144/5/134)
- Hunter, J. D. 2007, *Computing In Science & Engineering*, 9, 90, doi: [10.1109/MCSE.2007.55](https://doi.org/10.1109/MCSE.2007.55)
- Ianjamasimanana, R., Namumba, B., Ramaila, A. J. T., et al. 2020, *MNRAS*, 497, 4795, doi: [10.1093/mnras/staa1967](https://doi.org/10.1093/mnras/staa1967)

- Jain, S., Sanders, R. L., Khostovan, A. A., et al. 2025, ArXiv e-prints, doi: [10.48550/ARXIV.2508.18369](https://doi.org/10.48550/ARXIV.2508.18369)
- Jiang, F., & van den Bosch, F. C. 2014, MNRAS, 440, 193, doi: [10.1093/mnras/stu280](https://doi.org/10.1093/mnras/stu280)
- Johnson, B. D., Leja, J., Conroy, C., & Speagle, J. S. 2021, ApJS, 254, 22, doi: [10.3847/1538-4365/abef67](https://doi.org/10.3847/1538-4365/abef67)
- Kado-Fong, E., Geha, M., Mao, Y.-Y., et al. 2024, ApJ, 966, 129, doi: [10.3847/1538-4357/ad3042](https://doi.org/10.3847/1538-4357/ad3042)
- Karakas, A. I. 2010, MNRAS, 403, 1413, doi: [10.1111/j.1365-2966.2009.16198.x](https://doi.org/10.1111/j.1365-2966.2009.16198.x)
- Kawinwanichakij, L., Papovich, C., Quadri, R. F., et al. 2017, ApJ, 847, 134, doi: [10.3847/1538-4357/aa8b75](https://doi.org/10.3847/1538-4357/aa8b75)
- Kepley, A. A., Wilcots, E. M., Hunter, D. A., & Nordgren, T. 2007, AJ, 133, 2242, doi: [10.1086/513716](https://doi.org/10.1086/513716)
- Kirby, E. N., Cohen, J. G., Guhathakurta, P., et al. 2013, ApJ, 779, 102, doi: [10.1088/0004-637X/779/2/102](https://doi.org/10.1088/0004-637X/779/2/102)
- Kirby, E. N., Lanfranchi, G. a., Simon, J. D., Cohen, J. G., & Guhathakurta, P. 2011a, ApJ, 727, 78, doi: [10.1088/0004-637X/750/2/173](https://doi.org/10.1088/0004-637X/750/2/173)
- Kirby, E. N., Martin, C. L., & Finlator, K. 2011b, ApJL, 742, L25, doi: [10.1088/2041-8205/742/2/L25](https://doi.org/10.1088/2041-8205/742/2/L25)
- Kirby, E. N., Rizzi, L., Held, E. V., et al. 2017, ApJ, 834, 9, doi: [10.3847/1538-4357/834/1/9](https://doi.org/10.3847/1538-4357/834/1/9)
- Kirby, E. N., Xie, J. L., Guo, R., et al. 2019, ApJ, 881, 45, doi: [10.3847/1538-4357/ab2c02](https://doi.org/10.3847/1538-4357/ab2c02)
- Knebe, A., Stoppacher, D., Prada, F., et al. 2018, MNRAS, 474, 5206, doi: [10.1093/mnras/stx2662](https://doi.org/10.1093/mnras/stx2662)
- Knollmann, S. R., & Knebe, A. 2009, ApJS, 182, 608, doi: [10.1088/0067-0049/182/2/608](https://doi.org/10.1088/0067-0049/182/2/608)
- Kobayashi, C., Umeda, H., Nomoto, K., Tominaga, N., & Ohkubo, T. 2006, ApJ, 653, 1145, doi: [10.1086/508914](https://doi.org/10.1086/508914)
- Koester, D. 2010, Mem. Soc. Astron. Italiana, 81, 921. <https://ui.adsabs.harvard.edu/abs/2010MmSAI..81..921K>
- Kroupa, P. 2001, MNRAS, 322, 231, doi: [10.1046/j.1365-8711.2001.04022.x](https://doi.org/10.1046/j.1365-8711.2001.04022.x)
- Kurucz, R. L. 2005, Memorie della Societa Astronomica Italiana Supplementi, 8, 14. <https://ui.adsabs.harvard.edu/abs/2005MSAIS...8...14K>
- Kurucz, R. L. 2014, in Determination of Atmospheric Parameters of B, A, F, and G-Type Stars, ed. E. Niemczura, B. Smalley, & W. Pych (Springer International Publishing), 39–51, doi: [10.1007/978-3-319-06956-2_4](https://doi.org/10.1007/978-3-319-06956-2_4)
- Kvasova, K. A., & Kirby, E. N. 2025, ApJ, 982, 92, doi: [10.3847/1538-4357/adb729](https://doi.org/10.3847/1538-4357/adb729)
- Leaman, R., Cole, A. A., Venn, K. A., et al. 2009, ApJ, 699, 1, doi: [10.1088/0004-637X/699/1/1](https://doi.org/10.1088/0004-637X/699/1/1)
- Lee, H., Skillman, E. D., Cannon, J. M., et al. 2006, ApJ, 647, 970, doi: [10.1086/505573](https://doi.org/10.1086/505573)
- Leitherer, C., Schaerer, D., Goldader, J. D., et al. 1999, ApJS, 123, 3, doi: [10.1086/313233](https://doi.org/10.1086/313233)
- Li, F., Rahman, M., Murray, N., et al. 2021, MNRAS, 500, 1038, doi: [10.1093/mnras/staa3322](https://doi.org/10.1093/mnras/staa3322)
- Li, M., Cai, Z., Bian, F., et al. 2023, ApJL, 955, L18, doi: [10.3847/2041-8213/acf470](https://doi.org/10.3847/2041-8213/acf470)
- Lilly, S. J., Carollo, C. M., Pipino, A., Renzini, A., & Peng, Y. 2013, ApJ, 772, 119, doi: [10.1088/0004-637X/772/2/119](https://doi.org/10.1088/0004-637X/772/2/119)
- Lin, D., Widmann, D., Byrne, S., et al. 2025, Zenodo, doi: [10.5281/ZENODO.2647458](https://doi.org/10.5281/ZENODO.2647458)
- Ma, X., Hopkins, P. F., Faucher-Giguère, C.-A., et al. 2016, MNRAS, 456, 2140, doi: [10.1093/mnras/stv2659](https://doi.org/10.1093/mnras/stv2659)
- Maoz, D., Mannucci, F., & Brandt, T. D. 2012, MNRAS, 426, 3282, doi: [10.1111/j.1365-2966.2012.21871.x](https://doi.org/10.1111/j.1365-2966.2012.21871.x)
- Marigo, P., Girardi, L., Bressan, A., et al. 2017, ApJ, 835, 77, doi: [10.3847/1538-4357/835/1/77](https://doi.org/10.3847/1538-4357/835/1/77)
- Marszewski, A., Faucher-Giguère, C.-A., Feldmann, R., & Sun, G. 2025, ApJL, 991, L4, doi: [10.3847/2041-8213/adf74b](https://doi.org/10.3847/2041-8213/adf74b)
- Marszewski, A., Sun, G., Faucher-Giguère, C.-A., Hayward, C. C., & Feldmann, R. 2024, ApJL, 967, L41, doi: [10.3847/2041-8213/ad4cee](https://doi.org/10.3847/2041-8213/ad4cee)
- McConnachie, A. W. 2012, AJ, 144, 4, doi: [10.1088/0004-6256/144/1/4](https://doi.org/10.1088/0004-6256/144/1/4)
- McQuinn, K. B. W., Skillman, E. D., Dolphin, A., et al. 2015, ApJ, 812, 158, doi: [10.1088/0004-637x/812/2/158](https://doi.org/10.1088/0004-637x/812/2/158)
- McQuinn, K. B. W., Newman, M. J. B., Skillman, E. D., et al. 2024a, ApJ, 976, 60, doi: [10.3847/1538-4357/ad8158](https://doi.org/10.3847/1538-4357/ad8158)
- McQuinn, K. B. W., Newman, M. J., Savino, A., et al. 2024b, ApJ, 961, 16, doi: [10.3847/1538-4357/ad1105](https://doi.org/10.3847/1538-4357/ad1105)
- Mitchell, P. D., Schaye, J., Bower, R. G., & Crain, R. A. 2020, MNRAS, 494, 3971, doi: [10.1093/mnras/staa938](https://doi.org/10.1093/mnras/staa938)
- Mogensen, P. K., & Riseth, A. N. 2018, Journal of Open Source Software, 3, 615, doi: [10.21105/joss.00615](https://doi.org/10.21105/joss.00615)
- Moutard, T., Sawicki, M., Arnouts, S., et al. 2018, MNRAS, 479, 2147, doi: [10.1093/mnras/sty1543](https://doi.org/10.1093/mnras/sty1543)
- Muratov, A. L., Kereš, D., Faucher-Giguère, C.-A., et al. 2015, MNRAS, 454, 2691, doi: [10.1093/mnras/stv2126](https://doi.org/10.1093/mnras/stv2126)
- Muratov, A. L., Kereš, D., Faucher-Giguère, C.-A., et al. 2017, MNRAS, 468, 4170, doi: [10.1093/mnras/stx667](https://doi.org/10.1093/mnras/stx667)
- Nadler, E. O., Benson, A., Driskell, T., Du, X., & Gluscevic, V. 2023, MNRAS, 521, 3201, doi: [10.1093/mnras/stad666](https://doi.org/10.1093/mnras/stad666)
- Nakajima, K., Ouchi, M., Isobe, Y., et al. 2023, ApJS, 269, 33, doi: [10.3847/1538-4365/acd556](https://doi.org/10.3847/1538-4365/acd556)
- Narayanan, D., Lower, S., Torrey, P., et al. 2024, ApJ, 961, 73, doi: [10.3847/1538-4357/ad0966](https://doi.org/10.3847/1538-4357/ad0966)
- Nelson, D., Pillepich, A., Springel, V., et al. 2019, MNRAS, 490, 3234, doi: [10.1093/mnras/stz2306](https://doi.org/10.1093/mnras/stz2306)

- Nelson, D., Sharma, P., Pillepich, A., et al. 2020, *MNRAS*, 498, 2391, doi: [10.1093/mnras/staa2419](https://doi.org/10.1093/mnras/staa2419)
- Nocedal, J. 2006, Numerical optimization, second edition edn., ed. S. J. Wright, Springer series in operations research and financial engineering (New York, NY: Springer)
- Nomoto, K., Tominaga, N., Umeda, H., Kobayashi, C., & Maeda, K. 2006, *NuPhA*, 777, 424, doi: [10.1016/j.nuclphysa.2006.05.008](https://doi.org/10.1016/j.nuclphysa.2006.05.008)
- O'Donnell, J. E. 1994, *ApJ*, 422, 158, doi: [10.1086/173713](https://doi.org/10.1086/173713)
- Pandya, V., Somerville, R. S., Anglés-Alcázar, D., et al. 2020, *ApJ*, 905, 4, doi: [10.3847/1538-4357/abc3c1](https://doi.org/10.3847/1538-4357/abc3c1)
- Pandya, V., Fielding, D. B., Anglés-Alcázar, D., et al. 2021, *MNRAS*, 508, 2979, doi: [10.1093/mnras/stab2714](https://doi.org/10.1093/mnras/stab2714)
- Papovich, C., Kawinwanichakij, L., Quadri, R. F., et al. 2018, *ApJ*, 854, 30, doi: [10.3847/1538-4357/aaa766](https://doi.org/10.3847/1538-4357/aaa766)
- Papp, T. K., Widmann, D., Aluthge, D., et al. 2023, Zenodo, doi: [10.5281/zenodo.3384417](https://doi.org/10.5281/zenodo.3384417)
- Parkinson, H., Cole, S., & Helly, J. 2008, *MNRAS*, 383, 557, doi: [10.1111/j.1365-2966.2007.12517.x](https://doi.org/10.1111/j.1365-2966.2007.12517.x)
- Paxton, B., Cantiello, M., Arras, P., et al. 2013, *ApJS*, 208, 4, doi: [10.1088/0067-0049/208/1/4](https://doi.org/10.1088/0067-0049/208/1/4)
- Paxton, B., Marchant, P., Schwab, J., et al. 2015, *ApJS*, 220, 15, doi: [10.1088/0067-0049/220/1/15](https://doi.org/10.1088/0067-0049/220/1/15)
- Peimbert, M., Colin, P., & Sarmiento, A. 1994, in *Violent Star Formation, from 30 Doradus to QSOs* (Cambridge University Press), 79. <https://ui.adsabs.harvard.edu/abs/1994vsf.book...79P>
- Pietrinferni, A., Cassisi, S., Salaris, M., & Castelli, F. 2004, *ApJ*, 612, 168, doi: [10.1086/422498](https://doi.org/10.1086/422498)
- Pietrinferni, A., Cassisi, S., Salaris, M., & Castelli, F. 2006, *ApJ*, 642, 797, doi: [10.1086/501344](https://doi.org/10.1086/501344)
- Pietrinferni, A., Cassisi, S., Salaris, M., & Hidalgo, S. 2013, *A&A*, 558, A46, doi: [10.1051/0004-6361/201321950](https://doi.org/10.1051/0004-6361/201321950)
- Pietrinferni, A., Salaris, M., Cassisi, S., et al. 2024, *MNRAS*, 527, 2065, doi: [10.1093/mnras/stad3267](https://doi.org/10.1093/mnras/stad3267)
- Pietrinferni, A., Hidalgo, S., Cassisi, S., et al. 2021, *ApJ*, 908, 102, doi: [10.3847/1538-4357/abd4d5](https://doi.org/10.3847/1538-4357/abd4d5)
- Pillepich, A., Springel, V., Nelson, D., et al. 2018, *MNRAS*, 473, 4077, doi: [10.1093/mnras/stx2656](https://doi.org/10.1093/mnras/stx2656)
- Pillepich, A., Nelson, D., Springel, V., et al. 2019, *MNRAS*, 490, 3196, doi: [10.1093/mnras/stz2338](https://doi.org/10.1093/mnras/stz2338)
- Plez, B. 2011, in *Journal of Physics Conference Series*, Vol. 328, *Journal of Physics Conference Series* (IOP), 012005, doi: [10.1088/1742-6596/328/1/012005](https://doi.org/10.1088/1742-6596/328/1/012005)
- Portinari, L., Chiosi, C., & Bressan, A. 1998, *A&A*, 334, 505
- Press, W. H., & Schechter, P. 1974, *ApJ*, 187, 425, doi: [10.1086/152650](https://doi.org/10.1086/152650)
- Putman, M. E., Zheng, Y., Price-Whelan, A. M., et al. 2021, *ApJ*, 913, 53, doi: [10.3847/1538-4357/abe391](https://doi.org/10.3847/1538-4357/abe391)
- Ramesh, R., Nelson, D., & Pillepich, A. 2023a, *MNRAS*, 518, 5754, doi: [10.1093/mnras/stac3524](https://doi.org/10.1093/mnras/stac3524)
- Ramesh, R., Nelson, D., & Pillepich, A. 2023b, *MNRAS*, 522, 1535, doi: [10.1093/mnras/stad951](https://doi.org/10.1093/mnras/stad951)
- Reimers, D. 1975, *Memoires of the Societe Royale des Sciences de Liege*, 8, 369. <https://ui.adsabs.harvard.edu/abs/1975MSRSL...8..369R>
- Rey, M. P., Taylor, E., Gray, E. I., et al. 2025, *ArXiv e-prints*, doi: [10.48550/arXiv.2503.03813](https://doi.org/10.48550/arXiv.2503.03813)
- Roca-Fàbrega, S., Kim, J.-h., Primack, J. R., et al. 2024, *ApJ*, 968, 125, doi: [10.3847/1538-4357/ad43de](https://doi.org/10.3847/1538-4357/ad43de)
- Rosenfield, P., Marigo, P., Girardi, L., et al. 2016, *ApJ*, 822, 73, doi: [10.3847/0004-637X/822/2/73](https://doi.org/10.3847/0004-637X/822/2/73)
- Ruiz-Escobedo, F., Peña, M., Hernández-Martínez, L., & García-Rojas, J. 2018, *MNRAS*, 481, 396, doi: [10.1093/mnras/sty2265](https://doi.org/10.1093/mnras/sty2265)
- Salaris, M., Cassisi, S., Pietrinferni, A., & Hidalgo, S. 2022, *MNRAS*, 509, 5197, doi: [10.1093/mnras/stab3359](https://doi.org/10.1093/mnras/stab3359)
- Savino, A., Weisz, D. R., Skillman, E. D., et al. 2023, *ApJ*, 956, 86, doi: [10.3847/1538-4357/acf46f](https://doi.org/10.3847/1538-4357/acf46f)
- Savino, A., Weisz, D. R., Dolphin, A. E., et al. 2025, *ApJ*, 979, 205, doi: [10.3847/1538-4357/ada24f](https://doi.org/10.3847/1538-4357/ada24f)
- Schlaflly, E. F., & Finkbeiner, D. P. 2011, *ApJ*, 737, 103, doi: [10.1088/0004-637X/737/2/103](https://doi.org/10.1088/0004-637X/737/2/103)
- Schlegel, D. J., Finkbeiner, D. P., & Davis, M. 1998, *ApJ*, 500, 525, doi: [10.1086/305772](https://doi.org/10.1086/305772)
- Segers, M. C., Crain, R. A., Schaye, J., et al. 2016, *MNRAS*, 456, 1235, doi: [10.1093/mnras/stv2562](https://doi.org/10.1093/mnras/stv2562)
- Skillman, E. D., Salzer, J. J., Berg, D. A., et al. 2013, *AJ*, 146, 3, doi: [10.1088/0004-6256/146/1/3](https://doi.org/10.1088/0004-6256/146/1/3)
- Skillman, E. D., Monelli, M., Weisz, D. R., et al. 2017, *ApJ*, 837, 102, doi: [10.3847/1538-4357/aa60c5](https://doi.org/10.3847/1538-4357/aa60c5)
- Springel, V., & Hernquist, L. 2003, *MNRAS*, 339, 289, doi: [10.1046/j.1365-8711.2003.06206.x](https://doi.org/10.1046/j.1365-8711.2003.06206.x)
- Springel, V., White, S. D. M., Tormen, G., & Kauffmann, G. 2001, *MNRAS*, 328, 726, doi: [10.1046/j.1365-8711.2001.04912.x](https://doi.org/10.1046/j.1365-8711.2001.04912.x)
- Steinwandel, U. P., Rennehan, D., Orr, M. E., Fielding, D. B., & Kim, C.-G. 2025, *ApJ*, 991, 16, doi: [10.3847/1538-4357/adf283](https://doi.org/10.3847/1538-4357/adf283)
- Tammann, G. A., Reindl, B., & Sandage, A. 2011, *A&A*, 531, A134, doi: [10.1051/0004-6361/201016382](https://doi.org/10.1051/0004-6361/201016382)
- Tang, J., Bressan, A., Rosenfield, P., et al. 2014, *MNRAS*, 445, 4287, doi: [10.1093/mnras/stu2029](https://doi.org/10.1093/mnras/stu2029)
- Telford, O. G., Chisholm, J., Sander, A. A. C., et al. 2024, *ApJ*, 974, 85, doi: [10.3847/1538-4357/ad697e](https://doi.org/10.3847/1538-4357/ad697e)

- Tollet, É., Cattaneo, A., Macciò, A. V., Dutton, A. A., & Kang, X. 2019, *MNRAS*, 485, 2511, doi: [10.1093/mnras/stz545](https://doi.org/10.1093/mnras/stz545)
- Torres-Ríos, G., Pérez, I., Verley, S., et al. 2024, *A&A*, 691, A341, doi: [10.1051/0004-6361/202450675](https://doi.org/10.1051/0004-6361/202450675)
- Torrey, P., Vogelsberger, M., Marinacci, F., et al. 2019, *MNRAS*, 484, 5587, doi: [10.1093/mnras/stz243](https://doi.org/10.1093/mnras/stz243)
- Tremblay, P. E., & Bergeron, P. 2009, *ApJ*, 696, 1755, doi: [10.1088/0004-637X/696/2/1755](https://doi.org/10.1088/0004-637X/696/2/1755)
- Tung, P.-C., & Chen, K.-J. 2025, *ApJ*, 988, 127, doi: [10.3847/1538-4357/ade1d4](https://doi.org/10.3847/1538-4357/ade1d4)
- Urbaneja, M. A., Bresolin, F., & Kudritzki, R.-P. 2023, *ApJ*, 959, 52, doi: [10.3847/1538-4357/acfc3d](https://doi.org/10.3847/1538-4357/acfc3d)
- Van Nest, J., Munshi, F., Christensen, C., et al. 2023, *ApJ*, 956, 96, doi: [10.3847/1538-4357/acf861](https://doi.org/10.3847/1538-4357/acf861)
- van Zee, L., Skillman, E. D., & Haynes, M. P. 2006, *ApJ*, 637, 269, doi: [10.1086/498298](https://doi.org/10.1086/498298)
- Vincenzo, F., Matteucci, F., Belfiore, F., & Maiolino, R. 2016, *MNRAS*, 455, 4183, doi: [10.1093/mnras/stv2598](https://doi.org/10.1093/mnras/stv2598)
- Vink, J. S., de Koter, A., & Lamers, H. J. G. L. M. 2001, *A&A*, 369, 574, doi: [10.1051/0004-6361:20010127](https://doi.org/10.1051/0004-6361:20010127)
- Walcher, J., Groves, B., Budavári, T., & Dale, D. 2011, *Astrophysics and Space Science*, 331, 1, doi: [10.1007/s10509-010-0458-z](https://doi.org/10.1007/s10509-010-0458-z)
- Wang, B., Leja, J., Atek, H., et al. 2025, *ApJ*, 987, 184, doi: [10.3847/1538-4357/adddb8](https://doi.org/10.3847/1538-4357/adddb8)
- Wang, Y., Nadler, E. O., Mao, Y.-Y., et al. 2024, *ApJ*, 976, 119, doi: [10.3847/1538-4357/ad7f4c](https://doi.org/10.3847/1538-4357/ad7f4c)
- Weerasooriya, S., Bovill, M. S., Benson, A., Musick, A. M., & Ricotti, M. 2023, *ApJ*, 948, 87, doi: [10.3847/1538-4357/acc32b](https://doi.org/10.3847/1538-4357/acc32b)
- Weerasooriya, S., Bovill, M. S., Taylor, M. A., Benson, A. J., & Leahy, C. 2024, *ApJ*, 968, 78, doi: [10.3847/1538-4357/ad3924](https://doi.org/10.3847/1538-4357/ad3924)
- Weinberger, R., Springel, V., Hernquist, L., et al. 2017, *MNRAS*, 465, 3291, doi: [10.1093/mnras/stw2944](https://doi.org/10.1093/mnras/stw2944)
- Weisz, D. R., Skillman, E. D., Hidalgo, S. L., et al. 2014, *ApJ*, 789, 24, doi: [10.1088/0004-637x/789/1/24](https://doi.org/10.1088/0004-637x/789/1/24)
- Weisz, D. R., Dolphin, A. E., Savino, A., et al. 2024, *ApJS*, 271, 47, doi: [10.3847/1538-4365/ad2600](https://doi.org/10.3847/1538-4365/ad2600)
- Wetzel, A., Hayward, C. C., Sanderson, R. E., et al. 2023, *ApJS*, 265, 44, doi: [10.3847/1538-4365/acb99a](https://doi.org/10.3847/1538-4365/acb99a)
- White, S. D. M., & Frenk, C. S. 1991, *ApJ*, 379, 52, doi: [10.1086/170483](https://doi.org/10.1086/170483)
- Woo, J., Dekel, A., Faber, S. M., et al. 2013, *MNRAS*, 428, 3306, doi: [10.1093/mnras/sts274](https://doi.org/10.1093/mnras/sts274)
- Wright, R. J., Somerville, R. S., Lagos, C. d. P., et al. 2024, *MNRAS*, 532, 3417, doi: [10.1093/mnras/stae1688](https://doi.org/10.1093/mnras/stae1688)
- Zentner, A. R. 2007, *International Journal of Modern Physics D*, 16, 763, doi: [10.1142/S0218271807010511](https://doi.org/10.1142/S0218271807010511)
- Zhang, J., Fakhouri, O., & Ma, C.-P. 2008, *MNRAS*, 389, 1521, doi: [10.1111/j.1365-2966.2008.13671.x](https://doi.org/10.1111/j.1365-2966.2008.13671.x)
- Zhu, C., Byrd, R. H., Lu, P., & Nocedal, J. 1997, *ACM Transactions on Mathematical Software*, 23, 550, doi: [10.1145/279232.279236](https://doi.org/10.1145/279232.279236)
- Zu, Y., & Mandelbaum, R. 2016, *MNRAS*, 457, 4360, doi: [10.1093/mnras/stw221](https://doi.org/10.1093/mnras/stw221)